2012

A Study on the Welding Characteristics of Tailor Welded Blank Metal Sheets Using GTAW and Laser Welding

PORNSAK THASANARAPHAN
Lehigh University

A Study on the Welding Characteristics of Tailor Welded Blank Metal Sheets Using GTAW and Laser Welding

by

Pornsak Thasanaraphan

Presented to the Graduate and Research Committee
of Lehigh University
in Candidacy for the Degree of
Doctor of Philosophy

in

Mechanical Engineering

Lehigh University

September 2012

Approved and recommended for acceptance as a dissertation in partial fulfillment of the requirements for the degree of Doctor of Philosophy.

_____
Date

_____
Professor Herman F. Nied
Mechanical Engineering and Mechanics
Dissertation Advisor

_____
Accepted Date

Committee Members:

_____
Professor Terry J. Delph
Mechanical Engineering and Mechanics

_____
Professor John P. Coulter
Mechanical Engineering and Mechanics

_____
Professor John N. DuPont
Materials Science and Engineering

ACKNOWLEDGEMENT

First, I would like to gratefully thank my advisor, Prof. Herman F. Nied from Lehigh University, whose tremendous help, suggestion, and encouragement helped me in all the time of research and writing of this dissertation. I would like to thank Prof. John N. DuPont and his advisee from the Material Engineering Department for valuable suggestion and for the help on using LENS machine. Also, I would like to thank my PhD Committee for their guidance and recommendation throughout my study. I would like to show my deep gratitude also to all the staff and labmates in the Mechanical Engineering and Mechanics department, who helped me a lot in my research.

Next, I would like to acknowledge Khun Amnard Tungkanawanich and Khun Teerawut Prasongkij from the United Coil Center Limited for providing the samples and information for this study. Those samples are very important to my research. I also thank ESI Group for providing the SYSWELD software.

In addition, I am greatly indebted to Thai Government for financing to my study and to the Thailand Institute of Scientific and Technological Research to allow me to study at Lehigh University. I would like to thank an Emergency Student Fund (ESF) grant from Institute of International Education (IIE).

I owe my deepest gratitude to my family and girlfriend who supported me note only financially, but also mentally.

Finally, I would like to express my deepest gratitude to all of those who gave me the possibility to complete this research. This time was a great period in my life and allowed me to meet a lot of new friendly people and to make good on my research.

LIST OF TABLES

LIST OF FIGURES

Contents

ABSTRACT

In this study, a computational and experimental effort was carried out to qualitatively understand the weld pool shape, distortion and residual stress for continuous laser welding and manual pulsed gas metal arc welding. For all the welding simulations given in this dissertation, a welding specific finite element package, SYSWELD, is used. This research focuses on the welding behavior observed in light-weight metal structures known as the tailor-welded blanks, TWBs. They are a combination of two or more metal sheets with different thickness and/or different materials that are welded together in a single plane prior to forming, e.g., stamping. They made from the low carbon steel. As laser welding experiment results show, the weld pool shape at the top and bottom surface, is strongly influenced by surface tension, giving it a characteristic hourglass shape. In order to simulate the hourglass shape, a new volumetric heat source model was developed to predict the transient temperature profile and weld pool shape, including the effect of surface tension. Tailor welded blanks with different thicknesses were examined in the laser welding process. All major physical phenomena such as thermal conduction, heat radiation and convection heat losses are taken into account in the model development as well as temperature-dependant thermal and mechanical material properties. The model is validated for the case of butt joint welding of cold rolled steel sheets. The results of the numerical simulations provide temperature distributions representing the shape of the molten pool, distortion and residual stress with varying laser beam power and welding speed. It is demonstrated that the finite element simulation results are in good agreement with the

experiment results. This includes the weld pool shape and sheet metal distortion. While there is no experimental data to compare directly with residual stress results, the distorted shape provides an indirect measure of the welding residual stresses.

The welding details such as clamping, butt joint configuration, material, sample thickness are similar for both the laser welding process and the manual pulsed GTAW process. Also as same metallurgical investigation, the weld pool shape displays wider full penetration without the effect of surface tension. The double ellipsoid volumetric heat source is applied in the finite element simulation to determine the temperature distribution, distortion and residual stress. The simulation results are compared with the experimental results and show good agreement. In addition, the results from the laser welding process are compared to the equivalent results from the GTAW process in the order to better understand the fundamental differences between these two welding processes.

CHAPTER 1

Introduction

During the past two decades fuel conservation and safety mandates along with environmental concerns have prompted the automotive industry to design lighter cars for reduced fuel consumption while improving the overall structure of their vehicles for occupant safety. Therefore, the concept of combining various steel options using welding processes into a welded blank was developed to enable product and manufacturing engineers to "tailor" the blank so that steel's best properties were located precisely within the part they were needed.

1.1 Tailor-Welded blank

Use of the tailor-welded blank (TWB) continues to grow in the automotive industry. TWB consists of two or more metal sheets that have been welded together in a single plane prior to subsequent forming. With variable-thickness blanks, produced by welding together different sheet-stock combinations in specific regions, it is possible to make finished parts with a desirable variation in properties such as strength and corrosion resistance. It's common for TWBs to be composed of different sheets of different thickness, with different strength and material properties. This allows the use of thicker or stronger materials in the critical regions of a component, so as to increase the local stiffness, while thinner or lighter materials are used in other regions to reduce overall component weight.

Fig. 1.1 presents a few characteristic examples of TWBs fabricated using different methods. Examples A-D shows TWBs of different shapes, different thicknesses and different materials. Example E shows a typical weld between two metal sheets with different thicknesses. Example F-H shows a welding of different materials. This study focuses on the D and E case.

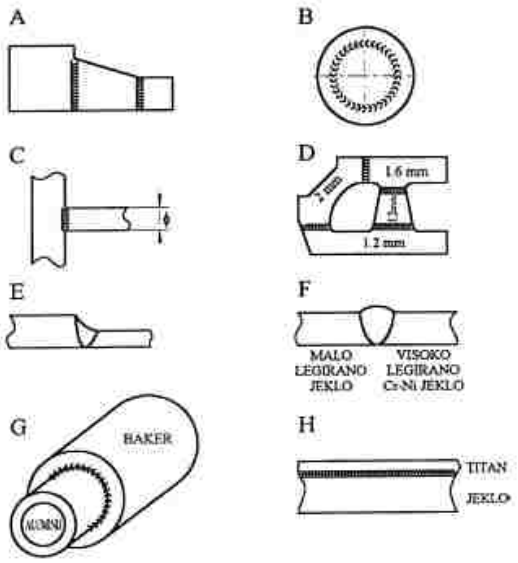

Figure 1.1 A few characteristic examples of tailored blanks and profiles.

[J. Tusek et al. / J of Mat Pro Tech 119 (2001)]

In the automotive industry, steel tailor-welded blanks are used to provide optimum strength using the least amount of material possible for specific points on a vehicle. The major application is with steel TWB sheet for automotive components such as body side frames, door inner panels, motor compartment rails, center pillar inner panels, and wheelhouse/shock tower panels. Fig. 1.2 displays two steel TWBs which are

closely examined in this study: 1. rear door inner reinforcement beam (no.9) and 2. front door inner reinforcement beam (no.12). TWB is used in the floor assembly (Fig. 1.3).

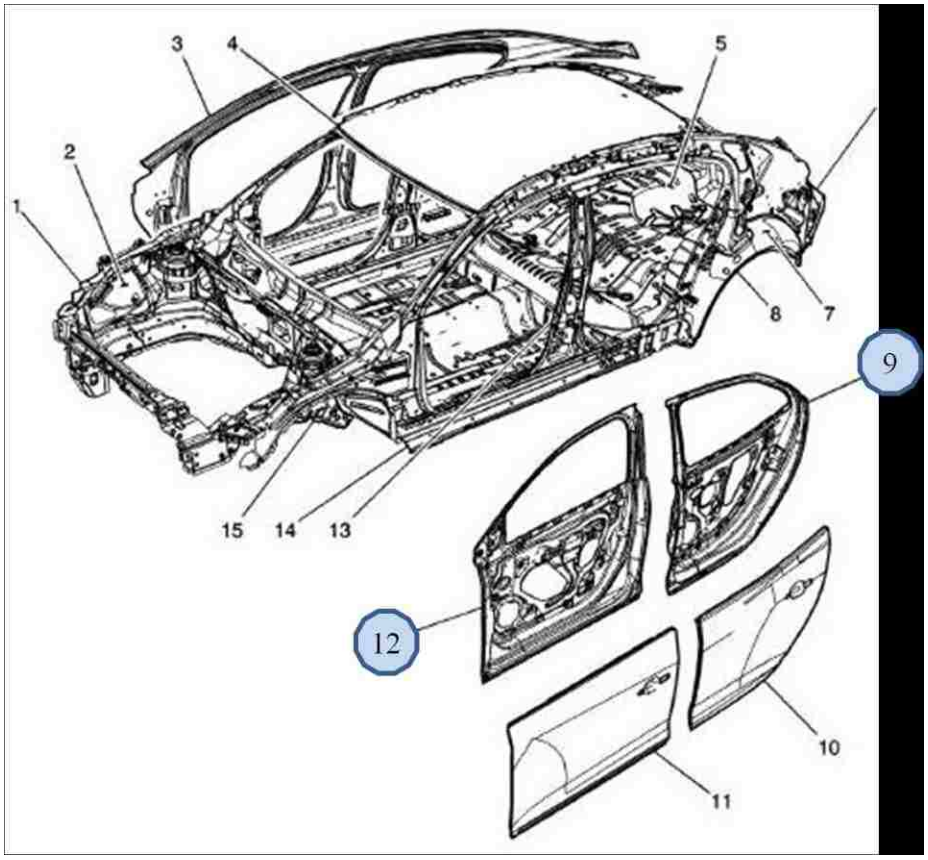

Figure 1.2 View of automotive TWB application

[United Coil Center Limited, UCC]

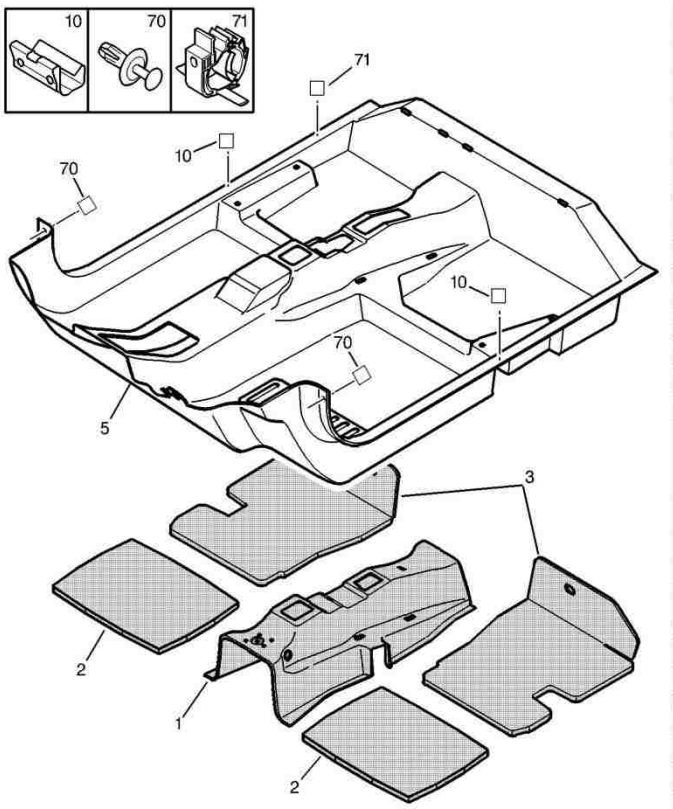

Figure 1.3 Floor panels.

[United Coil Center Limited, UCC]

1.2 Welding Simulation

As mention, there are many processes to assembly TWB. In the automotive industry, the laser welding process is the dominant TWB welding technology. The laser welding process is used for combining two or more metal sheets that have been welded together in a single plane prior to forming. Most of the tailor-welded blanks are welded using a laser beam heat source, especially Nd:YAG and CO_2 lasers [1]. The laser welding process, compared with the conventional welding processes (GMA, TIG etc.),

is an efficient joining technology for lightweight structures, because of its low localized energy input resulting in low distortion, deep penetration, high strength of the joint, and high processing speeds. Recently, a wide range of research activity has been undertaken in the area of laser beam delivery systems. Huntington and Eagar studied laser light absorption on aluminum and aluminum alloys [2]. Laser welding of aluminum alloys has been applied in various industrial applications [3, 4, 5, 6]. MIG welding and laser welding were used for joining austenitic stainless steel with ferrite non-stainless steel [1]. However, Tusek et al states that the tailed blanks of high-alloy stainless steel cannot be welded to low-alloy ferrite steel, without the addition of a filler material. The mechanical performance of the weld in TWB is tested [7].

During the welding process, the flow of molten metal is unstable and complex, which has a significant effect on the shape of weld pool controlled by the plasma drag force, electromagnetic force (Lorentz force), buoyancy force, and surface tension [8]. The influence of the heat flow and the fluid flow in the transient development of the weld pool during gas tungsten arc and laser beam welding with the independent temperature coefficient of surface tension was studied in [9]. The heat transfer and fluid flow in the weld pool are controlled by surface tension gradient, causing the molten metal to be drawn along the surface from the region of lower surface tension to that of higher surface tension. For pure metal and alloys, the temperature coefficient of surface tension, $\left(\frac{d\gamma}{dT}\right)$, is negative. In cases where the surface tension temperature coefficient is negative, the flow field is radially outward at the weld pool surface. As a result, both

top and bottom weld pool surfaces are widely deformed, giving it a characteristic hourglass shape [35].

The finite element simulation of the temperature profiles and weld pool shapes vary according to the models of the laser beam. Sometime the existing models, or heat source equations, are not available to predict the weld pool shape from those effects, especially surface tension. There are various volumetric heat sources. Probably the most used three dimensional heat source definition is Goldak's heat source [10]. Since all parameters are defined on the surface, it is difficult to use Goldak's double elliptic heat source for deep penetration. Another form of the volumetric heat source is the conical heat source model which is specially designed for laser and electron beam welding. Sometimes a heat source composed of two different models is also used. However, determining the shape of the weld pool, in cases where the effect of surface tension is difficult to simulate, is generally not feasible based on first principles alone. Attentively, empirical models have been developed. A power distribution function was created by superimposing a spherical and a conical heat source in order to simulate this behavior [11 - 12]. The prediction of the hourglass shape observed in Fig.1.5 for the weld pool is still limited. An objective of this study was to develop a new volumetric heat source model to predict the dimension of hourglass-like weld pool shapes for the laser welding of the sheet metal blanks.

During the laser welding process, the local temperature developed from the laser beam consists of a rapid heating and subsequent cooling phase, which generates

residual stresses and distortions in a structure. Masubuchi discussed the various types of welding-induced distortions and residual stresses [13]. The distortion causes problems in the assembly process as well as the product quality. The residual stress field is an important welding artifact as it may directly affect the mechanical behavior of the structure in several ways. In some cases, this may cause unexpected failure in the structure. The finite element method (FEM) can be used to simulate the laser welding process and predict the final distortions and residual stresses in steel plate butt joints [14 - 15]. Distortion and residual stress investigations of laser welding for aluminum alloys has been reported previously [16]. An uncoupled thermo-mechanical analysis was performed to predict the distortions and residual stresses for a single-pass fusion welded thin test plate [17]. However, there is very limited published literature describing the prediction and measurement of distortion and residual stress in very thin sheets in particular. In this study, for lightweight structures, whose thickness is less than 1.2 mm. distortion predictions are of particular interest.

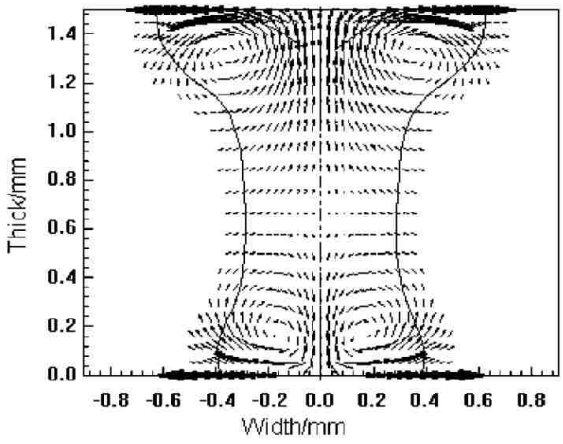

Figure 1.4 The velocity distribution in weld pool due to the surface tension [35].

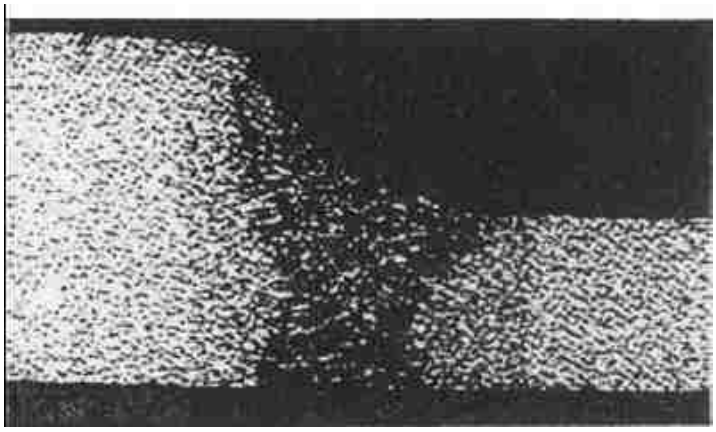

Figure 1.5 The hourglass shape of the weld pool for different thickness. [1]

CHAPTER 2

Fundamental

This chapter briefly describes the fundamentals of the welding processes, type of joints, fluid flow in weld pool, and materials using in the study.

2.1 Laser Welding

The word LASER stands for 'Light Amplification by Stimulated Emission of Radiation'. By the amplification of light in a resonator, a beam of coherent light with a high energy density was generated. This laser beam can be used in a lot of different ways like cutting, heat treatment, measuring, and welding.

In laser welding, a laser beam is focused on a workpiece where the absorption of the radiation leads to a local heating and fusion of the workpiece. In general, there are two different basic methods that should be distinguished: conduction welding and keyhole or penetration welding. The main difference between these modes is that the surface of the weld pool remains unbroken for the conduction welding process, i.e., the laser radiation does not penetrate into the material being welded. As a result, conduction welds are less susceptible to gas entrapment during the welding process. In keyhole welding, when the laser intensity is higher than approximately 10^6 W/cm^2 the weld pool opens and forms a narrow slot or keyhole so that the laser beam can enter the weld pool. The result is that the laser beam not only melts, but also evaporates, the material. The schematic sketches of these two welding modes are shown in Fig. 2.1.

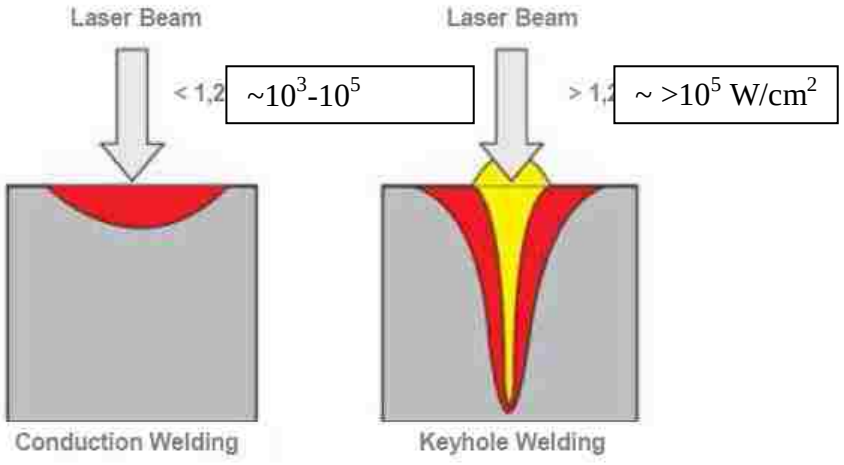

Figure 2.1 Comparison of conduction and keyhole welding [19]

As stated above, the keyhole formation basically depends on the heat source intensity, the wavelength, and, in the case of non-normal incidence on the polarization of the laser beam and the thermal properties of the workpiece.

2.2 Gas Tungsten Arc Welding

Gas tungsten arc welding (GTAW), commonly call TIG (tungsten inert gas), is an arc welding process whose heat source is an electric arc established between a non-consumable tungsten electrode and the metals, as shown in Fig. 2.2. The electrode and the weld are protected by a shielding gas, and filler metal may or may not be used.

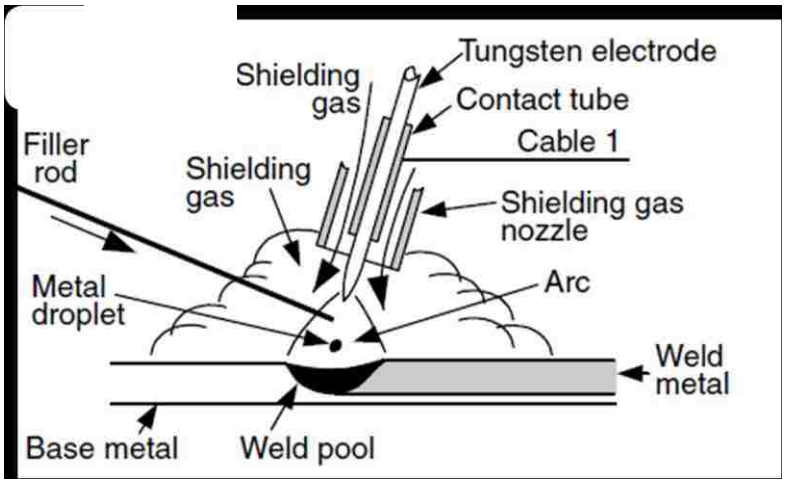

Figure 2.2 Gas tungsten arc welding. [20]

GTAW is suitable for joining butt joints of thin sheets by fusion alone because its limited heat inputs.

2.3 Types of joints

Fig. 2.3 shows the basic welding joint designs: the butt, lap, tee, corner and edge joints. The butt joint is designated for welding tailor blanks. Therefore, the butt joint is the primary considered in this study.

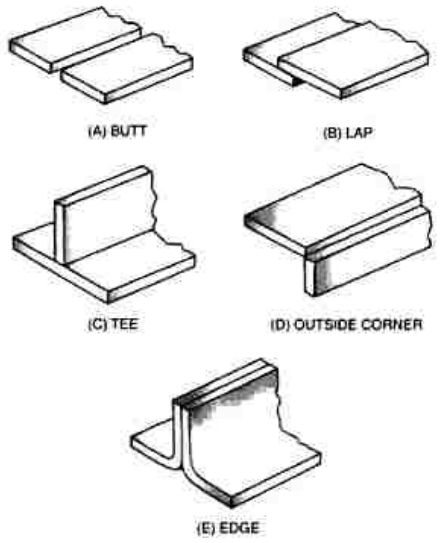

Figure 2.3 Five basic types of welding joint designs. [21]

2.4 Fluid flow in weld pool

The driving forces for fluid flow in the weld pool includes the buoyancy force, the electromagnetic force (Lorentz force), surface tension force (Marangoni convection), and the arc plasma shear stress as shown in Fig. 2.4. Note that the Lorentz force is absent in laser welding but otherwise the basic heat transfer and fluid flow mechanisms are similar for both welding processes.

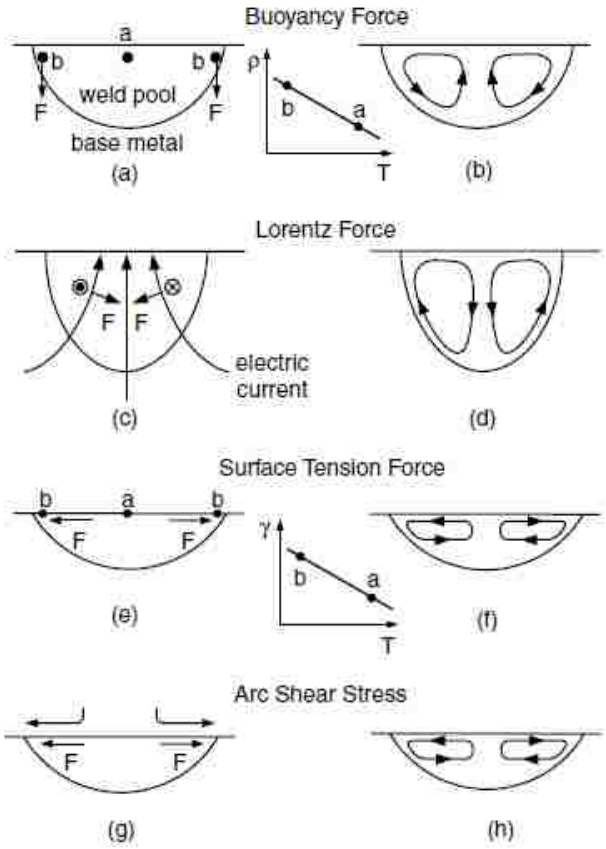

Figure 2.4 The driving forces for weld pool convection [20]

For the thin metal sheet, the real weld pool geometry for the laser welding is not a simple shape. For full penetration weld, the surface tension effect makes the weld pool wider at the top and bottom surfaces. During the welding process, the surface tension of the liquid metal decreases with increasing temperature. The hotter liquid metal with the lower surface tension is pulled outward by the cooler liquid metal with the higher surface tension. As a result, the liquid metal from the center flows to the edge and returns to below the pool surface, resulting in a wider weld pool. Shear stress induced by the surface tension gradient is also called thermocapillary convection or Marangoni

convection. Pitscheneder et al. [22] calculated Marangoni convection in stationary steel weld pools for a laser power of 5200 W. R. Rai et al. [23] developed and tested a computationally efficient heat-transfer and fluid-flow model considering recoil pressure, gravitational force, and surface tension of key hole mode laser welding that can be applied to both partial and full penetration welds taking into account convective heat transfer in the weld pool. The most important pressure terms at the keyhole wall are evaluated for the Nd:YAG laser welding process of thin aluminum (AA5182) and mild steel (DC04) sheets [24]. The result showed that the surface tension pressure term becomes dominant and causes keyhole elongation, eventually resulting in holes when the plate thickness is comparable to the keyhole diameter.

2.5 Materials

The materials used for this study were a cold roll steel sheet and a galvannealed steel sheet. The galvannealed steel is the result from the combined process of galvanizing and annealing. The grade of material for both steels defined by the Japan Iron and Steel Federation Standard and equivalent to the Japan Industrial Standard was shown in the table 2-1. Their chemical composition is reported in Table 2-2.

Table 2.1 Materials:

Cold Roll Steel Sheet, CR	Standard	Equivalent to
JSC270F	JFS	
SP121BQ		JIS NO. G3141
Galvannealed Steel Sheet, GA		
JAC270F	JFS	
SP783-590BQ		JIS NO. G3302
JAC270FNN	JFS	

Remark: JFS = The Japan Iron and Steel Federation Standard

JIS = Japanese Industrial Standards

Table 2.2 Chemical composition of cold roll steel and galvannealed steel, wt.%

Material	Chemical Composition					
	C	Si	Mn	P	S	Fe
JSC270F	0.001	0.01	0.1	0.02	0.006	Bal.
SP121BQ	0.001	0.01	0.23	0.02	0.008	Bal.
JAC270F	0.001	0.01	0.15	0.012	0.006	Bal.
JAC270FNN	0.002	0.01	0.13	0.01	0.006	Bal.
SP783-590BQ	0.085	0.44	1.97	0.015	0.002	Bal.

In SYSWELD material database, there are some available low carbon steel alloys. Those materials are equivalent to Material Database that is available in SYSWELD as following.

Cold Roll Steel (JSC270F and SP121BQ) = DC04 (EN10130, EURONORM)

Galvannealed Steel Sheet (SP785-590BQ) = TRIP700 (EN10338, EURONORM)

The carbon content for the cold rolled steel is very low, less than 0.1 weight percent carbon as well as the content of sulfur and of phosphorus. Consequently, the low carbon steel displays good weldability, meaning that they can be generally welded.

2.6 Heat Transfer Analysis

To determine the thermal fields during the welding process, the equation of energy conservation is required. The heat transfer of laser beam welding is usually calculated by applying classical heat conduction theory. The thermal analysis is conducted using temperature dependent thermal material properties [25]. The governing partial differential equation for the transient heat conduction is

$$\frac{\partial}{\partial x}\left(k_x \frac{\partial T}{\partial x}\right)+\frac{\partial}{\partial y}\left(k_y \frac{\partial T}{\partial y}\right)+\frac{\partial}{\partial z}\left(k_z \frac{\partial T}{\partial z}\right)+Q=\rho C_p\left(\frac{\partial T}{\partial t}-v\frac{\partial T}{\partial x}\right) \tag{2.1}$$

where ρ is the density (kg/m^3), C_p is the specific heat (J/K), ν is the welding speed, T is the temperature (^{o}K), t is the time (s), k is the thermal conductivity(W/mK) , and Q is the volumetric heat source term which varies with beam power and absorption efficiency (W/m^3). All of these quantities are strong functions of temperature and possibly other welding variables.

The significant factors affecting heat conduction and thermal analysis are the heat input rate, boundary and initial conditions. In order to solve the differential equation, the boundary conditions also need to be specified. A portion of the energy is lost by convection and radiation. The heat lost is usually described mathematically by

$$q_{conv}=h_{conv}(T-T_0) \tag{2.2}$$

$$q_{rad} = \sigma\varepsilon(T^4 - T_0^4) \tag{2.3}$$

where h_{conv} is the convection coefficient (W/m^2K), T and T_0 are the plate and ambient temperatures (K), respectively, σ is the Stefan-Boltzman constant, and ε is the heat emissivity.

In the case where the specimen contacts the metal support base plate, the heat loss from the bottom surface is particular the heat conduction lost from the work to the support.

$$q_{cond} = k(T - T_S)/l \tag{2.4}$$

where h_{cond} (k/l) is the conduction coefficient (W/m^2K), T_S and T are the temperature of the support and test plate temperatures (K), respectively and l is the length of weld line (mm).

2.7 Effects of Welding

Distortion and residual stress closely related phenomena are two major effects after welding.

2.7.1 Types of Distortion

In a thermal cycle, heating and cooling, thermal strains occur in the weld metal and base metal regions near the weld. The strains produced during welding are accompanied by plastic deformation. The stresses resulting from these strains produce internal forces that cause bending, bucking, and rotation. It is these displacements that are called distortion.

The basic types of distortion for a rectangular plate with a centric joining weld are presented in Fig. 2.5. These dimensional changes are classified by their appearance as follows:

a. Angular deformation. A non-uniform thermal distribution in the thickness direction causes angular change close to the weld line.

b. Transverse deformation. Shrinkage perpendicular to the weld line.

c. Longitudinal deformation. Shrinkage in the direction of the weld line.

d. Bending deformation. Distortion in a plane through the weld line and perpendicular to the plane.

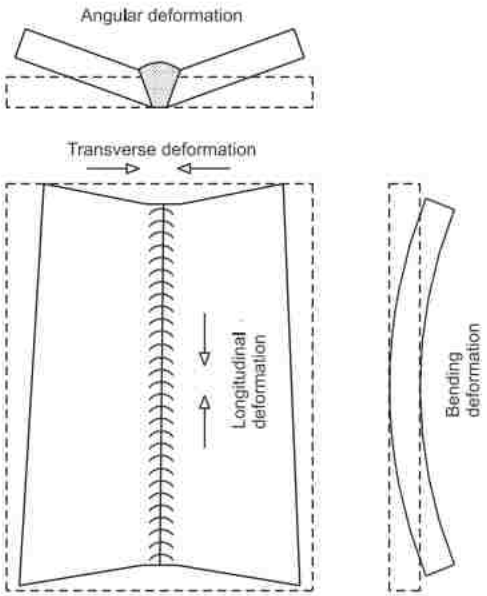

Figure 2.5 Basic types of distortion [13]

2.7.2 Residual stress

Residual stresses occur when a material is subjected to a non-uniform temperature change associated with the welding thermal stresses. During the welding process a local area is heated up rapidly with high thermal gradients. The thermal gradients cause the localized expansion, but the expansion is restrained by the surrounding colder and stronger material. When the finished weldment cools, some areas cool and contract more rapidly than others, leaving residual stresses. Fig. 2.6 shows a typical distribution of residual stress in a weld. For long continuous welds, the significant stresses are those parallel to the welding direction, designated σ_x, which are usually called the longitudinal stresses, and those transverse to σ_x, designated σ_y, which are called the transverse stresses. Tensile stresses are produced in the weldment and adjacent to weldment, and compressive stresses are produced in the areas a certain distance from the weld.

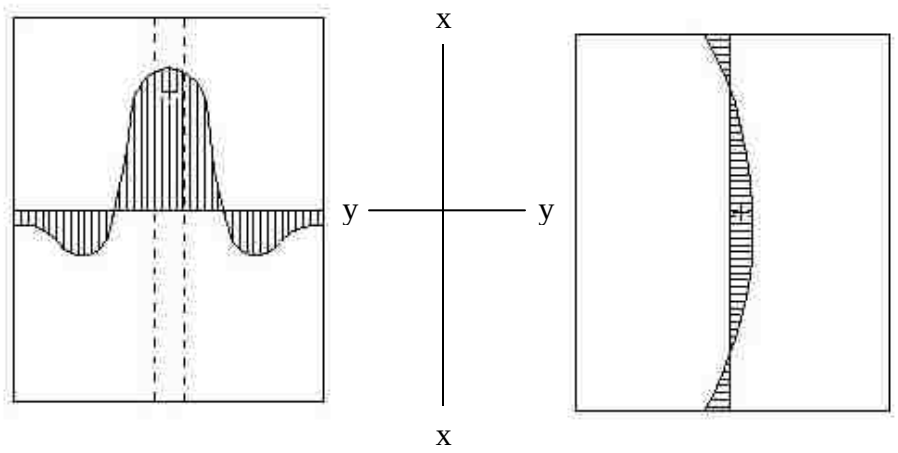

a. Longitudinal residual stress b. Transverse residual stress

Figure 2.6 Typical distributions of residual stresses in a weld. [20]

CHAPTER 3

Experiment

This chapter describes the experimental methods and measurement techniques used in this study.

3.1 Welding Processes

In this study, the metal sheets were welded with the same and different materials as well as the different welding parameters and the welding processes. The base metals are different in terms of coatings or grades e.g. cold roll steel (CR) and galvannealed steel (GA), thickness e.g. 0.64 mm. and 1.2 mm, and welding process e.g. laser welding (L) and TIG welding (T). The laser-welded metal sheets are classified into two different combinations according to the grade of material. One is SM (same material) joining two base metals with the same material and the other is DM (different material) joining two base metals with the different material.

3.1.1 Laser Welding Process

A butt joint was welded using a 3 kW Oyabe Seiki Model: TRUMPF HAAS HLD3006 (Fig.3.1) Nd:YAG CW laser welding system with a 3.23 mm focal length and 8 m/min welding speed. The focus was on the top surface of the butt welded specimens refer to Fig.3.1. The laser welding machine specifications are shown in Table. 3.1. All welded specimens were fabricated with two thin sheets in the different thickness (0.65mm/1.2mm.). Fig. 3.2 schematically shows the clamping situation in the

experiments. The thin sheets were clamped tightly with a magnetic clamping system so that no movement during the welding process was allowed. During the experiments, power and welding speed were recorded. A sample laser welding specimen is shown in Fig. 3.3. Table 3.2 summarizes the welding parameters for the laser welded specimens.

Figure 3.1 Oyabe SeiKi semi auto welding laser.

[http://www.ucc.co.th/index_w.html**]**

Table 3.1 Laser machine specification

Capacity	Range
Thickness	0.5 mm. - 2.8 mm.
Width	300 mm. - 1500 mm.
Length	150 mm. - 1800 mm.
Cycle time	28 Sec / 1 Panel
Welding speed (Max)	120 m. / min (x-axis welding direction)
Power	3000 W.

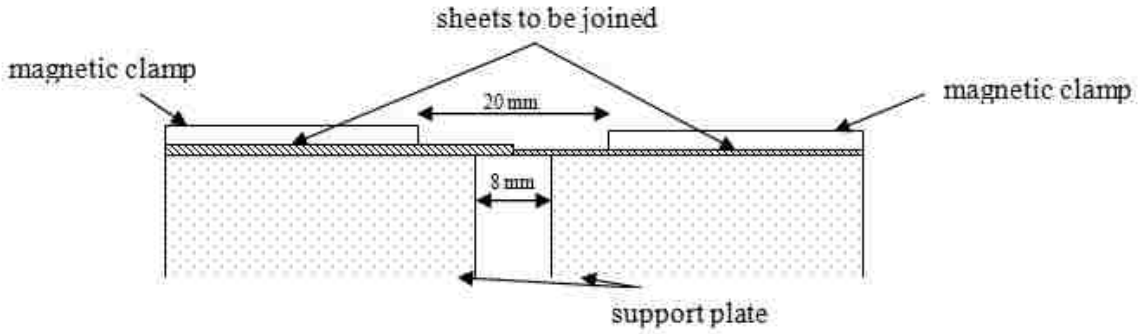

Figure 3.2 Schematic clamping situation for laser welding experiments.

Table 3.2 Welding parameters for laser welding process

Group	Specimen No.		Power (W)	Welding Speed (m/min)
A	ASML1	0.64t-CR/1.2t-CR (JSC270F/JSC270F)	2,858	8
	ADML1	0.64t-CR/1.2t-GA (JSC270F/JAC270F)	2,858	8
	ASML2	0.64t-GA/1.2t-GA (JAC270F/JAC270F)	2,858	8
B	BSML1	0.64t-CR/1.2t-CR (JSC270F/JSC270F)	3,000	8
	BDML1	0.64t-CR/1.2t-GA (SP121BQ/SP783-590BQ)	3,000	8
	BSML2	0.64t-GA/1.2t-GA (JAC270FNN/JAC270FNN)	3,000	8

After the laser welding processes, the samples from the United Coil Center Limited, Thailand, were shipped by Air mail to Lehigh University for study.

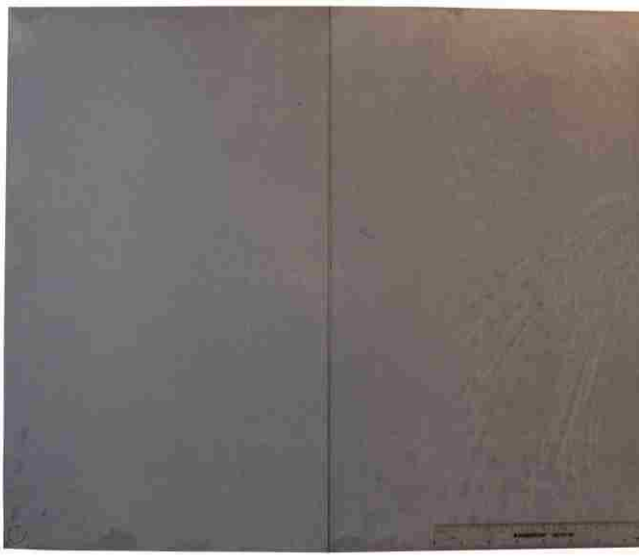

Figure 3.3 Sample of laser welding specimen for GA joining

3.1.2 Gas Tungsten Arc Welding Process

For the TIG welding, the specimens were manually welded by a Miller Syncrowave-250 ac/dc welding power supply (Fig. 3.4). An inert gas, 100% Argon was used as the shielding gas. The TIG welding machine specifications are shown in Fig. 3.5. The materials and thickness of samples were the same as those used in the laser welding experiment. The thin sheets were clamped with a C-clamp as shown in Fig. 3.6. The TIG welding was performed for comparison with the laser beam welding.

Figure 3.4 TIG welding machine

Rated Welding Output	PFC**	Amperes Input at AC Balanced Rated Load Output, 50/60 Hz, Single-Phase				KVA	KW	Amp Range	Max OCV	IP Rating
		200 V	230 V	460 V	575 V					
NEMA Class II (40) – 250 Amperes, 30 Volts AC, 40% Duty Cycle	No PFC	106 (4.6*)	92 (4*)	46 (2*)	37 (1.6*)	21 (0.89*)	11.4 (0.68*)	5–310 A	80 V	21 S
	With PFC	76	66	33	26	15.2	11.4			
*While idling **Power Factor Correction										

Rated Welding Output	PFC **	Amperes Input at AC Balanced Rated Load Output, 50/60 Hz, Single-Phase									KVA	KW	Amp Range	Max OCV	IP Rating
		200 V	220 V	230 V	260 V	380 V	415 V	460 V	520 V	575 V					
NEMA Class I (60) – 200 Amperes, 28 Volts AC, 60% Duty Cycle	No PFC	85 (4.6*)	77 (4.2*)	74 (4*)	65 (3.5*)	45 (2.4*)	41 (2.2*)	37 (2*)	33 (1.8*)	30 (1.6*)	17 (0.9*)	8.3 (0.7*)	5–310 A	80 V	21 S
	With PFC	55 (57*)	64 (51*)	48 (49*)	48 (49*)	37 (30*)	34 (27*)	24 (25*)	48 (49*)	19 (20*)	11 (11*)	8.3 (0.6*)			
*While idling **Power Factor Correction															

Figure 3.5 TIG welding machine specification

Figure 3.6 Schematic clamping situations for TIG welding experiments.

Table 3.3 Welding parameters for TIG welding process

Group	Specimen No.		Volt (V)	Current (A)	Welding Speed (mm/s)
A	ASMT1	0.64t-CR/1.2t-CR (JSC270F/JSC270F)	10	15	1.07
	ASMT2	0.64t-GA/1.2t-GA (JAC270F/JAC270F)	10	15	0.86
B	BSMT1	0.64t-CR/1.2t-CR (JSC270F/JSC270F)	8	20	1.13
	BSMT2	0.64t-GA/1.2t-GA (JAC270F/JAC270F)	8	25	0.95
	BSMT3	0.64t-GA/1.2t-GA (JAC270F/JAC270F)	8	25	1.28

3.2 Distortion Measurement

Following the welding experiments, a height gauge was used to determine the height h as shown in Fig. 3.7. Due to the relatively small angle (θ), the deflection at the center of the welding line (z) is approximately as h/2.

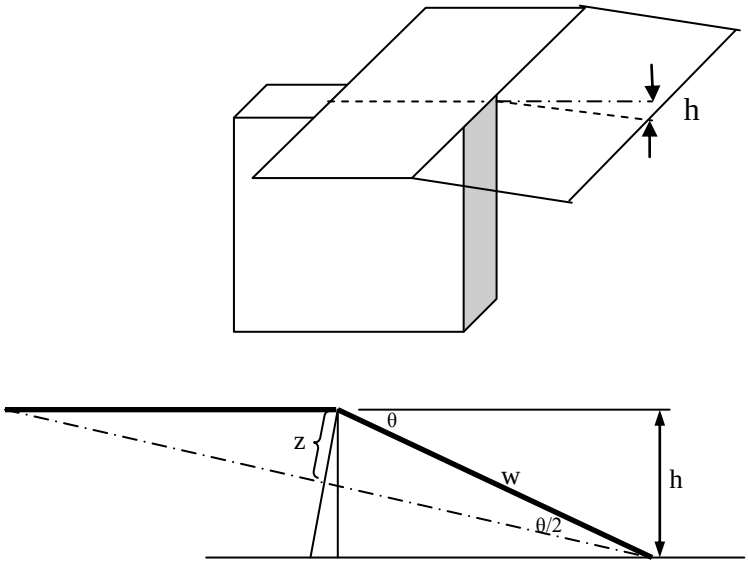

Figure 3.7 Schematic image of measuring the deflection in the weld joint.

3.3 Tensile Testing

Tensile tests were performed to determine the strength of the welds. Transverse samples (weld line perpendicular to the direction of application of load) were cut from representative welds (start, center, and end of the welding line) using a water-jet cutter to obtain tensile specimens. These same samples were also used for metallurgical analysis and hardness tests (Fig. 3.8). The normal tensile test specimen has 60 mm

length of reduced section and 20 mm width specified by AWS B4.0 for uniaxial tensile tests. The dimension of a tensile specimen is shown in Fig. 3.9 - 3.10.

The base metal (thinner sheet) and weld metal tests were performed on a tensile testing machine with a crosshead speed of 5 mm/s in accordance with the requirements of ASTM E8. The results of both tests were compared. The direction of the applied load was perpendicular to the weld line and will be referred to as a transverse specimen. Transverse tests were used to ensure that the weld does not crack before the failure occurs in the thinner material due to deformation. In the transverse tests, the thickness of the thinner side was taken as the initial thickness for calculation of the cross-section area as the fracture was expected on the thinner side. Each specimen was pulled to failure in the MTI Phoenix tensile machine. Fig. 3.11 displays a specimen in the tensile machine during testing.

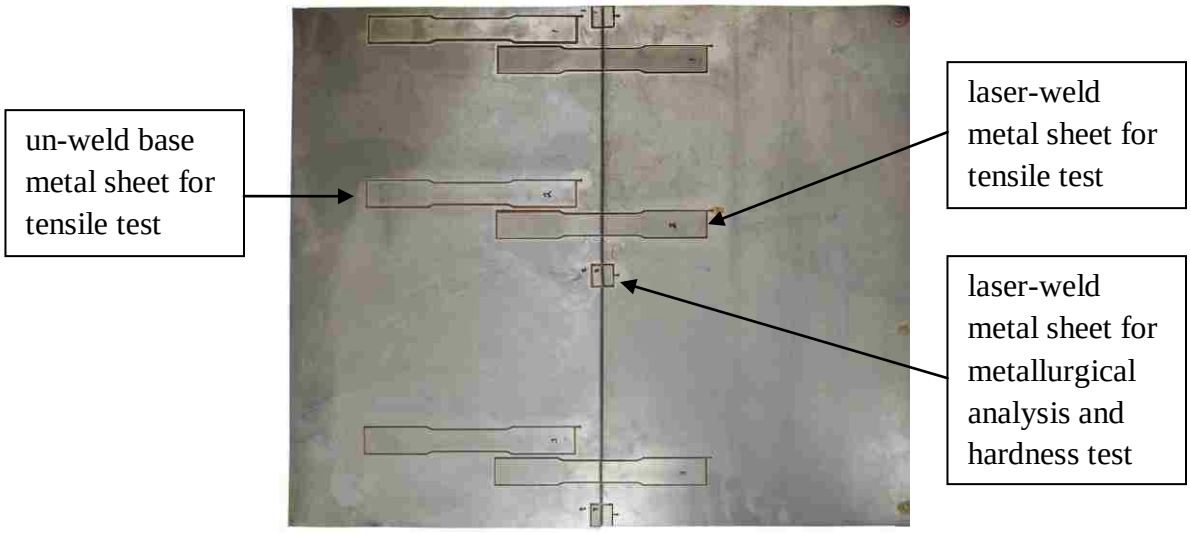

Figure 3.8 The locations were selected to investigation for tensile test metallurgical analysis and hardness test

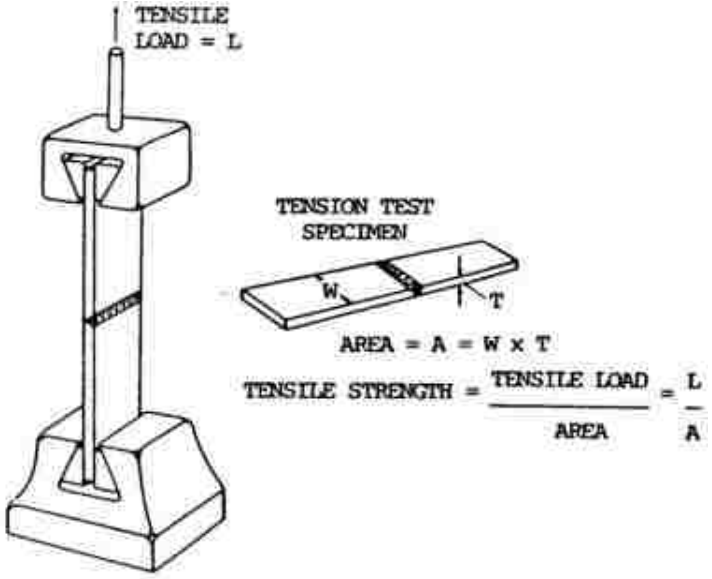

Figure 3.9 Tensile strength test specimen and test method [37]

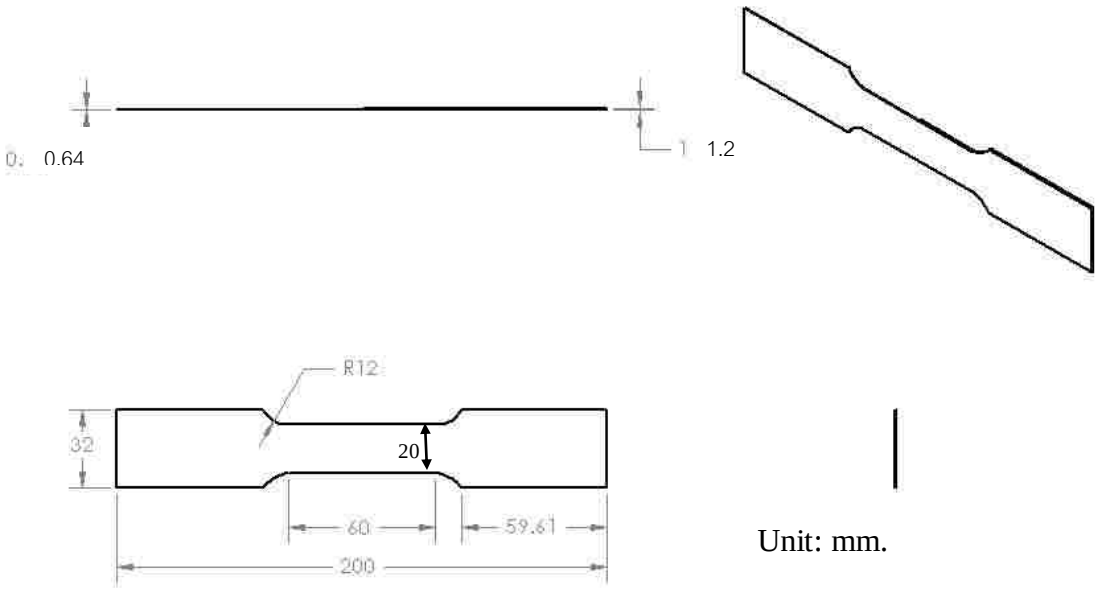

Figure 3.10 Dimension of tensile specimen

Figure 3.11 Tensile testing machine

3.4 Metallurgical Characterization

After welding, the specimens were cut on their cross-sectional area to reveal microstructure observations. The cut sample was mounted with resin and then polished using 320, 400, and 600 sand papers, followed by a 6 μm diamond suspension, a 3 μm alumina suspension and finished with a 0.5 μm alumina suspension to a mirror like surface finish to observe the microstructure across the weld.

Etching with 2% nital solution (2% nitric, solvent of alcohol) was used to reveal the weld microstructures, which proximately display the weld pool shape. Microstructures of the joints were examined using Pax-it software in conjunction with

optical microscopy to capture and measure the weld pool's shape and dimension. Some etched specimens for metallurgical analysis are shown in Fig. 3.12. The weld profile was examined at 5 x magnification to check the weld penetration and measure the weld pool dimensions. Microstructural details were observed at a higher magnification, e.g., 50x.

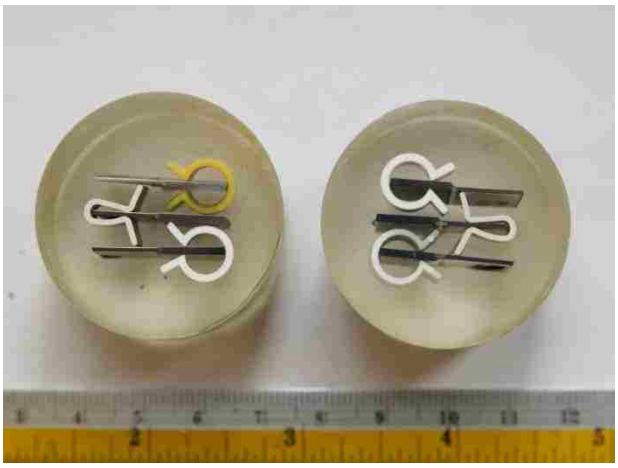

Figure 3.12 Metallurgical analysis specimens

3.5 Micro Hardness Testing

Microhardness tests were performed on the etched specimens. Hardness testing was carried out using a Leco Model M-400 microhardness unit with a 100g-200g load (Fig. 3.13). Hardness was measured at the center of the fusion zone and across the heat-affected zone (HAZ) into the base metal to estimate local mechanical properties.

Figure 3.13 Microhardness machine

CHAPTER 4

Numerical Simulation

During the last decades developments in welding simulation have lead to more realistic welding models, from simple 2D to more and more complex 3D models. In this chapter, the theory of the finite element analysis techniques used in welding is reviewed.

4.1 Finite Element Analysis of Welding

Finite element analysis (FEA) has been used by many authors to perform welding simulations to predict weld pool shape in different types of joints and materials [26 - 27]. Due to the complexity of welding processes, prediction of temperature distribution, distortion and residual stress are very difficult. Therefore, modeling of the welding process must be included for such effects and moving heat sources.

For the simulation of the temperature distribution, the commercial welding FEA package SYSWELD was employed [18]. In Fig. 4.1, a schematic diagram depicts the procedure to calculate the heat fluxes for FE transient thermal analysis of the welding process. The geometry of the butt weld joint is generated from SYSWELD software and defined material properties supplied with the software, welding process with heat source parameters, and thermal boundary condition while the maximum heat intensity calculated from Maple software [38], is added in SYSWELD at welding process section. The nodal values calculated during thermal analysis were used as a predefined

field for mechanical analysis in order to determine the distortions and residual stress state induced by welding.

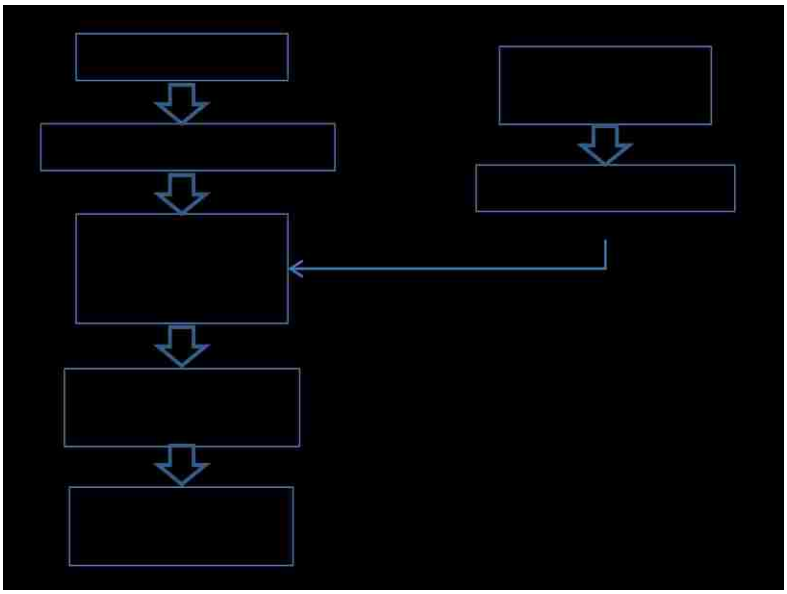

Figure 4.1 Schematic diagram of calculate the heat fluxes

4.1.1 Finite Element Meshes

In this work, the type of welding joint of interest is the butt joint. The butt joint welding simulation models the joining of two thin sheets with different thicknesses and materials. The weld zone is modeled as a solid deformable body in the finite element simulation with the same properties as the parent sheets. The geometry of the weld structure was modeled using the pre-processor of the SYSWELD code. The size of the simulated thin sheet is 50 mm x 20 mm, with two different values for the sheet thickness, 0.64 mm and 1.2 mm, respectively. The dimensions of the butt joint are depicted in Fig. 4.2. Three dimensional volume elements having eight nodes and three degrees of freedom per node were utilized. The model depicted in Fig.4.2 consisted of

51,138 nodes and 77,624 elements as shown in Fig. 4.3. The accuracy of the finite-element method depends upon the density of the mesh. The temperature around the laser beam is higher than the boiling point of the material, and it drops sharply in regions away from the molten pool. Therefore, a fine mesh is required in the area along the weld line and a coarse mesh is located away from the weld line (Fig.4.3).

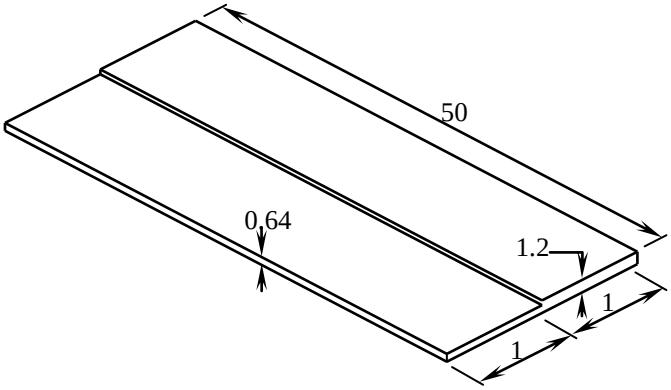

Figure 4.2 Butt-joint sheet dimensions

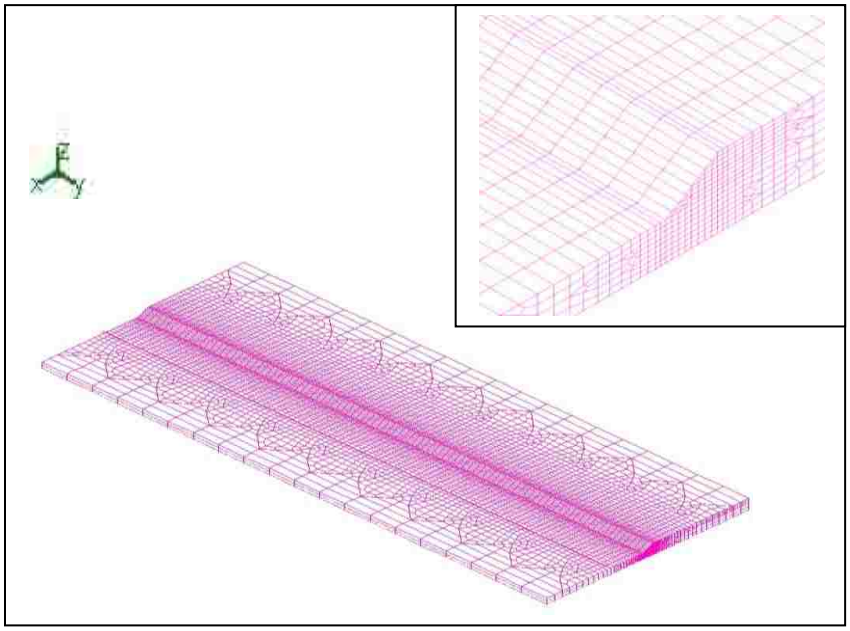

Figure 4.3 Butt-joint finite element mesh

4.1.2 Heat Source Models

The heat source model plays an important role in achieving the precise application of heat flux, which helps to accurately predict the required weld pool shapes and desired thermal histories. The heat source can be applied on the surface as a Gaussian power distributed thermal energy density and a volume such as a conical and ellipsoid heat source (Fig. 4.4). To be even more realistic heat source can be combined. A heat source in the shape of a double ellipsoid is appropriate for the simulation of TIG welding processes, whereas a conical source is more appropriate for laser beam and electron beam welding processes [18].

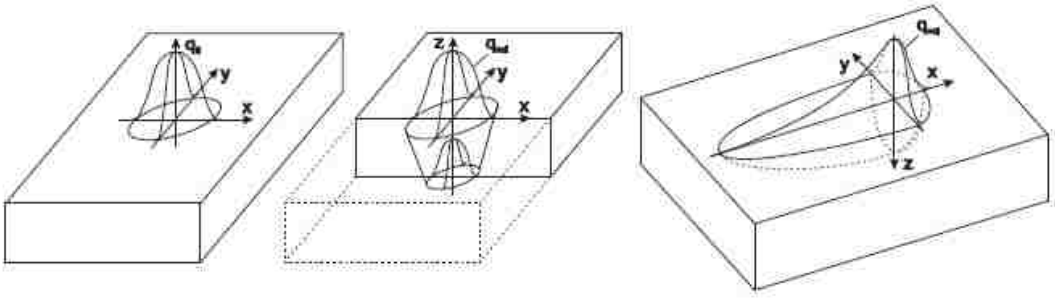

Figure 4.4 a. Gaussian distributed thermal energy density b. Conical volumetric heat source c. Double Ellipsoid volumetric heat source

In some cases, the selection of an appropriate model is not obvious. Although a conical heat source may be used for simulation of the full penetration laser welding process, it does not reflect the action of surface tension on both the top and bottom weld pool surface, so it is not suitable for modeling hourglass-like weld pool shape.

4.1.2.1 Hourglass Heat Source

During the welding process, the flow of molten metal is unstable and complex. It is known that the distribution of pressure and shear force from the effect of surface tension at the both the top and bottom weld pool surface cause the hourglass shape. The existing heat source models cannot predict the weld pool shape from these effects, especially that of surface tension. Thus, the heat source model is developed to fix this problem called the hourglass heat source. The three-dimensional hourglass heat source is a volumetric heat source that best simulates the heat source distribution along the workpiece thickness when full penetration welds are considered in the thin metal sheets. As shown in Fig. 4.5, the heat intensity region begins at the top surface of workpiece and decreases to the minimum at a core (transition point) of hourglass shape inside of the workpiece, and increases again after towards the bottom surface of the workpiece. Along the thickness of the workpiece, the diameter of the heat density distribution region is modeled as linearly decreasing and increasing, respectively. But the heat density at the central axis (z-direction) is kept constant. At any plane perpendicular to the z-axis, the heat intensity is distributed in a Gaussian form. Thus, the three-dimensional hourglass heat source used in this study is the addition of two Gaussian heat sources with different distribution parameters and the same central maximum values of heat density along the workpiece thickness. In this way, the heating action of the laser beam through thin sheet metal workpieces is best simulated.

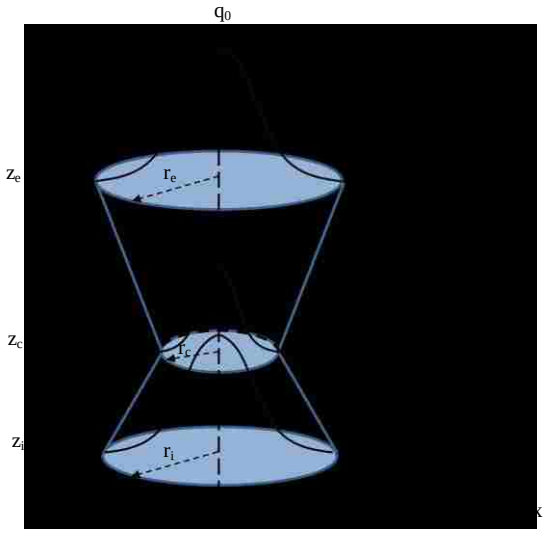

Figure 4.5 hourglass heat source

At any plane perpendicular to the z-axis, the heat intensity distribution may be written as [39]

$$Q(x,y,z) = Q_o exp\left(-\frac{x^2+y^2}{r^2(z)}\right) \tag{4.1}$$

where r_o is given as

for $z_c \leq z \leq z_e$

$$r_o(z) = r_e - \frac{r_e - r_i}{z_e - z_i}(z_e - z) \tag{4.2}$$

$z_i \leq z < z_c$

$$r_o = 2r_i - \frac{(r_e - r_i)(z_e - z)}{(z_e - z_i)} \tag{4.3}$$

Q is the source intensity, Q_o is the maximum heat intensity, r_e is the (x,y) parameter of the Gaussian curve in the upper plane at z=z_e, r_c is the (x,y) parameter of Gaussian

curve in the core plane at $z=z_c$, and r_i is the (x,y) parameter of Gaussian curve in the upper plane at $z=z_i$,

The parameters of the heat sources are adjusted in a way that the result is approximately the shape of the molten zone measured in from the experimental results. The sample values used in this study are given in Table 4.1.

Table 4.1 Value of the hourglass parameters used for simulation

Parameter	Q_o (W/mm^3)	r_e (mm)	r_c (mm)	r_i (mm)	z_e (mm)	z_c (mm)	z_i (mm)
Value	10230	0.4	0.1	0.34	0	-0.5	-0.9

Note; the minus sign of z_c and z_i is due to the presence of the support the top surface, during welding.

The power intensity, Q_o is calculated with

$$Q_0 = \frac{\eta P}{\int f_1 dV_1 + \int f_2 dV_2} \tag{4.4}$$

where η is the thermal efficiency, P is the laser power, f_1 and f_2 are $exp\left(-\frac{r^2}{r_0^2}\right)$ for the upper cone and the lower cone, respectively, a FORTRAN function of the x-y-z coordinate of conical source with a Gaussian power density distribution in the range of r_e - r_c, and r_c - r_i , respectively, V_1 and V_2 are the volume of upper and lower conical source, respectively. The complete derivation is shown in Appendix.

4.1.2.2 Double Ellipsoid Heat Source

For the arc welding heat source, a 3D double ellipsoidal heat source developed by Goldak is often used in arc welding simulation [10]. The heat source model has proven to be more stable and accurate than a point or a line heat source model, especially for welding with moving heat source. [28] The total heating rate (P, power) from the arc welding torch is simply expressed as

$$P = \eta VI \tag{4.5}$$

where η is the arc welding efficiency, which depends on the metal, V and I are applied voltage and current given as 8-10V and 20-25A. For low carbon steel arc welding, the arc efficiency measured as a function of welding current shows little variation over the current range tested. The arc efficiency is assumed to be 70% for carbon steel [30]. In this research all welding parameters were predetermined as given in Table 4.2, and the residual stresses and welding distortions were computed numerically as an output of the simulation.

The 3D double ellipsoidal heat equation is a well-known numerical heat input model for arc welding in computer-based simulation [30]. The geometrical shape of the weld pool has two individual one-half ellipsoids, and is described in Fig. 4.6. The feed wire is assumed to be completely molten by the fusion of metal due to the applied heat input. The heat input source induces the temperature to rise over the liquidus point, and the molten beads are expected to be in the fusion zone (FZ). Similar to the FZ, the

partially melted zone (PMZ) is located outside the FZ as the temperature falls. The PMZ is defined by the temperature distribution that is above the solidus, but below the liquidus point [31].

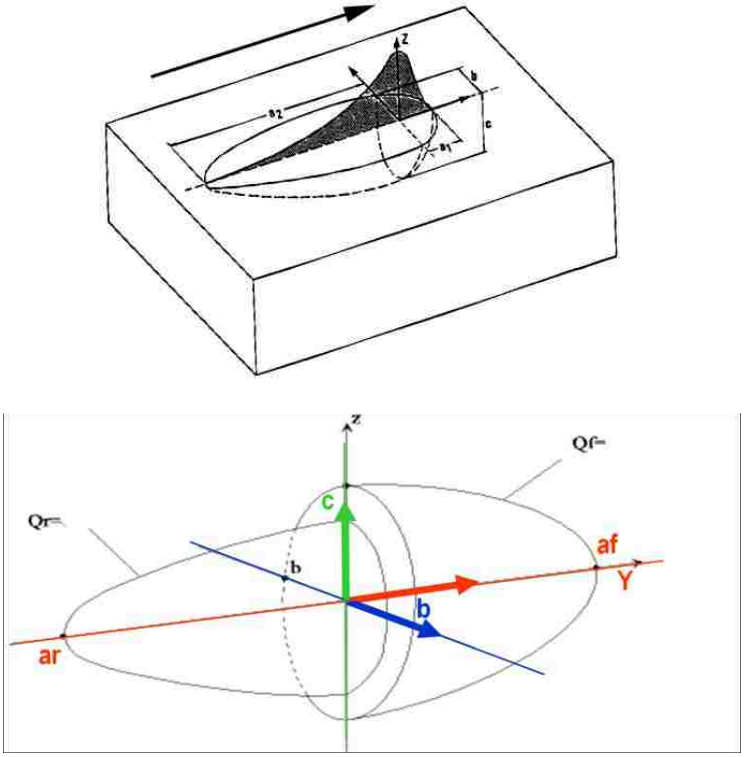

Figure 4.6 3D Double Ellipsoidal Moving Heat Source [30]

The melt pool shape is dependent on welding parameters: intensity of heat input, and welding speed. In the TIG welding process, Goldak's double-ellipsoid heat source model [28] is adopted to calculate volumetric heat flux distributions as heat input around the welding pool. The heat source distribution consists of two different ellipses: one in the front quadrant and the other in the rear quadrant of the heat source. The total power densities from both Q_f and Q_r describing heat flux distributions inside the front and rear quadrant of the heat source can be expressed as [28]:

$$Q_f(x,y,z) = \frac{6\sqrt{3}f_f P}{a_f bc\pi\sqrt{\pi}} e^{-3\frac{x^2}{b^2}} . e^{-3\frac{z^2}{c^2}} . e^{-3\frac{y^2}{a_f^2}} \tag{4.5}$$

$$Q_r(x,y,z) = \frac{6\sqrt{3}f_r P}{a_r bc\pi\sqrt{\pi}} e^{-3\frac{x^2}{b^2}} . e^{-3\frac{z^2}{c^2}} . e^{-3\frac{y^2}{a_r^2}} \tag{4.6}$$

where Q is the power density [W/mm^3]. a_f, a_r, b, and c are Goldak's parameters related to the shape and the fraction of the molten zone [mm]. a_f stands for the frontal distance from the center of the melt pool; a_r is the rear portion along the welding direction. The determination of the length a_r is related to the welding velocity; a longer a_r is given for a faster velocity. b and c reflect half of the width and depth in the melt pool. f_f and f_r are Goldak's fraction parameters of power sent from the heat source center to the front and to the rear in the molten zone, with $f_f + f_r = 2$ [28]. x and z are horizontal and vertical locations of the moving heat source in Cartesian coordinates.

The transformation relating the fixed (x,y,z) and moving coordinate system (x,ξ,z) is:

$$\xi = y + v(\tau - t) \tag{4.7}$$

where y is the location of the moving heat source along the welding line. t is the time at which a point is at the center of the moving heat source. v is the welding speed. The shape of the melt pool is usually obtained through experiments; however, in this

simulation, Goldak's parameters are the main factors deciding the dimension and shape of the melt pool. The coordinate transformation, Eq.4.7, can be substituted into Eq. 4.5, combined with Eq. 4.6.

$$Q(x,y,z,t) = \frac{6\sqrt{3}\, f_{f,r}\, q}{a_{f,r} b\, c\, \pi\sqrt{\pi}} e^{-3x^2/b^2} e^{-3z^2/c^2} e^{-3(y-vt)^2/a_{f,r}^2} \quad (4.8)$$

Table 4.2 TIG welding parameter

Parameters [Unit]	Welding Speed [mm/s]	Length of Weld [mm]	Voltage [V]	Current [A]
Values	0.9-1.3	170	8-10	20-25

Definition of double ellipsoid heat source parameters used in the calculation is shown in Table 4.3.

Table 4.3 Value of the double-ellipsoidal parameters used for simulations

Parameter	P (W)	a_f (mm)	a_r (mm)	b (mm)	c (mm)	f_f (mm)	f_r (mm)
Value	170	2.25	3.75	1.5	1.5	0.6	1.4

4.1.3 Boundary Conditions

During the welding process, the specimen was subjected to both thermal and mechanical boundary conditions. The suitable boundary conditions, representative of actual experimental conditions bring more accuracy to the computational results.

4.1.3.1 Thermal Boundary Conditions

On the boundary of the simulation model should be satisfied. In this study, three types of thermal boundaries were considered. A schematic representation of the thermal boundary conditions is shown in Fig. 4.7. Free convection and radiation are presented at the surfaces where the surface is exposed to the atmosphere. Thermal conductance is present at the interface of the sample and the base support as well as the edge of the sample.

Type A:

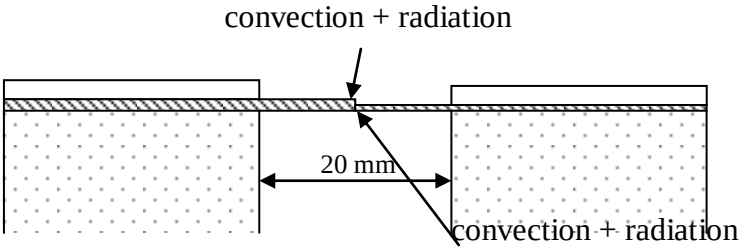

Type B:

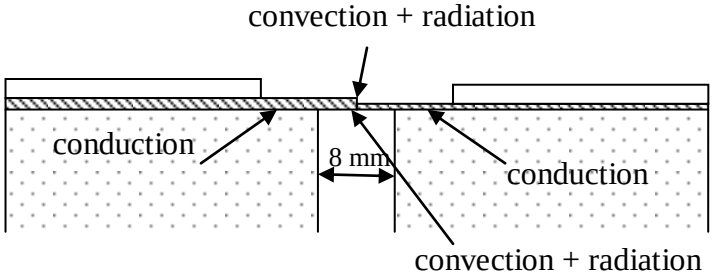

Type C:

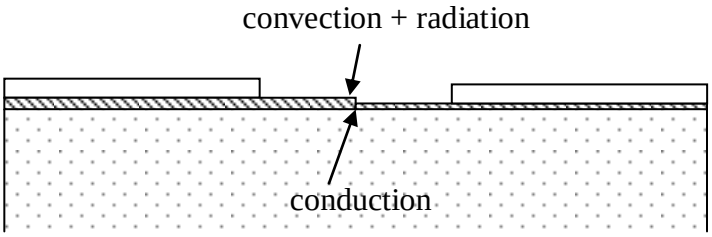

Figure 4.7 Schematic representation of thermal boundary conditions

The surfaces of the model exposed to the environment were subjected to convection and radiation heat loss (convective coefficient of 25 W/m^2K), while the surfaces that contact the support base plate were subjected to conduction loss with a thermal conductivity coefficient of 58 W/m-K. The initial ambient temperature was assumed to be 20 ^oC.

4.1.3.2 Mechanical Boundary Condition

The clamped boundary condition is the main variable for determining the correct residual stresses and distortion. The specified mechanical boundary conditions must in all cases be sufficient to prevent rigid body motion of the model. Two sheet metal halves were "rigidly" clamp down along longitudinal direction far from the weld line of 10 mm (weld line to front edge of clamping) using magnetic clamp system for the laser welding case. All the three translational degrees of motion were set to zero, to simulate rigid clamping. The zones where the clamping tools were actually applied in the experiments were fixed with rigid constraints. Fig. 4.8 depicts the specified zero displacement conditions for the butt joint weld simulations.

In the real welding process, the clamping tools were released after welding. Therefore, the mechanical simulation also calculated the displacement and stresses after cooling and unclamping. For unclamping, only rigid body motions are applied. The part is "clamped" in a statically determinate manner. To block rigid body motion three nodes are clamped perpendicular to the plane (UZ). Two of these nodes need additional clamping in order to prevent the rotation around an axis perpendicular to the plane

(UY). One of these nodes needs another additional clamping in order to prevent the translation along the axis perpendicular to the plane (UX). The mechanical constraint for the unclamping condition is shown in Fig. 4.9.

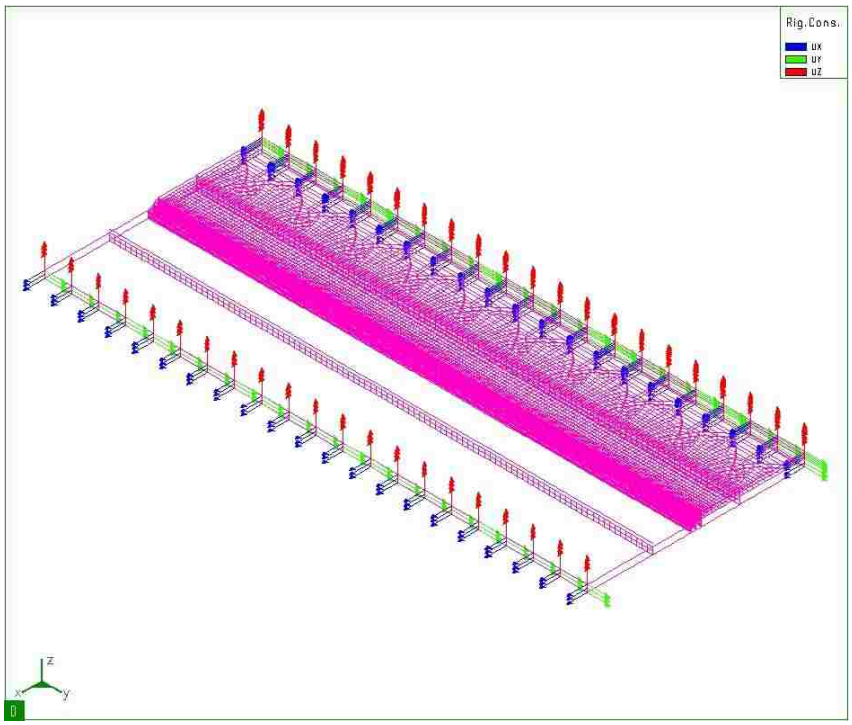

Figure 4.8 Mechanical constraints for butt joint

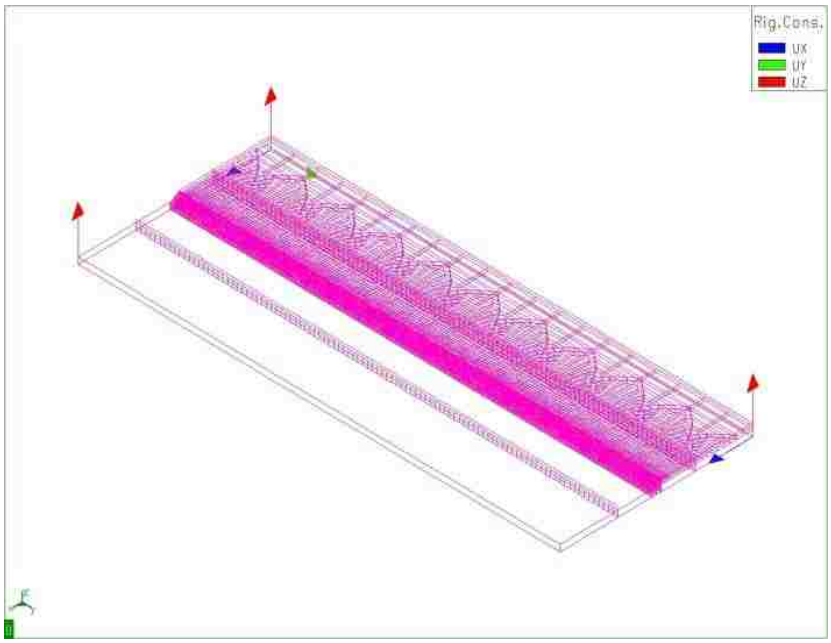

Figure 4.9 Mechanical constraints in case of unclamping

4.2 Material Properties

The material properties were considered to be functions of temperature. The thermal and mechanical material properties of low carbon steel DC04 and TRIP700 with varying temperature dependent properties are presented in Fig. 4.10 - 4.13 [29], respectively. The melting temperature of DC04 and TRIP700 is 1505 ^{o}C.

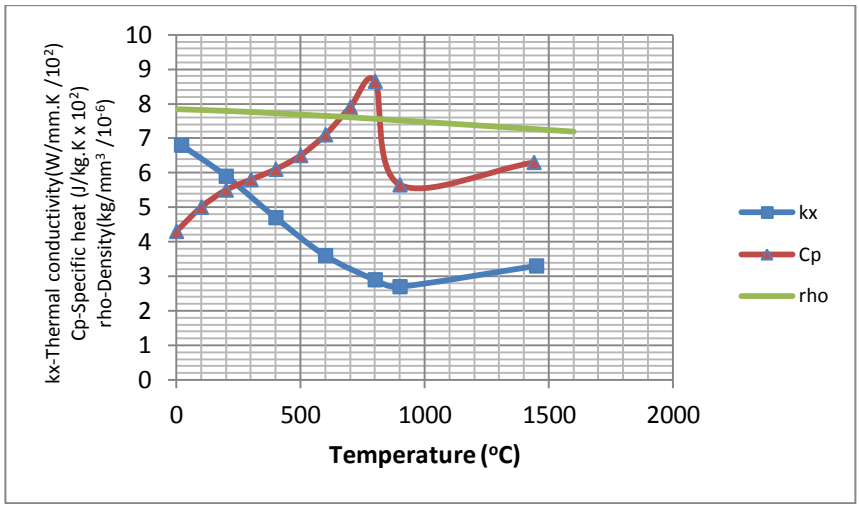

Figure 4.10 Temperature dependent thermal properties for DC04

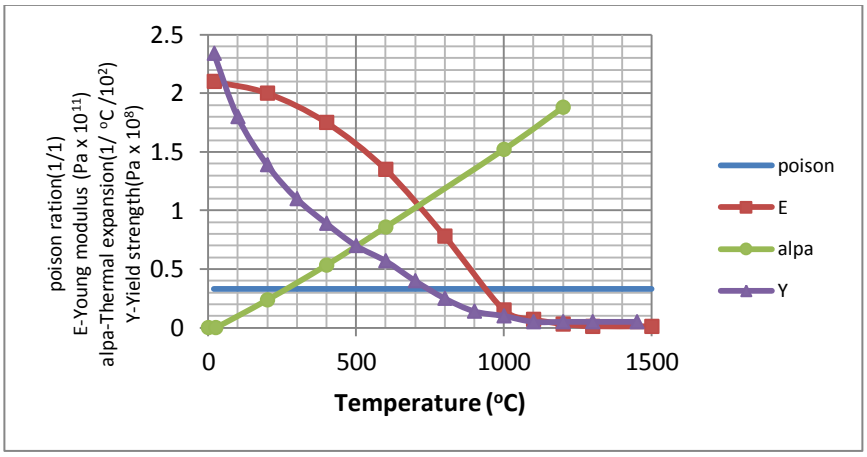

Figure 4.11 Temperature dependent mechanical properties for DC04

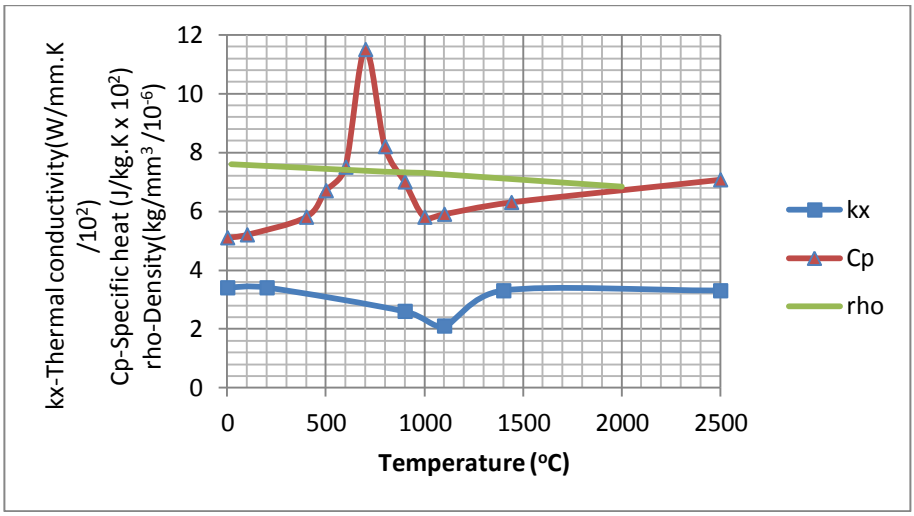

Figure 4.12 Temperature dependent thermal properties for TRIP-700

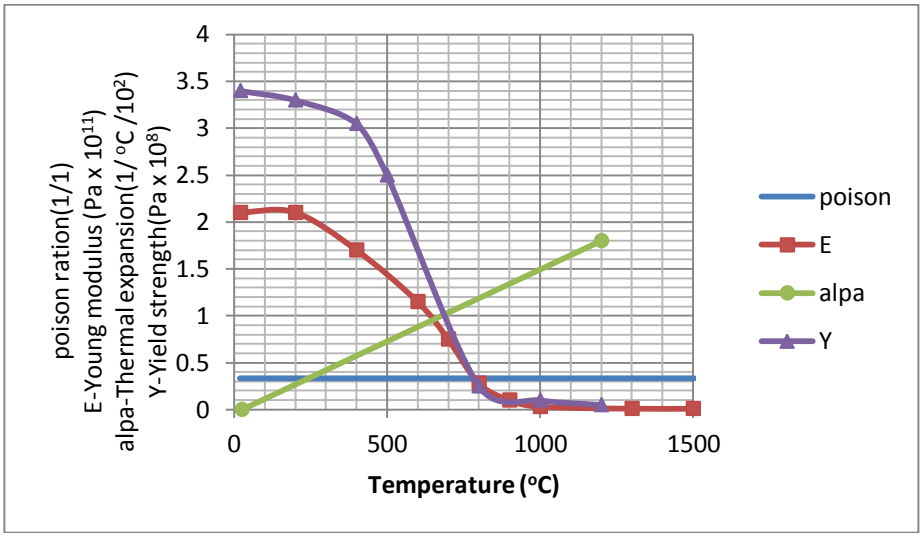

Figure 4.13 Temperature dependent mechanical properties for TRIP-700

CHAPTER 5

Laser Welding Simulation Results

In this chapter two main results, laser welding experimental and simulation results, are described and compared.

5.1 Laser Welding Experimental Results

Visual investigations, tensile tests, and hardness tests were carried out to evaluate the performance and mechanical properties of the weld.

5.1.1 Visual investigation

Fig. 5.1 – 5.6 shows the top and bottom views of the laser-welded butt joints obtained in the experiments. At the bottom view the weldment can be observed. There was no spatter and porosity from welding with the laser welding process. The weld shape is narrow and smooth and the width of weldment is approximately 1 mm. The welding area (dark area) of the uncoated sheet (cold roll steel without zinc coating) is wider than the coated sheet (galvannealed steel). A sound weld with complete penetration was achieved without any spatter or porosity.

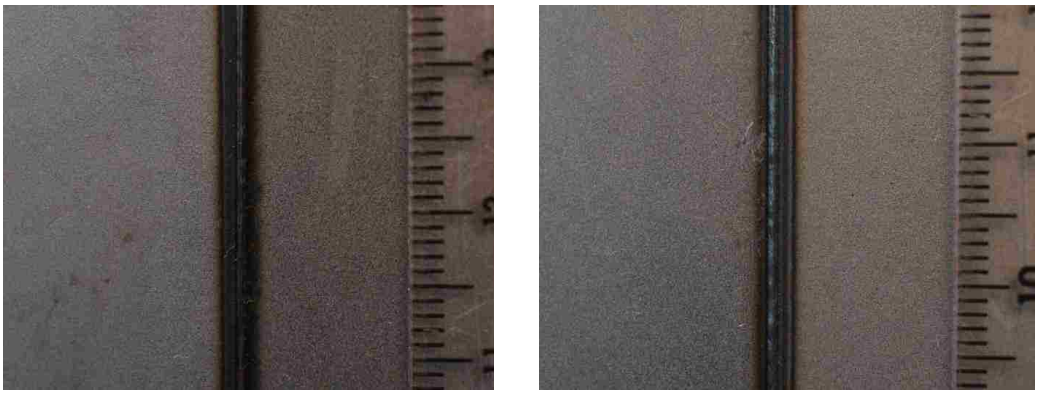

a) Top surface b) Bottom surface

Figure 5.1 The laser butt joint for ASML1

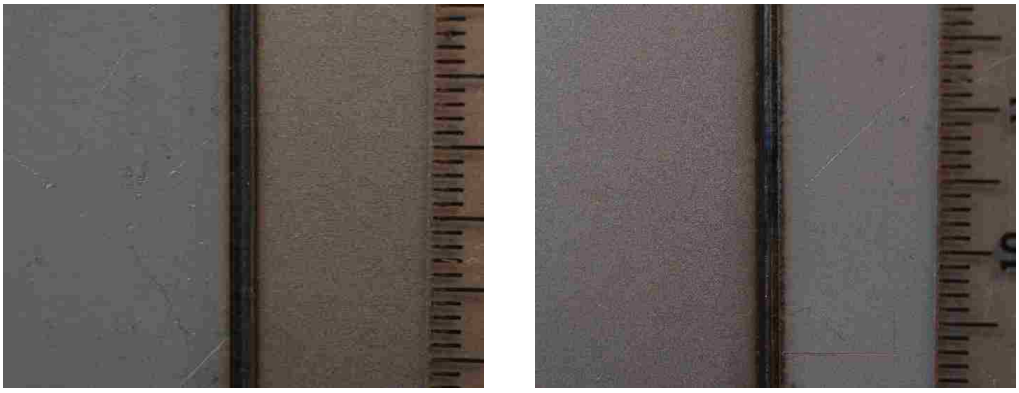

a) Top surface b) Bottom surface

Figure 5.2 The laser butt joint for ADML1

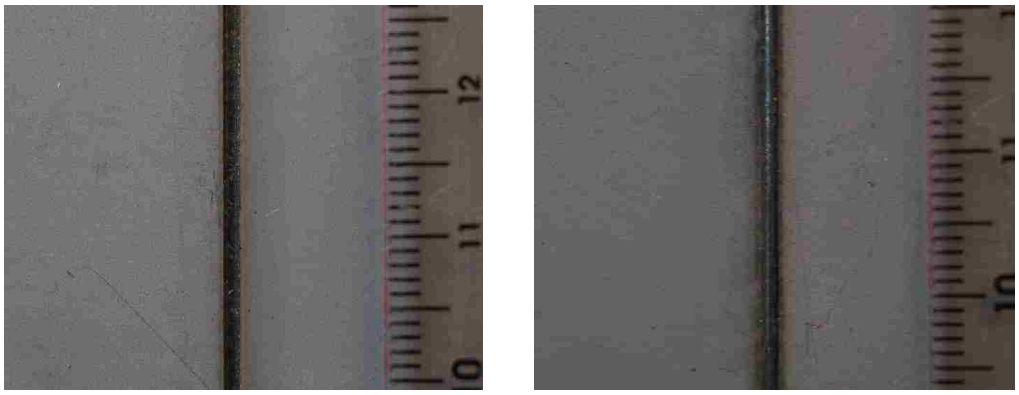

a) Top surface b) Bottom surface

Figure 5.3 The laser butt joint for ASML2

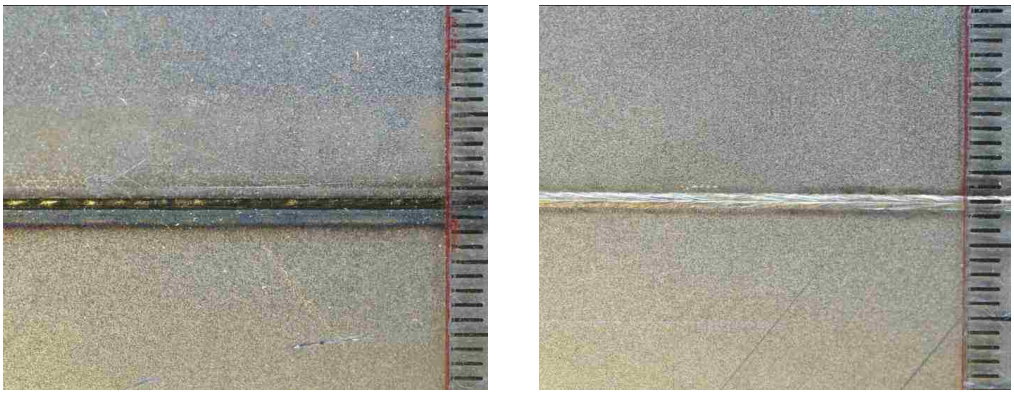

a) Top surface b) Bottom surface

Figure 5.4 The laser butt joint for BSML1

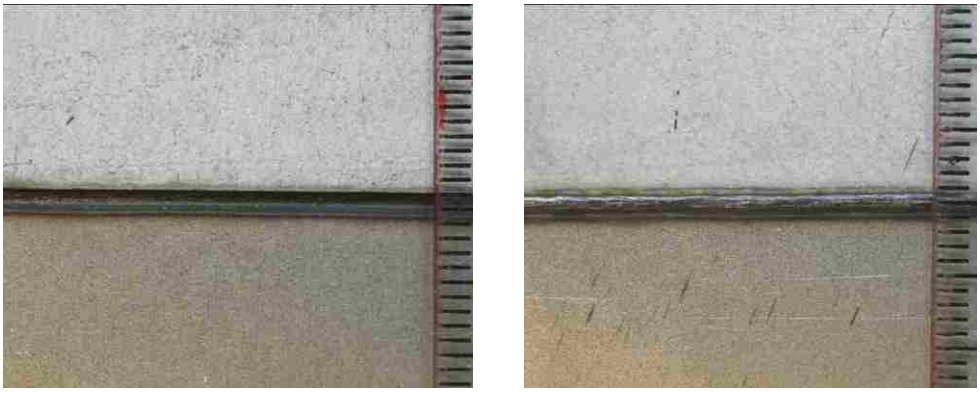

a) Top surface b) Bottom surface

Figure 5.5 The laser butt joint for BDML1

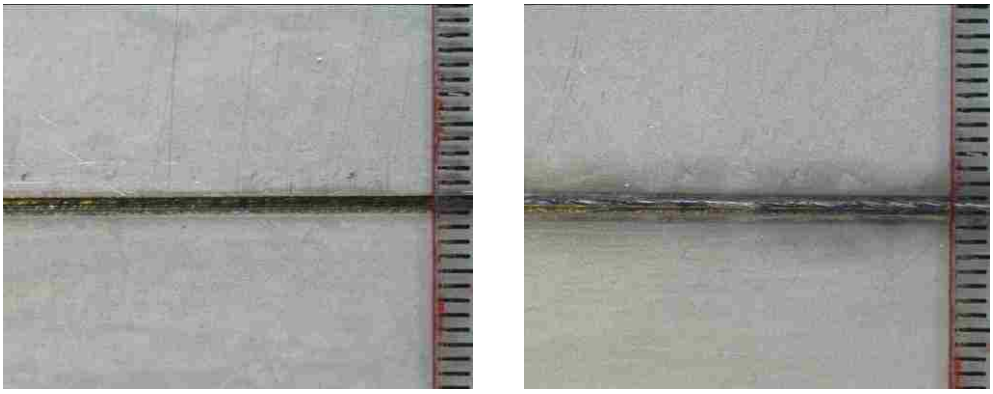

a) Top surface b) Bottom surface

Figure 5.6 The laser butt joint for BSML2

5.1.2 Tensile Stress Test

The uniaxial tensile tests were performed on the base metal sheet (i.e. thinner base metal sheet) and laser-welded metal sheet until fracture occurred.

Images of tensile specimens before testing compared to after testing are shown in Fig. 5.7. The fracture of the base metal specimens occurred at the center, whereas the laser-welded metal specimens had fracture occur near the center of the thinner side, within the gauge length in all cases (Fig. 5.8). Both the base metal and the laser-welded metal specimen show a ductile shear failure mode where the fracture surfaces are inclined at 45^{o}. The deformation can be considered to be under plane stress loading conditions, since the thickness of the specimen is much less than the width. This form of ductile fracture occurs in stages that initiate after necking begins, where small microvoids form in the interior of the material and enlarge to form a crack continuing to grow and spreads laterally towards the edges of the specimen. Finally, crack propagation is rapid along a surface that makes about a 45^{o} degree angle with the surface. Noticeably, the crack did not initiate at the weld zone when it is deformed in tension. Table 5.1 lists the mechanical properties in the tensile testing of the un-welded metal sheet (base metal) and the laser-welded metal sheet. The tensile strength of the laser-welded sheet specimens are higher than the mean value of those of un-welded sheet specimens. All laser-welded specimens have higher UTS compared to the base metal due to the presence of weld. Hence, the true stress-strain curves of as-welded sheet specimens are higher than those of the base metal sheet specimens.

The tension load and displacement curves obtained from the experiments for the un-welded specimens and laser-welded specimens are shown in Fig. 5.9. The ductility of coated sheet (galvannealed sheet) is observed to be higher. The comparison of tensile strengths, is shown in the graph shown in Fig. 5.10 between the laser-welded specimens and the base metal specimens. The tensile results of the additional laser-welded specimens were shown in Fig. 5.11.

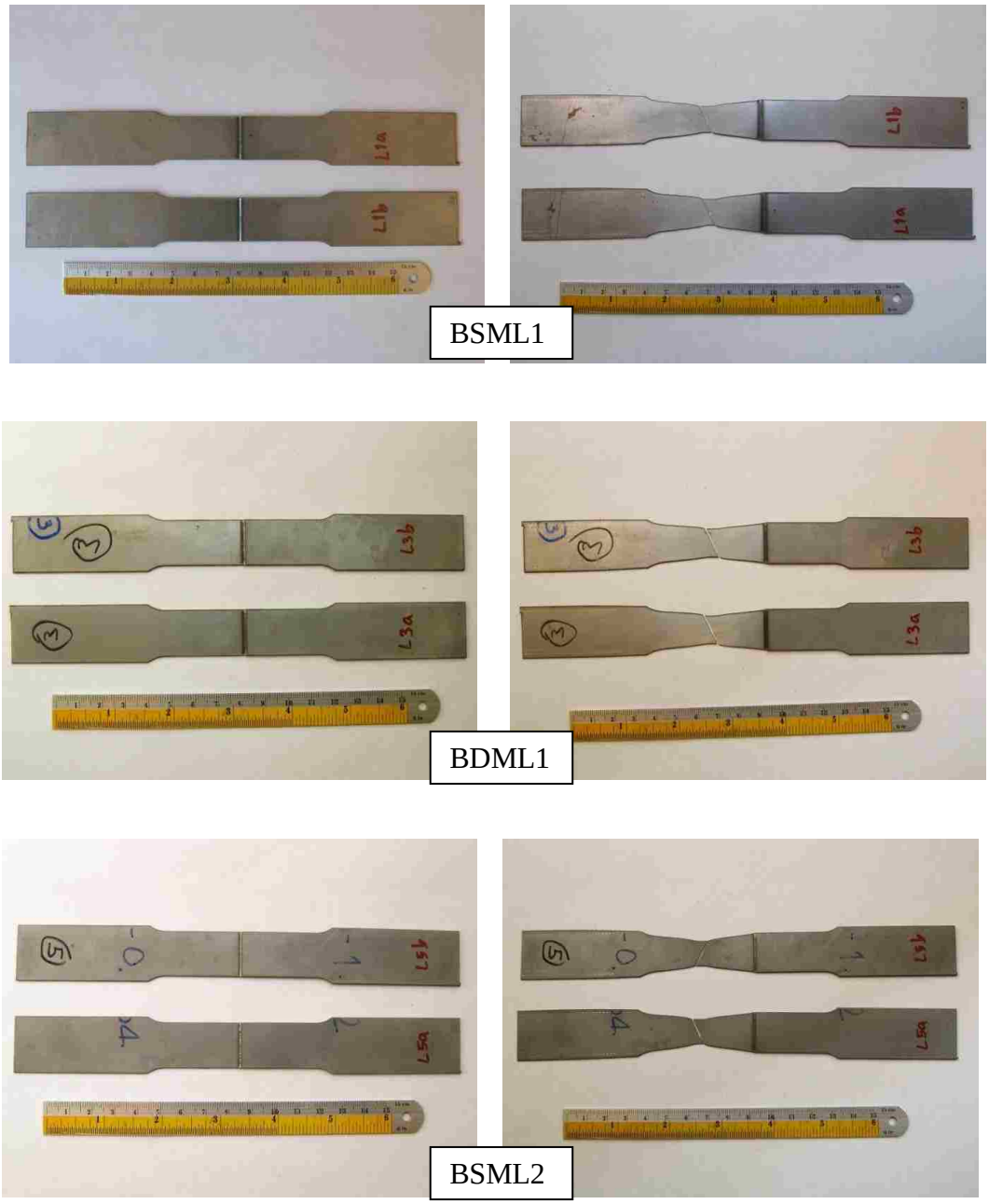

a. Before testing b. After testing

Figure 5.7 Comparison of the tensile specimens before and after testing

Figure 5.8 Failure location of the tensile test specimens

Table 5.1 Tensile test of the sheet specimens

Specimen No.	Cross-section area (mm^2)	Ultimate Tensile (N)	Tensile Strength (N/mm^2)
1-Base Metal	12.76	4122	323.00
ASML1	12.71	4358	342.87
2-Base Metal	12.70	4230	332.97
ASML1	12.74	4318	338.87
3-Base Metal	12.80	4237	331.02
ASML1	12.74	4304	337.94
4-Base Metal	12.73	4141	325.30
ADML1	12.66	4201	331.85
5-Base Metal	12.70	4116	323.99
ADML1	12.72	4212	331.05
6-Base Metal	12.77	4188	327.84
ADML1	12.74	4302	337.61

7-Base Metal	12.70	3900	306.99
ASML2	12.72	3976	312.66
8-Base Metal	12.81	3862	301.57
ASML2	12.80	3966	309.84
9-Base Metal	12.73	3915	307.55
ASML2	12.76	4099	321.36
10-BSML1	12.71	3811	299.77
11-BSML1	12.76	3825	299.78
12-BSML1	12.76	3814	298.86
13-BSML1	12.74	3835	300.91
14-BDML1	12.73	4260	334.72
15-BDML1	12.76	4271	334.68
16-BDML1	12.76	4280	335.39
17-BDML1	12.78	4264	333.70
18-BSML2	12.74	3642	285.77
19-BSML2	12.79	3623	283.15
20-BSML2	12.78	3681	288.08
21-BSML2	12.71	3651	287.18

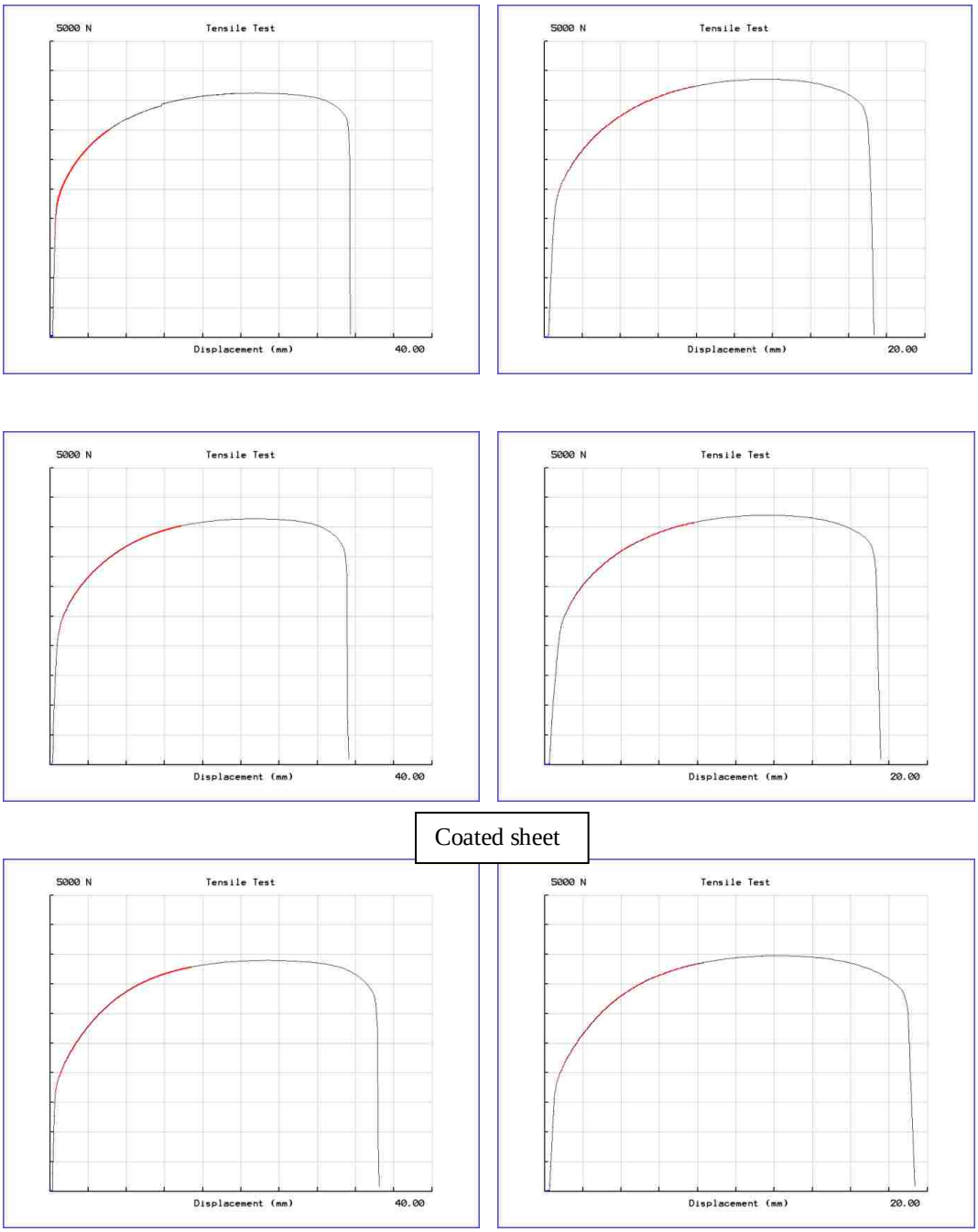

a. The base metal b. The laser-welded metal

Figure 5.9 Tension load-displacement curves (a) the base metal, (b) the laser-welded metal

The mechanical properties of cold-roll steel sheet are higher than the galvannealed steel sheet as a result of the fact that tensile strength of CR is higher than GA.

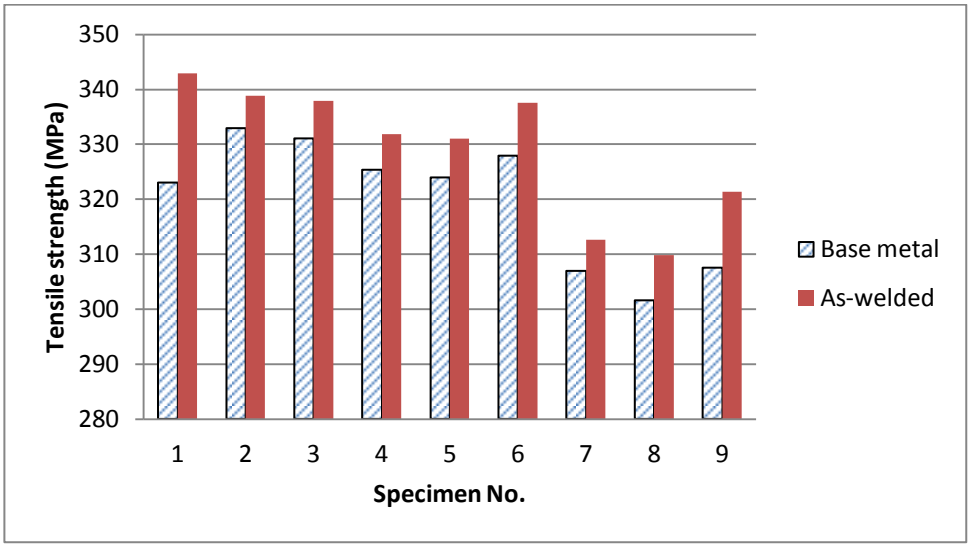

Figure 5.10 Tensile strength of the base metal and the laser-welded metal in group A experiments.

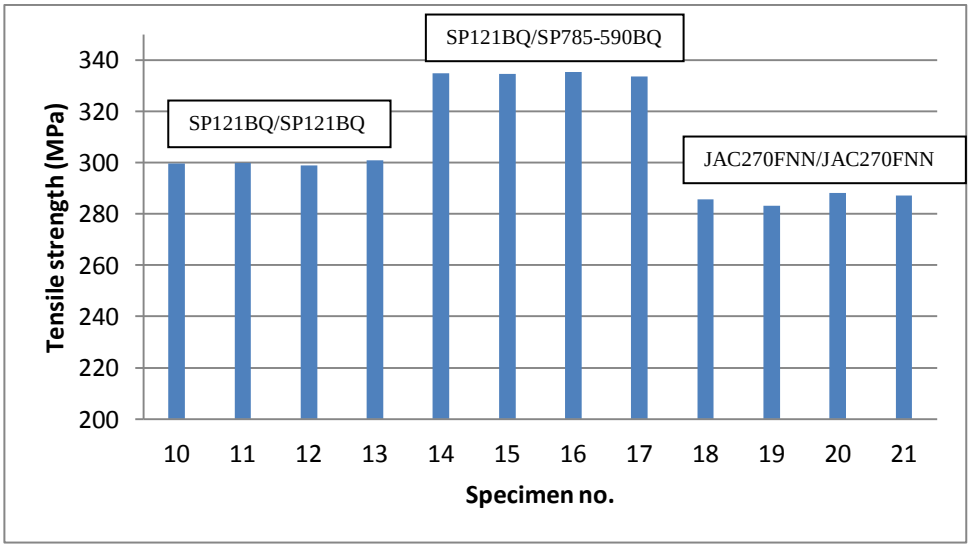

Figure 5.11 Tensile strength of the laser-welded metal in group B experiments.

5.1.3 Metallurgical Analysis

In the welding of unequal thickness steel sheets, the irradiation from the laser beam heat source is directed towards the uneven joint interface. Some portion of the melted thicker sheet will flow to the top of the thinner one, which leads to the formation of an inclined layer (Fig. 5.12). Although no specific thermal data was recorded from the experimental setup, the size and shape of this sort of weld pool was observed with metallurgical analysis.

The microstructures of the three zones (base metal, HAZ and fusion) are shown in Fig. 5.13. Here the fusion zone is defined as the region in which the weld metal and base metal are fused together and HAZ is the region adjacent to the weld, where the mechanical properties and/or microstructure have been altered by the heat of welding. Fig. 5.13 shows the cross section microstructures of TWB (ASML1) from the butt joint laser welding process. The images in Fig. 5.13 are from locations at start point, middle point, and end point. Interestingly, the butt joint becomes misaligned at the middle point and end point due to thermal expansion of the thin metal sheets. In some experimental results, the thick metal sheet moved up higher than the thin metal sheet as shown in Fig. 5.14. The reason is that the welded sheets were prone to buckling, since the welding length of the metal sheet is very high. Full penetration welds, with slight porosity was observed.

Ferrite and a mix of some bainite is observed in the fusion zone. The light region is ferrite, while the dark region is bainite (Fig. 5.15). Bainite formation is due to the rapid

heating and cooling rates in laser welding. Similar micro-structural features are observed in the coated (galvanized steel) and uncoated (cold roll steel) combination. The weld pool shape and microstructure for group B with power of 3,000 W using different combinations are shown in Fig. 5.16 - 5.18. The micrograph at higher magnification for BDML1 (SP121BQ/SP783-590BQ) displays martensite structure due to rapid cooling (Fig. 5.19).

The values for the weld pool dimension from the experiments are shown in Fig. 5.20. Table 5.2 summarized the weld pool shape measurements. These measurements were used to specify values for the hourglass heat source parameters during the welding simulation.

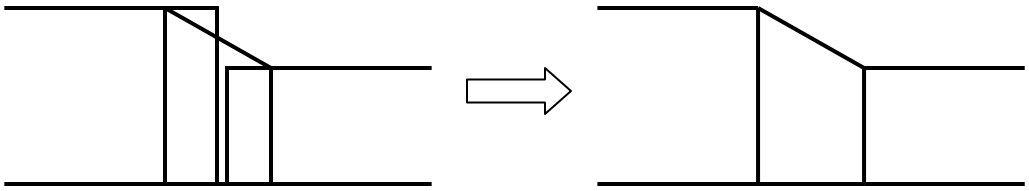

Figure 5.12 Metal compensation of butt welding on unequal thickness sheets.

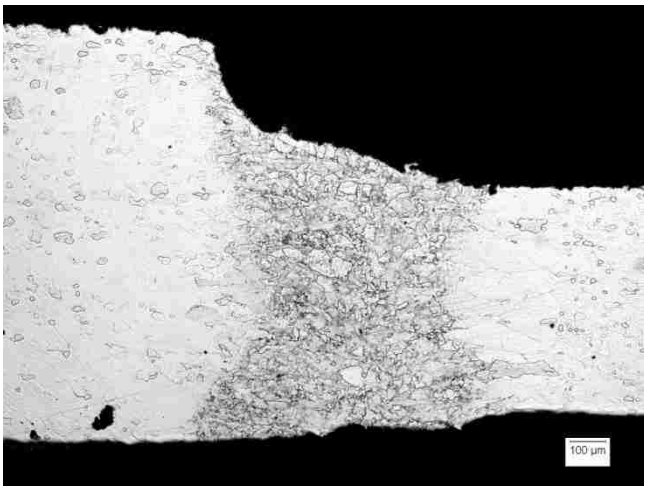

(a) Start point

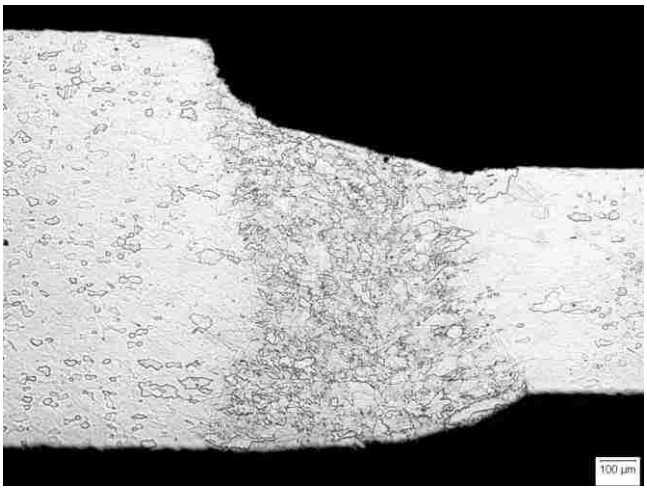

(b) Middle point

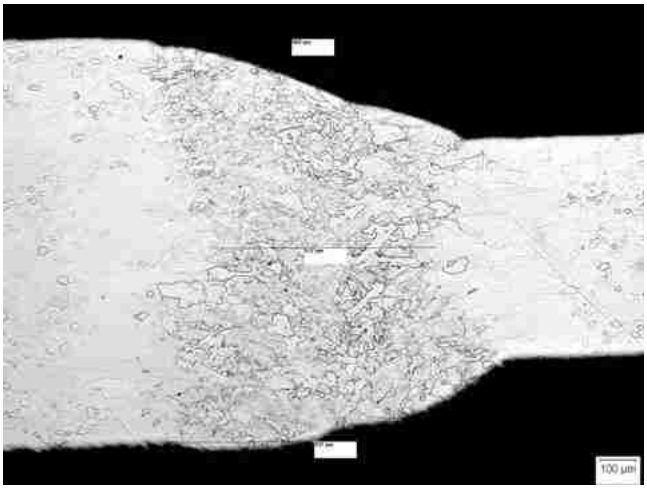

(c) End point

Figure 5.13 Microstructure of laser welding of ASML1 at different location: (a) Start point, (b) Middle point (c) End point

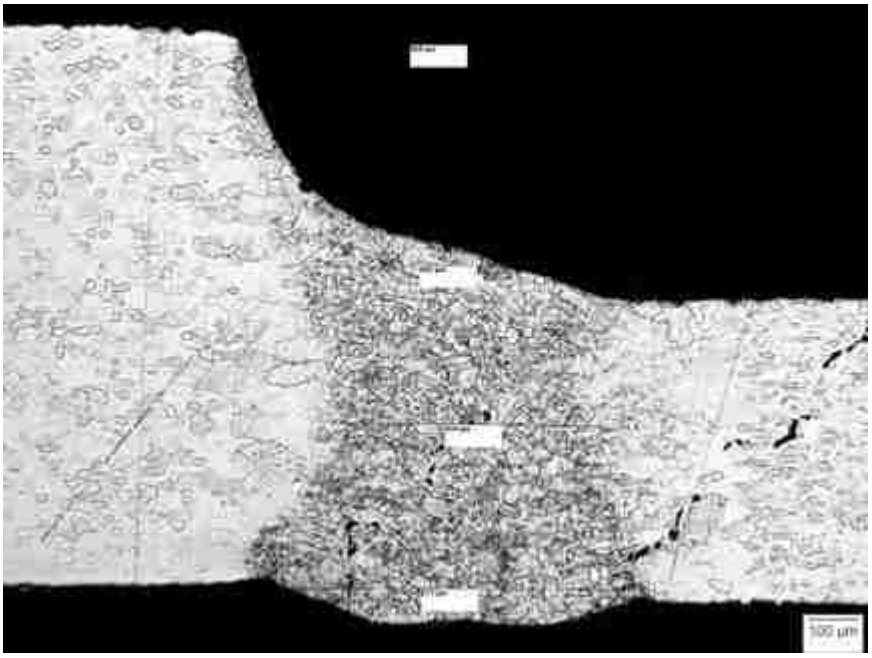

Figure 5.14 Microstructure of laser welding of ADML1 at end point.

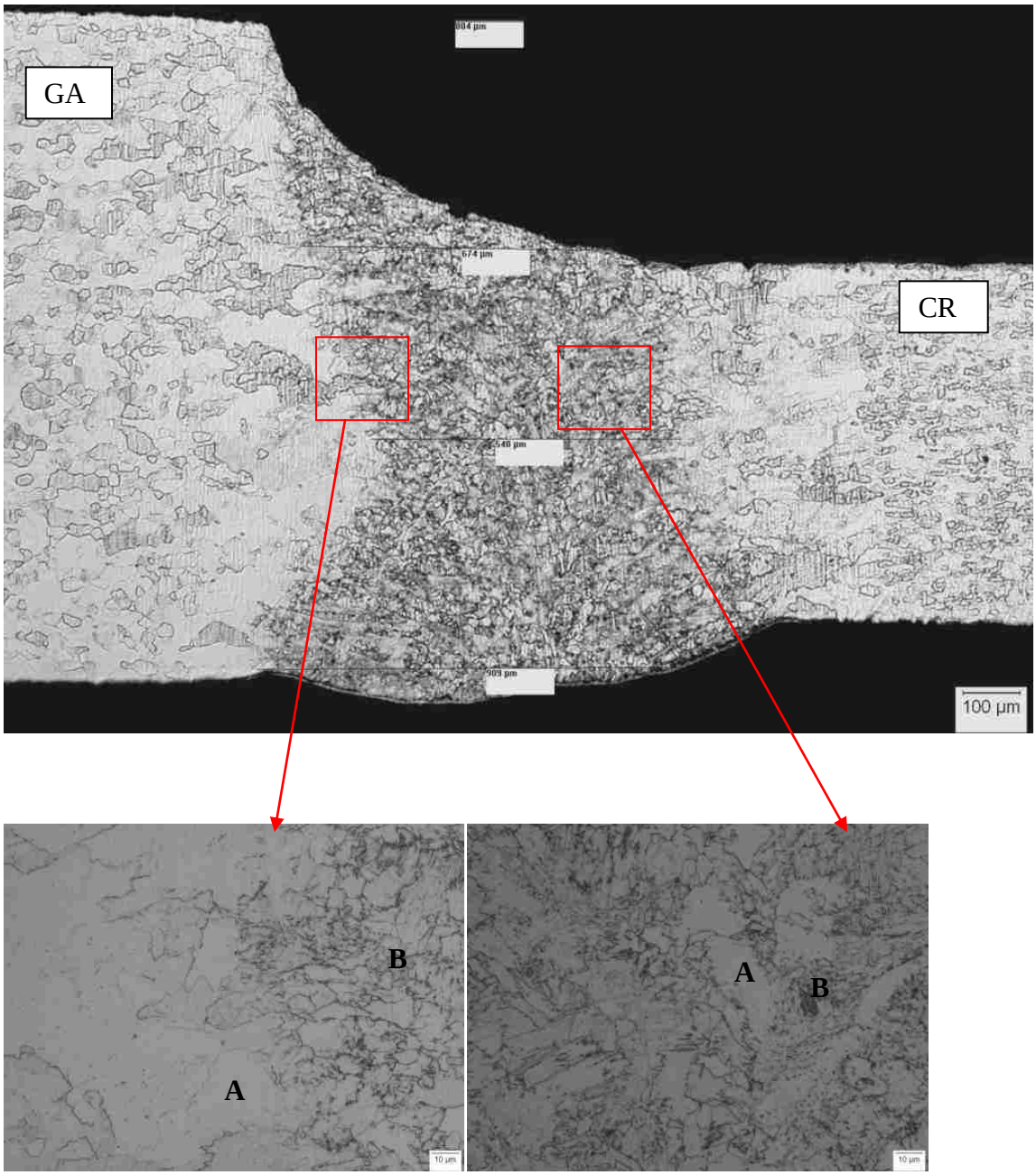

Figure 5.15 Micrographs showing typical weld metal microstructures in weld metal for ADML1 at middle point: A, Ferrite; B, Bainite.

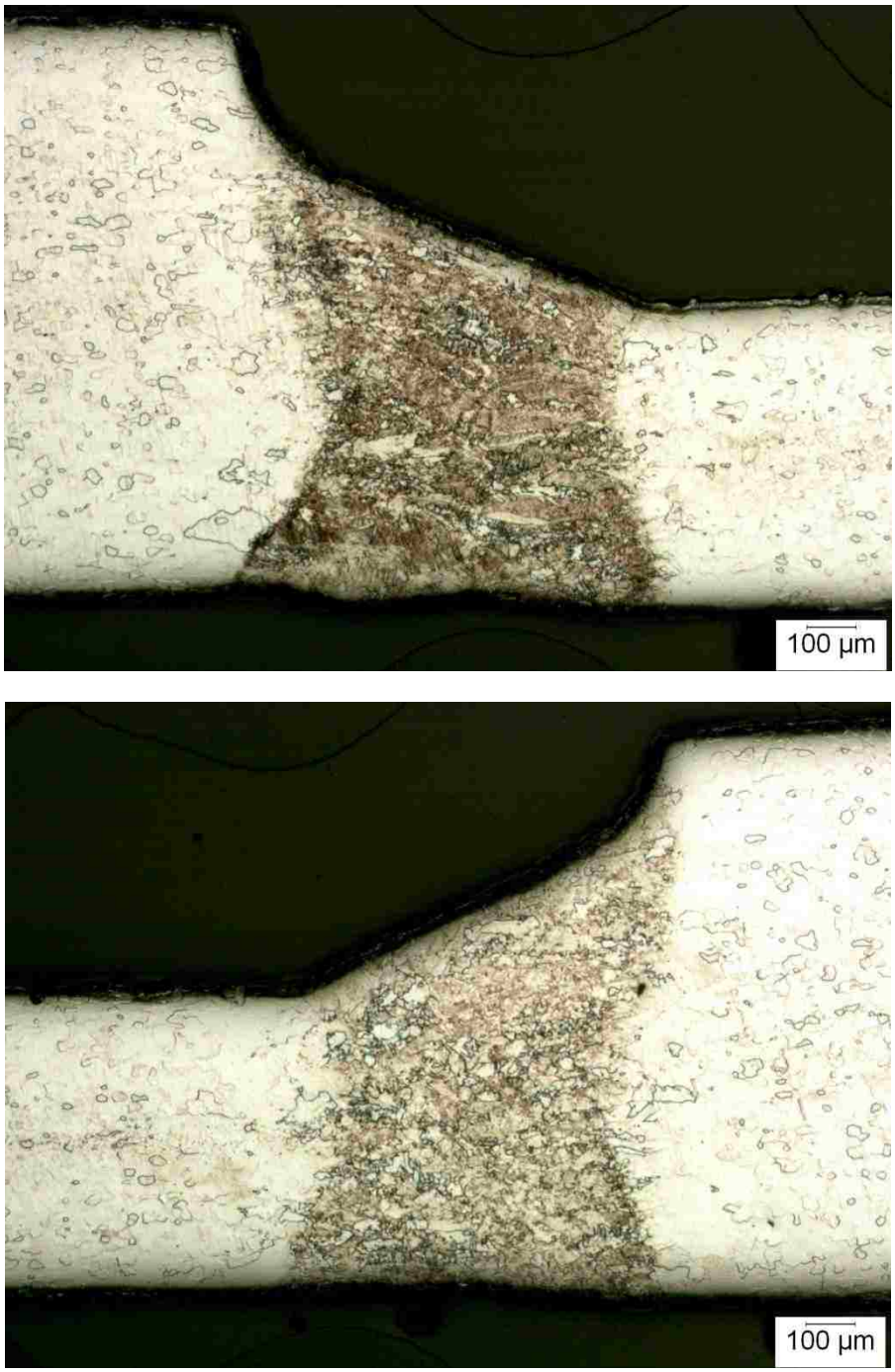

Figure 5.16 Microstructure of laser welding of BSML1

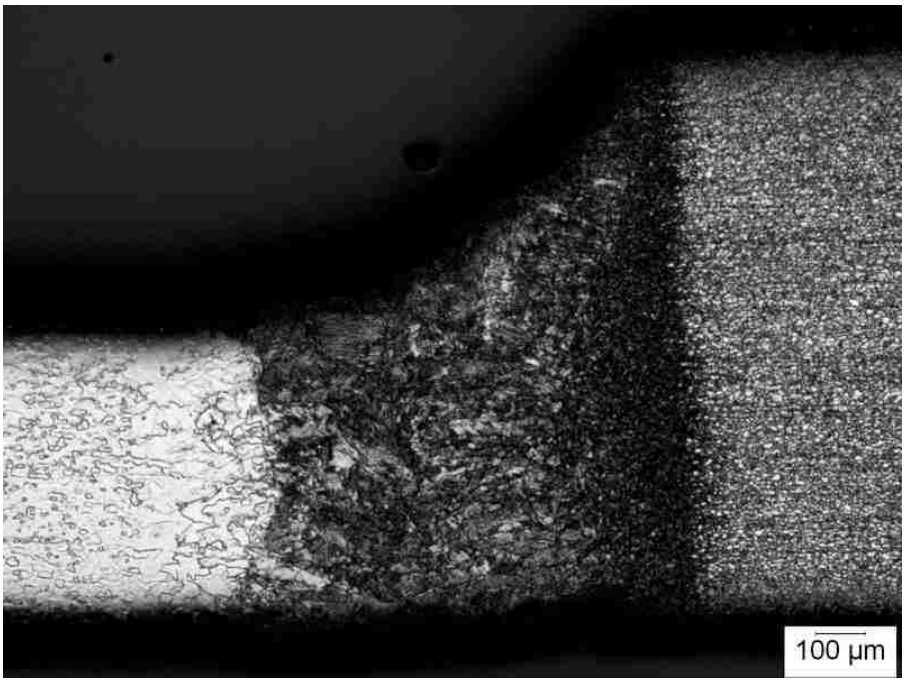

Figure 5.17 Microstructure of laser welding of BDML1

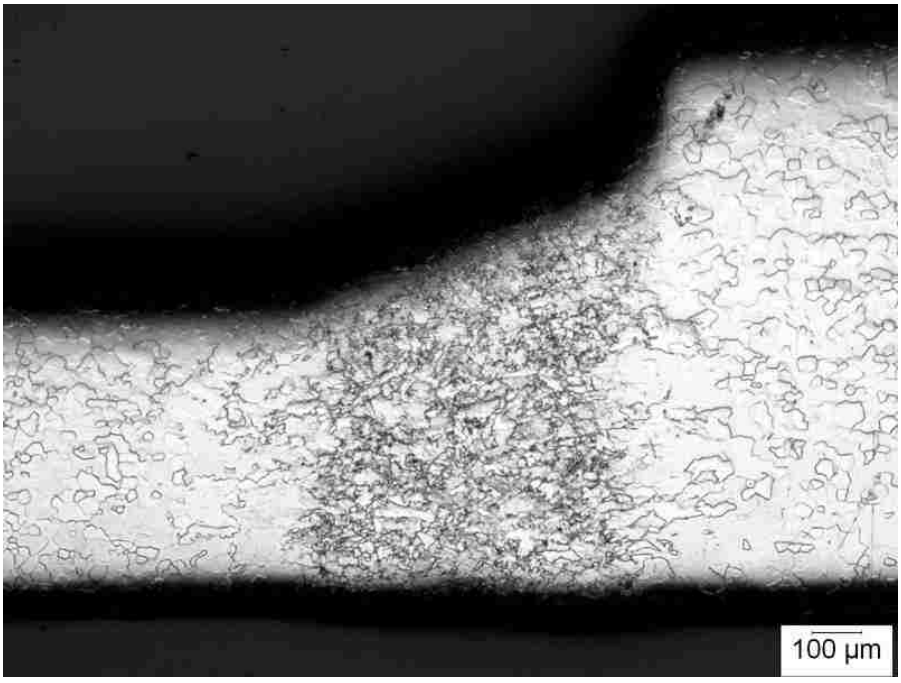

Figure 5.18 Microstructure of laser welding of BSML2

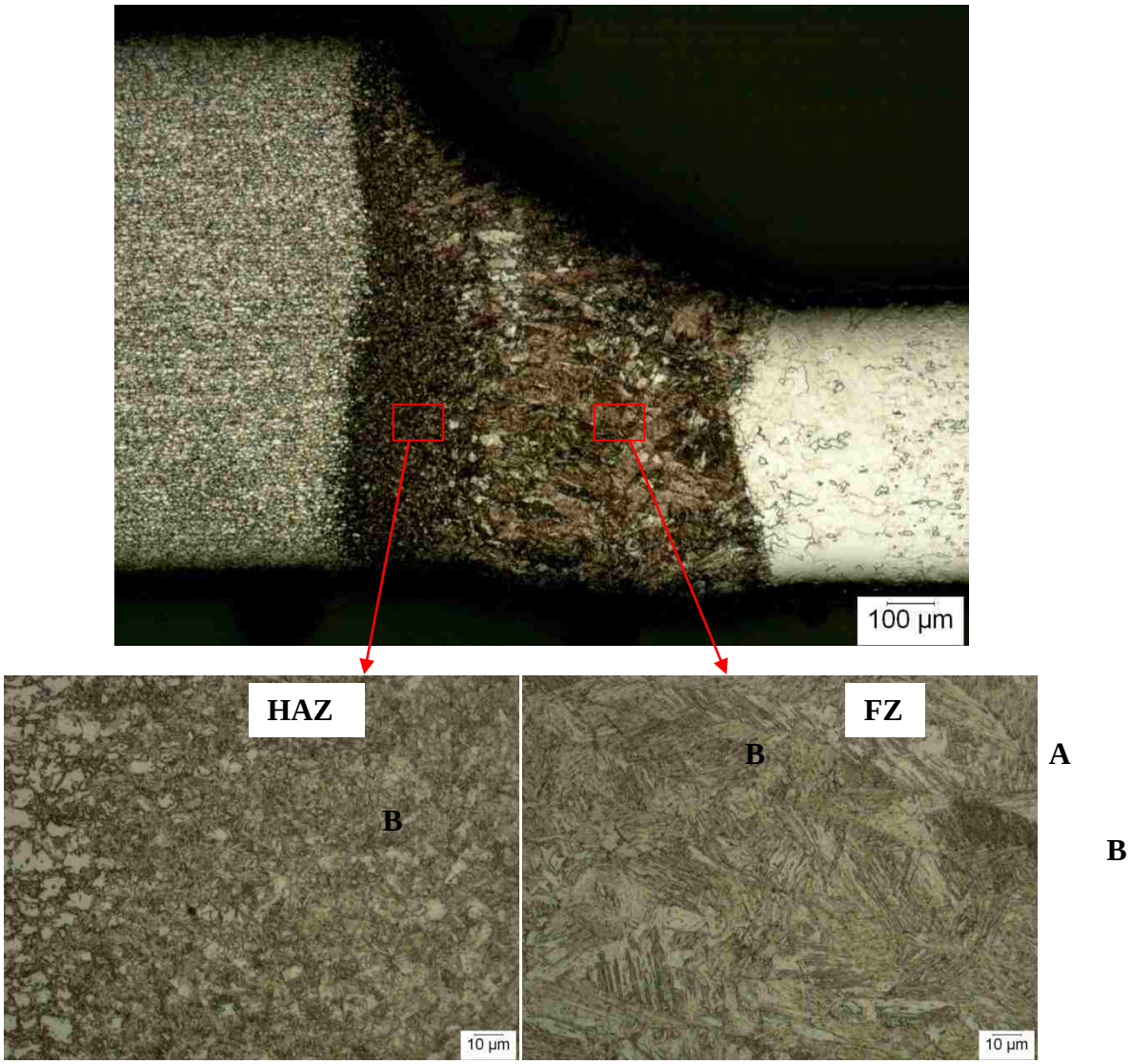

Figure 5.19 Micrographs showing typical weld metal microstructures in weld metal for ADML1: A, Ferrite; B, Martensite.

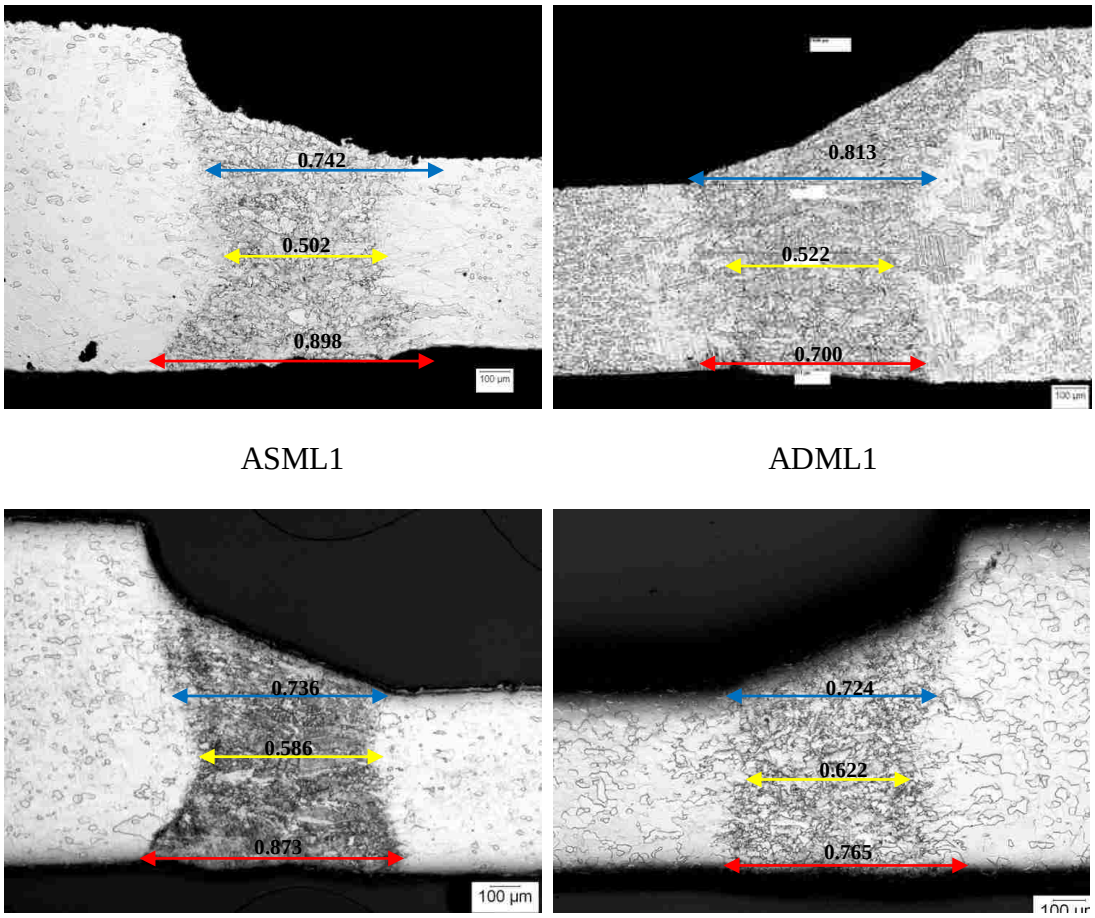

ASML1 ADML1

BSML1 BSML2

Figure 5.20 Weld pool shape measurement

Table 5.2 Weld measurements for experimental samples

Specimen No.	P (W)	Top (mm)	$Core$ (mm)	$Bottom$ (mm)
ASML1	2,858	0.742	0.502	0.898
ADML1	2,858	0.813	0.522	0.700
BSML1	3,000	0.736	0.586	0.873
BSML2	3,000	0.724	0.622	0.765

5.1.4 Hardness Test

Hardness testing was carried out on a Leco Model M-400 microhardness unit using a 100g-200g load. Hardness was measured at the center of the fusion zone and across the heat-affected zone (HAZ) into the base metal (Fig. 5.21).

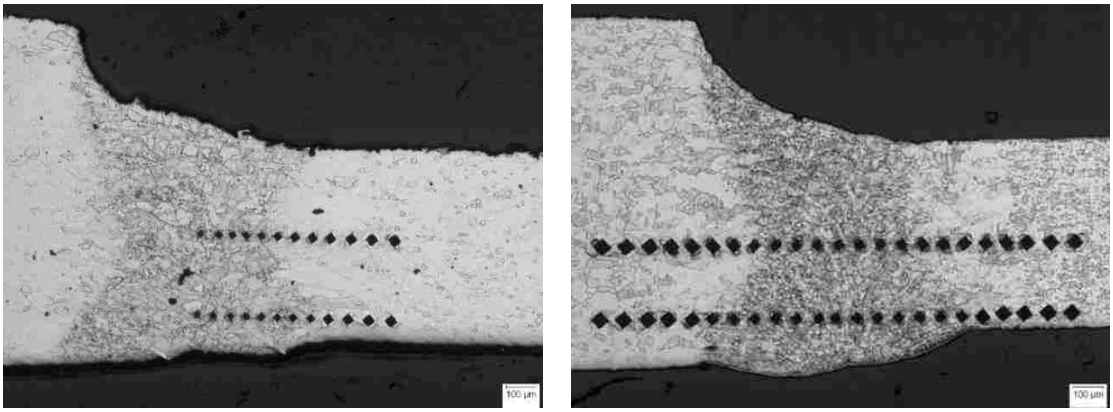

(a) ASML1 (CR/CR) (b) ADML1 (GA/CR)

Figure 5.21 The location of the two hardness scans (center and bottom): a) hardness profiles (HV) of unequal thickness carbon steel sheet using a 100g load. b) hardness profiles of carbon/galvanized steel weld combination using a 200g load.

Fig. 5.22 - 5.23 shows the measured line and the hardness profiles across the weld zone and the heat-affected zone (HAZ) as well as the base metal. The microhardness values are a function of the distance from the weld centerline. It clearly shows the increased hardness in the weld region compared to the base metal. The hardness of the base metal is less than 150 Hv, whereas the maximum hardness of the fusion zone is 184-240 Hv. In the fusion zone, the weld has a higher hardness value than that of the base metal due to the fast cooling that occurs in the bainite structure. Internal stresses also develop due to a combination of thermal stresses and clamping

boundary conditions for the samples in the fixture. The clamp fixtures restrict the sheet metal samples from expanding freely during welding, in addition to preventing out-of-plane distortion during cooling. The increase of hardness is relative to the fusion zone. Since the width of the fusion zone along the bottom line is wider than at the centerline, the range of the maximum hardness along the bottom line is covered more than the centerline. The average weld hardness is approximately 200 Hv, which indicates that the weld zone still has sufficient ductility as also observed in the tensile properties.

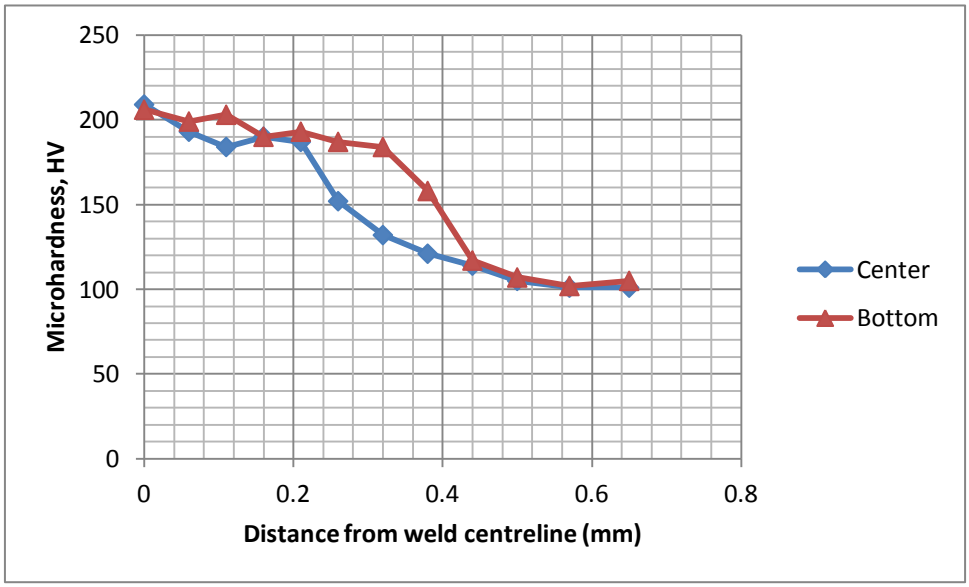

Figure 5.22 Microhardness profile of a welded joint between unequal thickness carbon steel sheet.

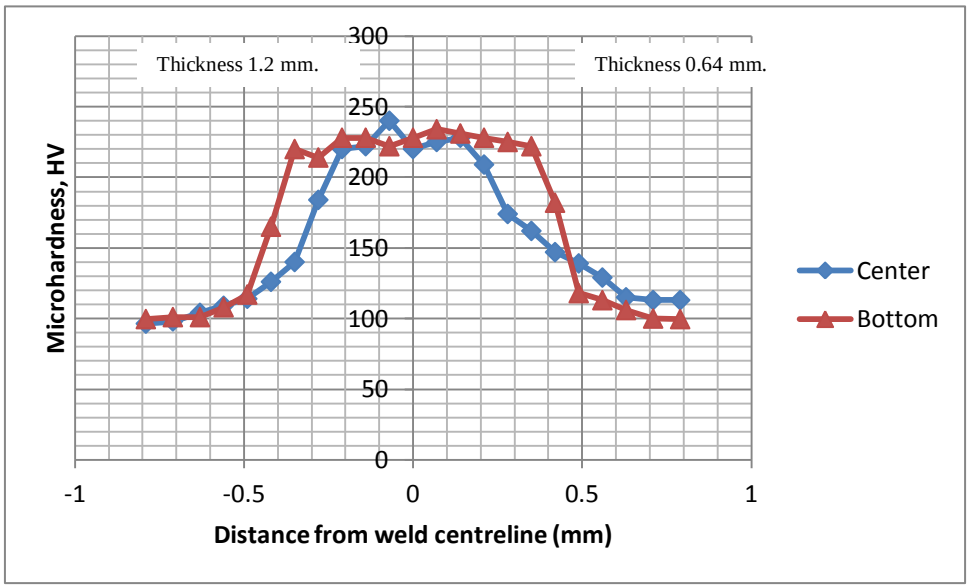

Figure 5.23 Microhardness profile of a welded joint between galvanized steel and carbon steel.

5.2 Laser Welding Simulation Results

Using the geometry, the mesh and the heat flux models described in the previous chapters and the geometrical parameters for the weld pool that were measured from the metallographic investigation, the welding process on butt-joint with different thickness was simulated.

5.2.1 Thermal Results

In this particular study, the thermal results are the basic for weld pool shape comparison between the simulation results and the experimental results. The size and shape of the weld pool from the metallurgical results is used to compare with the thermal results.

Fig. 5.24 shows the temperature distribution when the welding torch passes the center position at the coordinate of y = 25 mm in the welding direction for the power of 2858 W and the welding speed of 8 m/min.

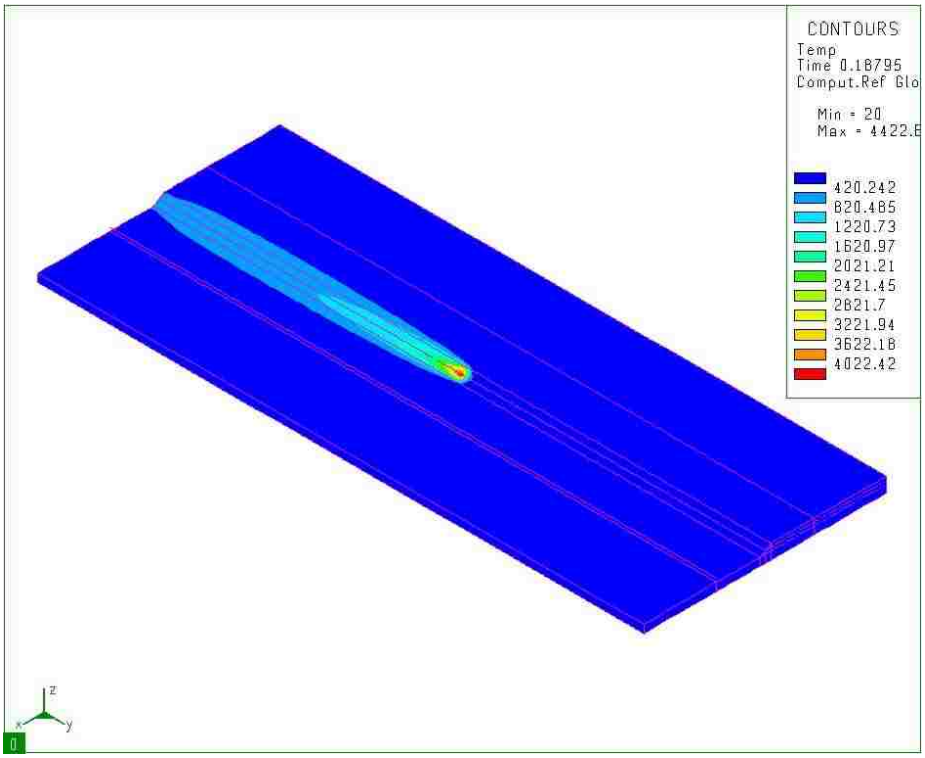

Figure 5.24 Distribution of the surface temperature of the low carbon steel sheet at t = 0.18s.

In Fig. 5.25, the temperature evolution on the top surface along weld line at the starting node, middle node and last node, during the laser welding process are depicted. It can be observed that the heating is very steep, leading to local heating, while the cooling process is relatively fast due to the convection and radiation heat transfer. The process takes about 2s to reach to ambient temperature.

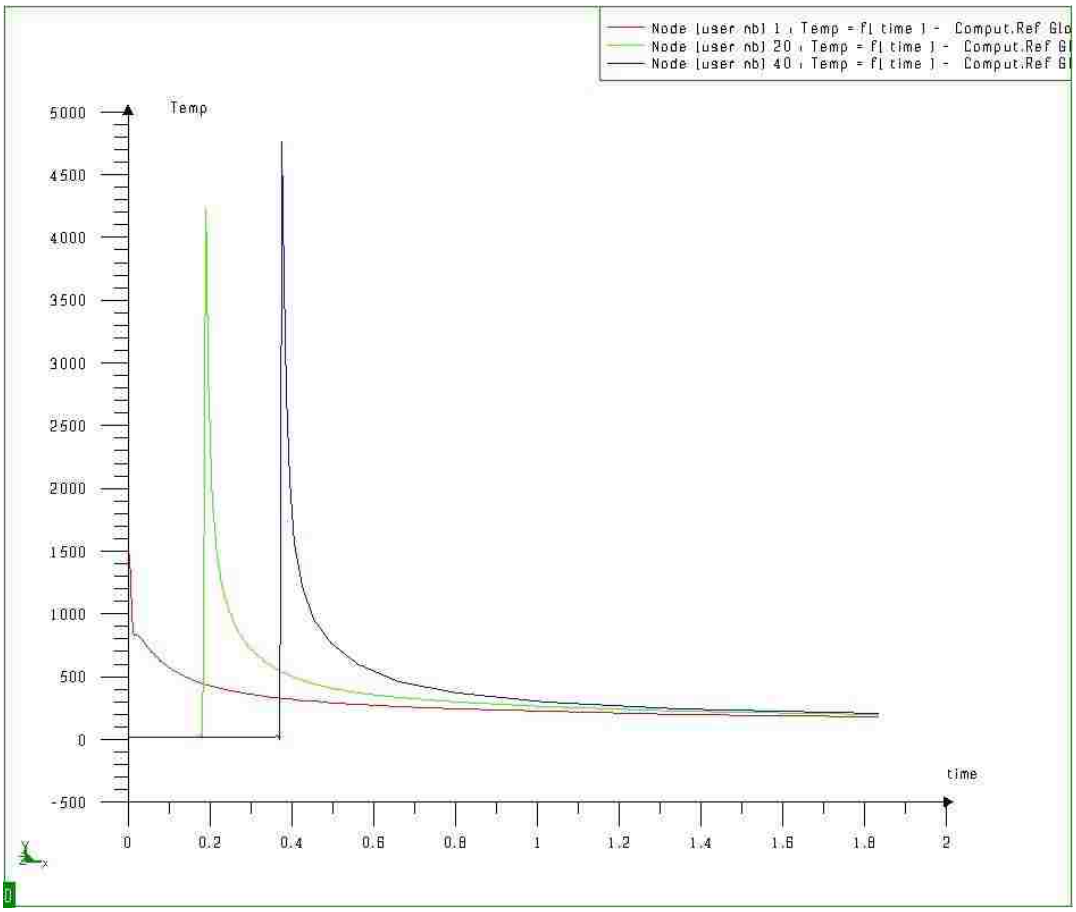

Figure 5. 25 Temperature evolution on the top surface at start node, middle node and last node.

The temperature distribution in the cross-section perpendicular to the welding direction is presented in Fig 5.26. The molten zone is sized to emulate the molten zone produced by the actual laser welding process. The red area represents the melted material in the weld pool with a temperature higher than 1505 ^{o}C (melting point). The very high temperature gradients in the vicinity of the weld line close to the upper surface of the molten zone may be clearly observed. The welding pool shape on the top and bottom surface is wider than that on the middle planes.

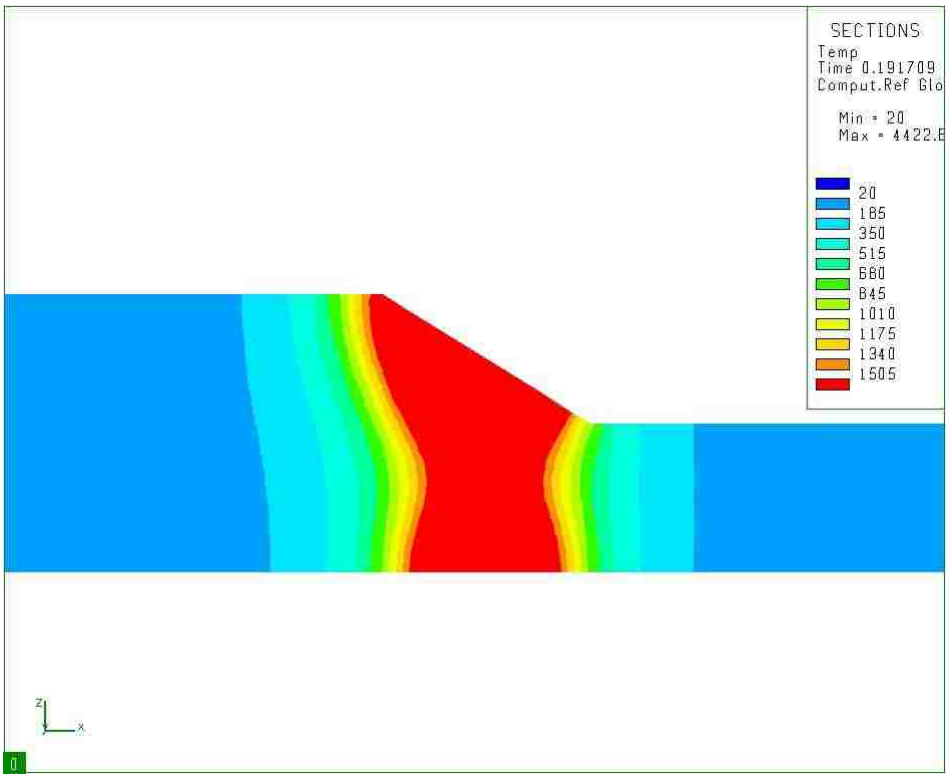

Figure 5.26 The temperature distribution in the cross-section perpendicular to the welding direction.

Transient temperature distributions develop during the laser beam pass at the mid section of the workpiece as shown in Fig. 5.27. The size of the molten zone, or weld pool shape behind the laser source increases after passing of the laser source. At this time the keyhole shape and size are considered fixed. After that the molten pool size decreased during cooling process and solidification. Fig. 5.28 compares the experimental and simulated weld pool shape for ASML1, BSML1, and BDML1. The comparison of the weld pool shape indicates that the simulated weld pool shape is close to the measured experimental weld pool shape. Therefore, the simulated weld pool shapes verify the correct implementation of the heat source model. Similarly, the overall

simulated thermal fields seem to be reasonable enough to proceed further with the mechanical analysis.

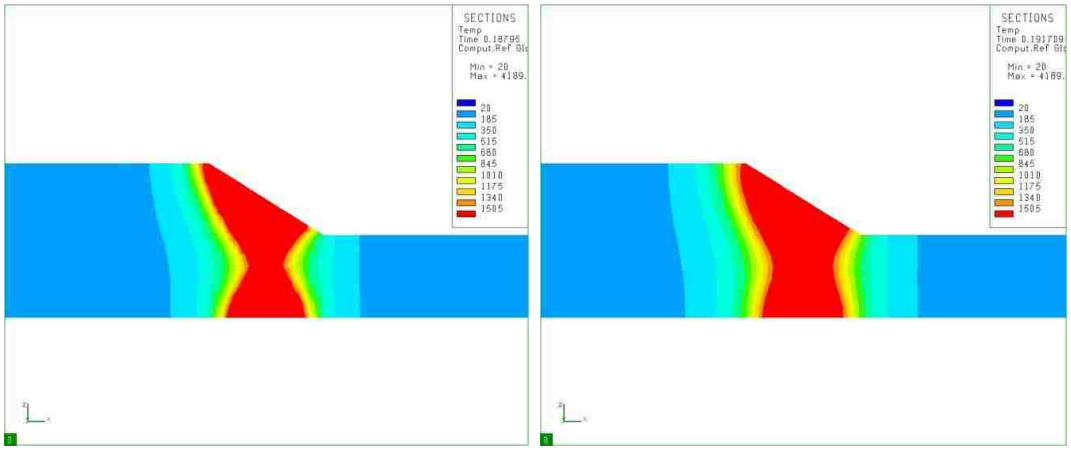

(a) (b)

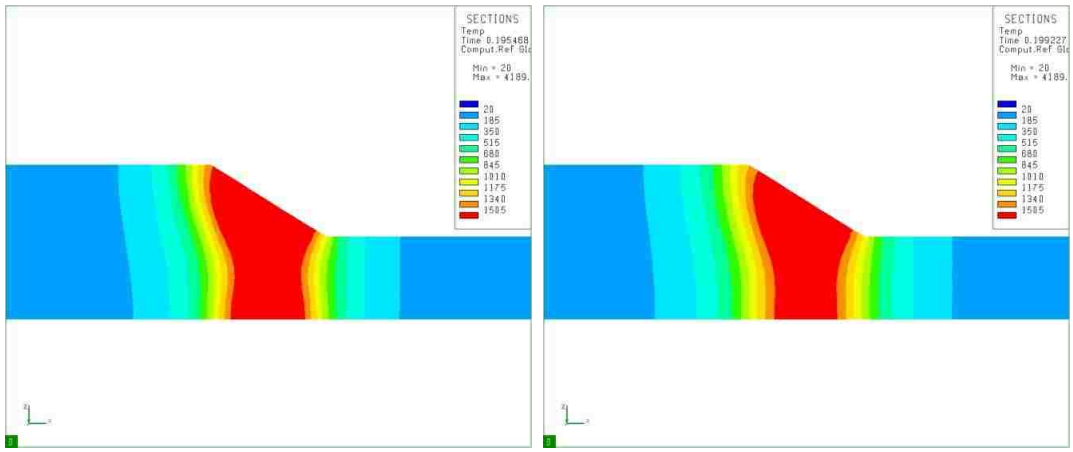

(c) (d)

Figure 5.27 Transient temperature distribution at mid section of the workpiece during welding process, at (a) t ~ 0.188s, (b) t ~ 0.192s, (c) t ~ 0.195s and (d) t ~ 0.199s

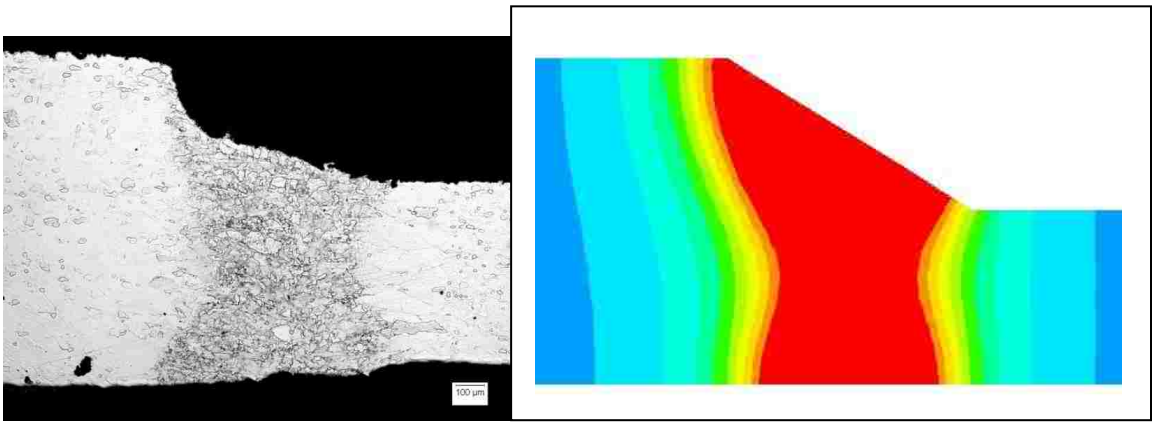

(a) ASML1

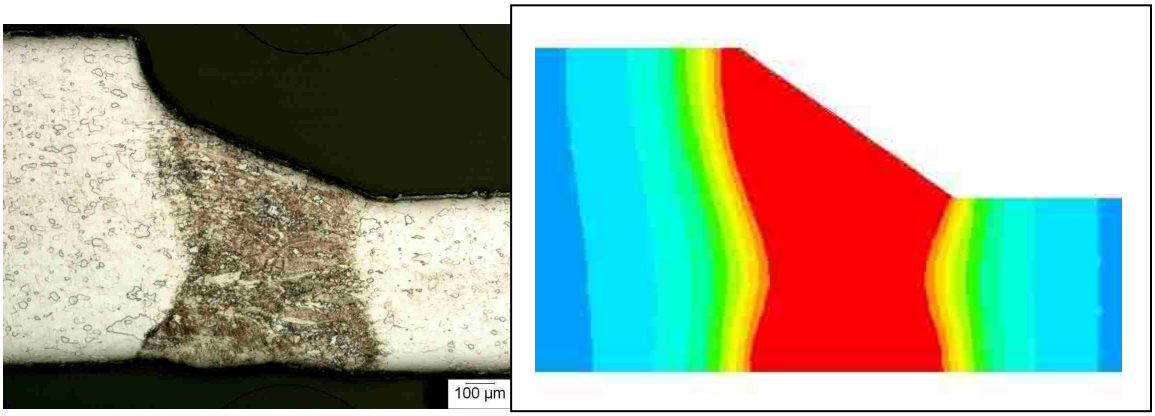

(b) BSML1

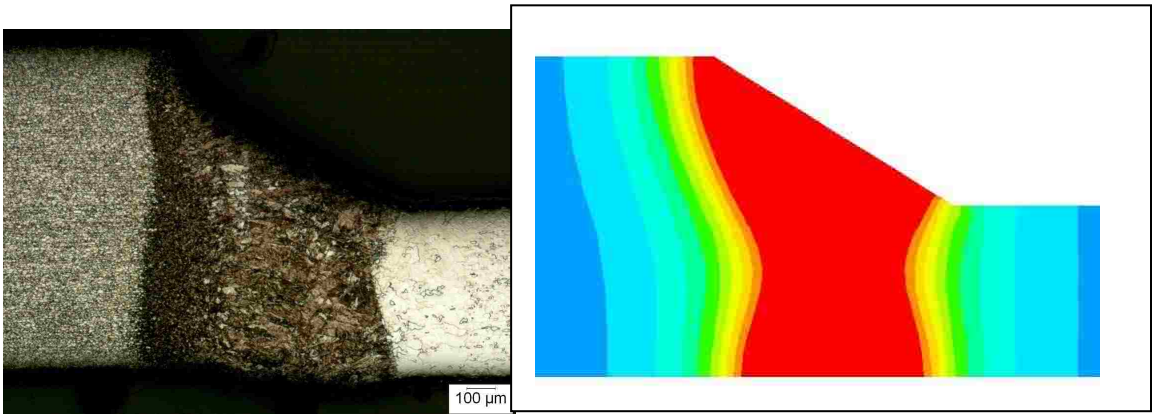

(c) BDML1

Figure 5.28 Comparison of weld pool shape: (a) ASML1, (b) BSML1, and (c) BDML1

5.2.1.1 Effect of welding speed

In order to study the influence of the welding speed on the weld pool shape, three trial tests were conducted where the welding speed was varied in the range of 7 - 9 m/min in increasing of 1 m/min with the laser power constant at 2,858 W. The effect of the welding speed on the weld pool shape at the middle of the joint is illustrated in Fig. 5.29 - 5.31. It is observed that the width of the weld pool size decreases with increases in the welding speed. In addition, the peak temperature decreases for higher welding speeds, from 4,138 to 3,855 ^{o}C as the welding speed changes from 7 to 9 m/min.

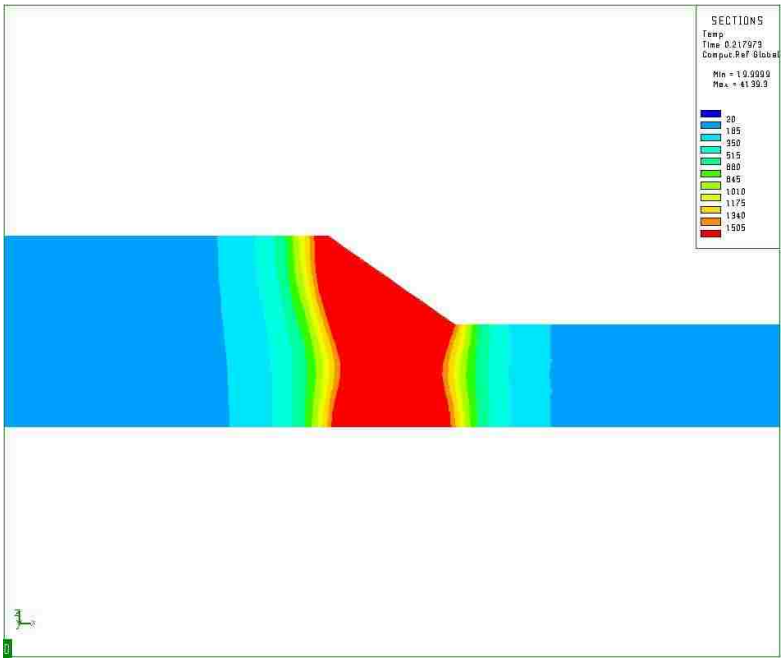

Figure 5.29 Temperature distribution at mid section of the workpiece for welding speed of 7 m/min

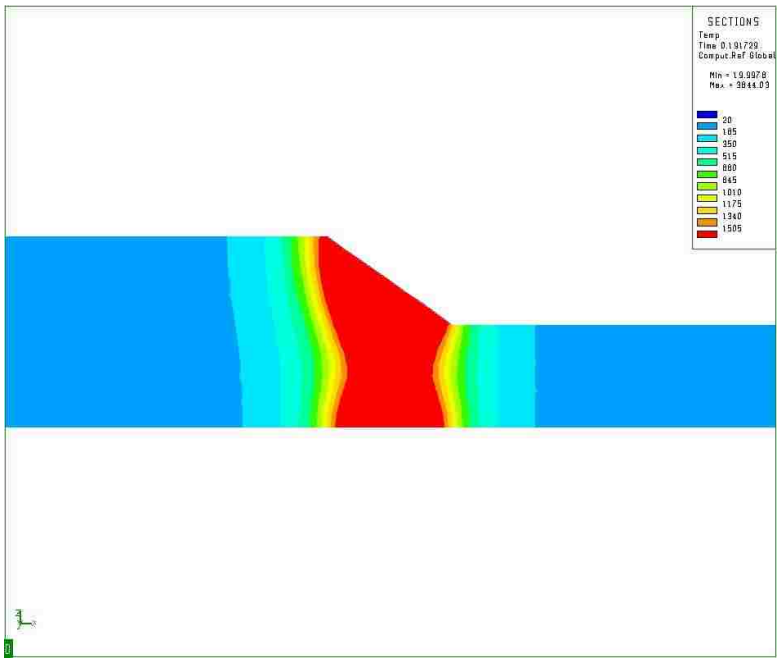

Figure 5. 30 Temperature distribution at mid section of the workpiece for welding speed of 8 m/min

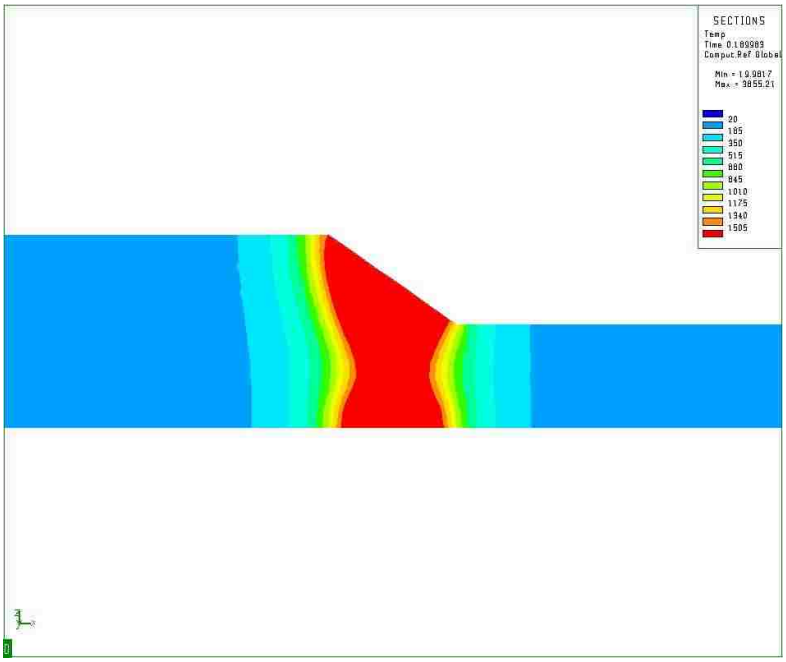

Figure 5. 31 Temperature distribution at mid section of the workpiece for welding speed of 9 m/min

5.2.1.2 Effect of laser power

In this study the laser power used was between 2,858 W and 3,000 W, with a constant welding speed of 8 m/min. The effect of the laser power on the weld pool shape at the middle of the joint is illustrated in Fig. 5.32 - 5.34. It is observed that the width of the weld pool size increases with increasing the laser power. In addition, the peak temperature increases for higher laser power from 3,842 to 4,023 ^{o}C, as the laser power changes from 2,858 to 3,000 W.

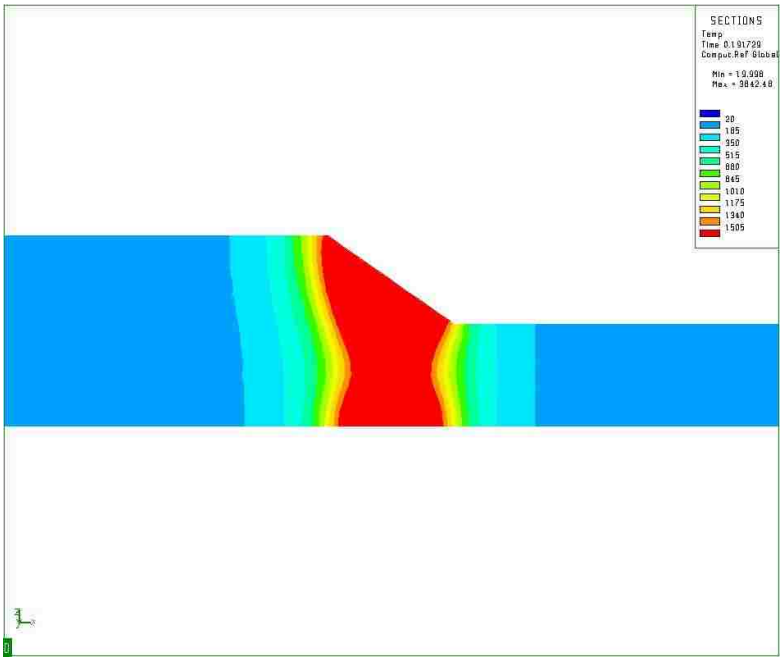

Figure 5. 32 Temperature distribution at mid section of the workpiece for laser power of 2,700 W

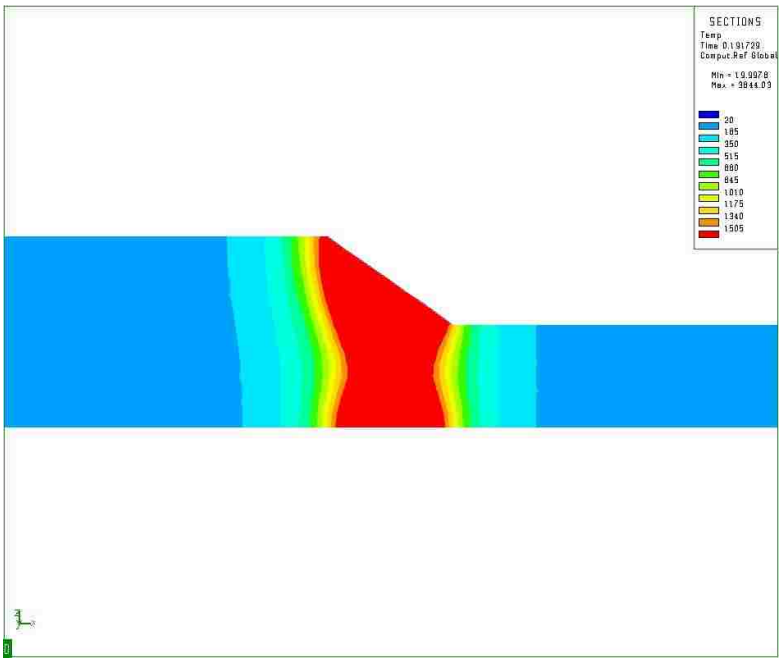

Figure 5.33 Temperature distribution at mid section of the workpiece for laser power of 2,858 W

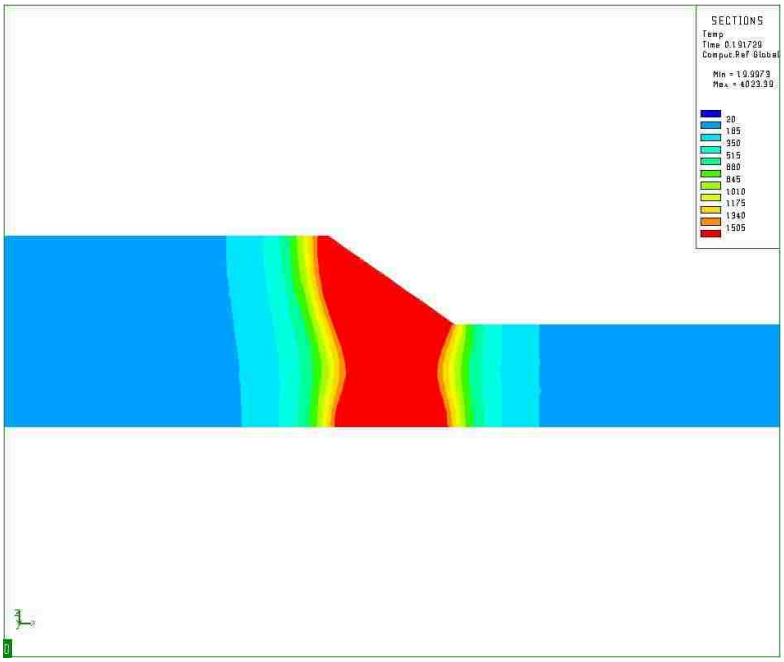

Figure 5.34 Temperature distribution at mid section of the workpiece for laser power of 3,000 W

5.2.2 Mechanical Results

Welding induced residual stresses and distortion are among the most studied subjects for welded structures. A structural analysis was performed to calculate the distortion and residual stress induced during welding, for appropriate boundary conditions, using SYSWELD. The basis of stress and distortion analysis is the temperature field during welding. The thermal results were used to calculate mechanical results in both distortion and stress.

5.2.2.1 Distortion Analysis

Distortion simulations of all experimental configurations were performed. The simulation of the butt joint was completed in two steps. First, the laser weld torch moved from t=0 to t=5s with clamping, where the weld torch was stepped forward from start to end of the weld line. Second, the clamping was released and cooling. This step consisted of a transient analysis from t=5s to the final time of t=500s. The results giving the displacements after cooling and unclamping for different welding speeds and laser power are shown in Figs. 5.35 - 5.37. The contours in these figures represent the z-direction displacement.

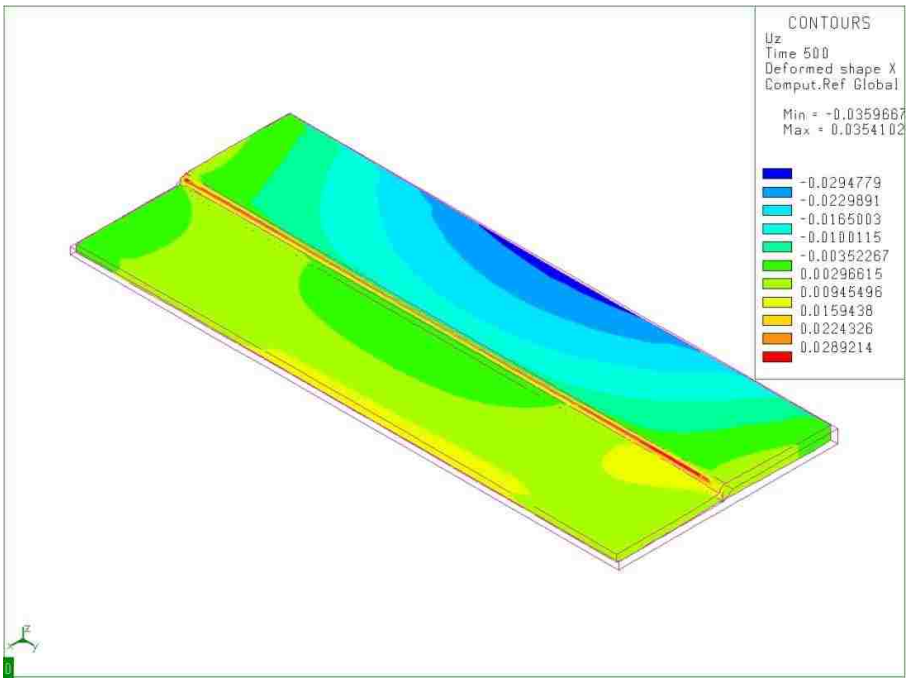

Figure 5.35 Distortion for welding speed 7 m/min.

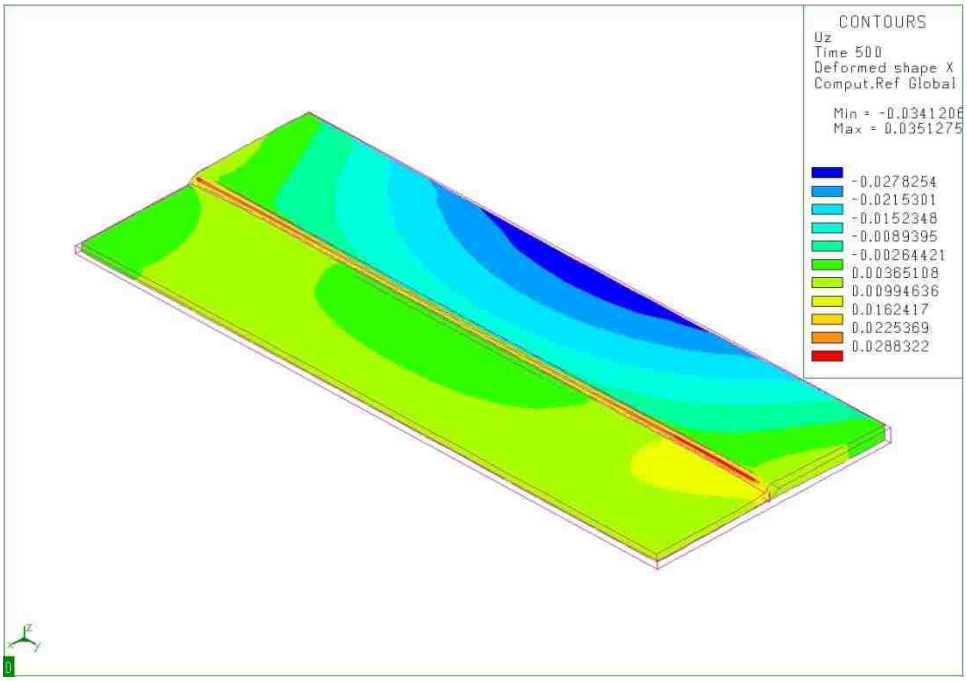

Figure 5.36 Distortion for welding speed 8 m/min.

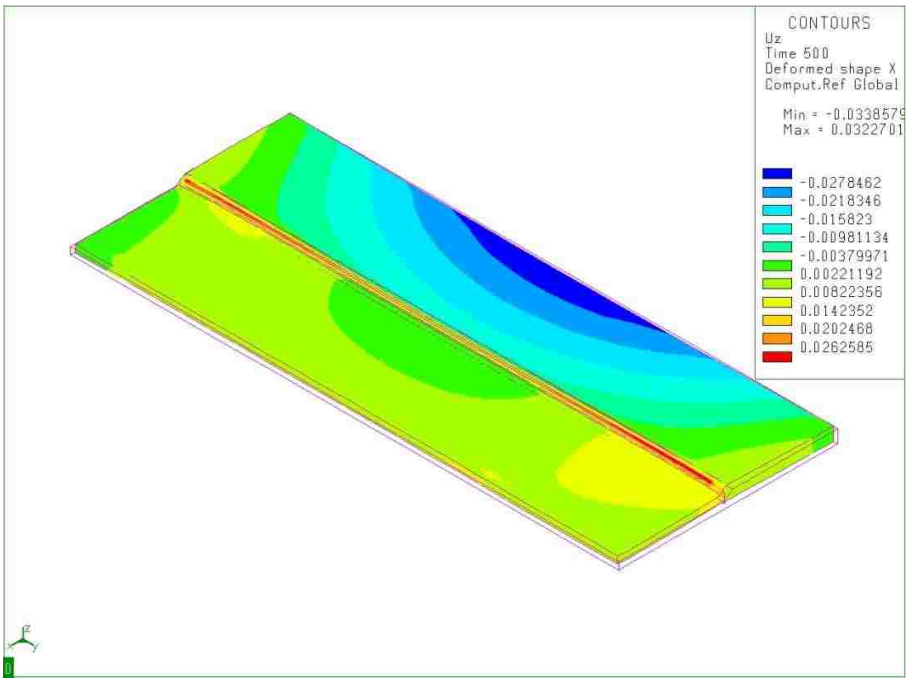

Figure 5.37 Distortion for welding speed 9 m/min.

The effect of laser power with constant welding speed of 8 m/min on the distortion of a laser welded joint is shown in Figs. 5.38 - 5.40. The higher magnitude for the displacement profile at the end of welding is shown in Fig. 5.41. The displacements are magnified 5 times in these figures to make them clearly visible. From all the figures, both longitudinal bending and transverse bending are generated in the butt welded joint.

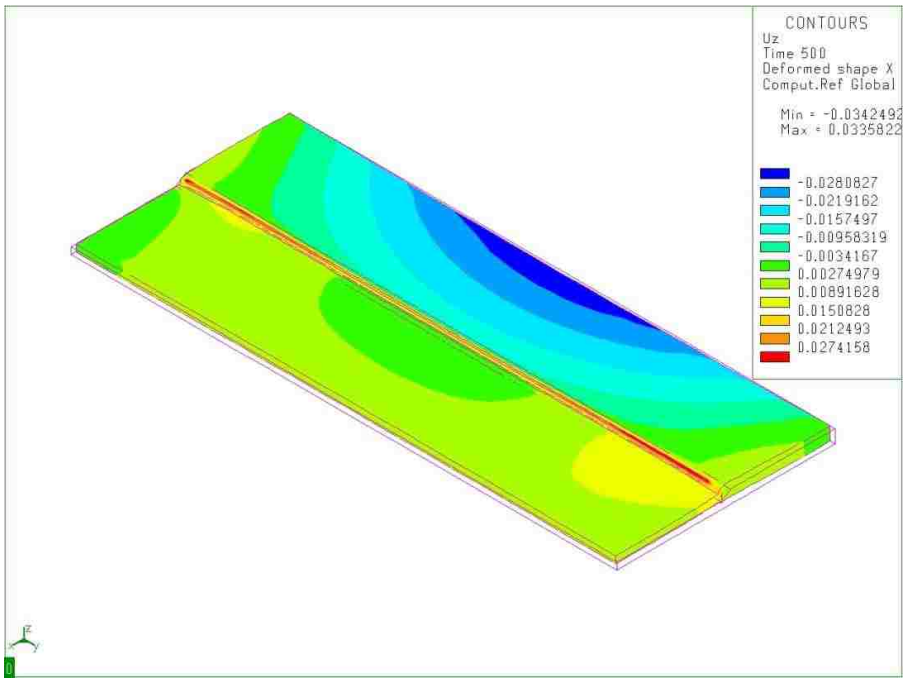

Figure 5.38 Distortion for laser power of 2,700 W

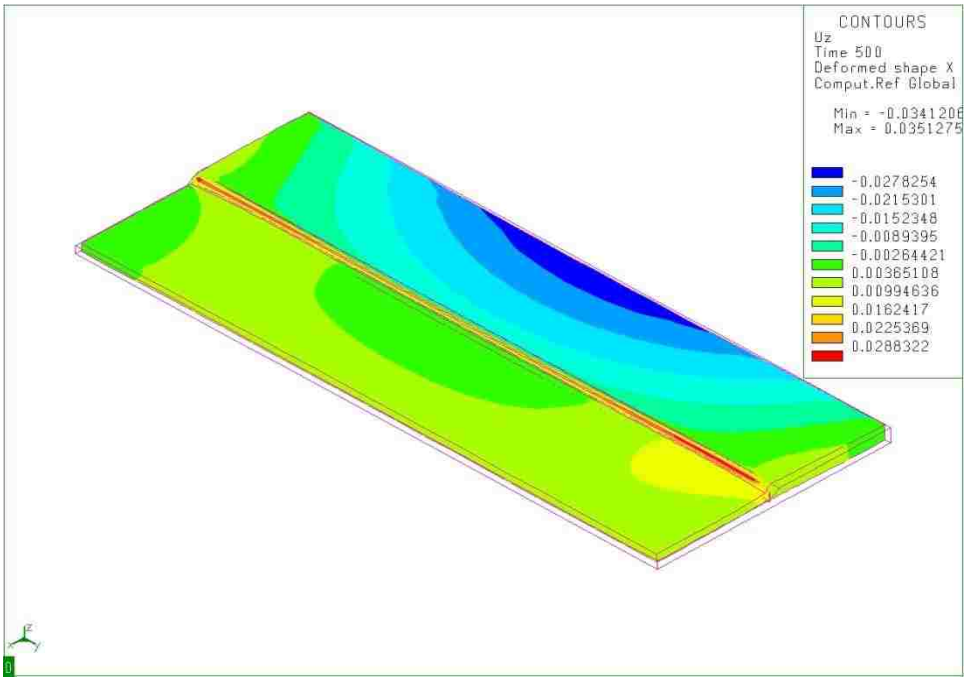

Figure 5.39 Distortion for laser power of 2,858 W

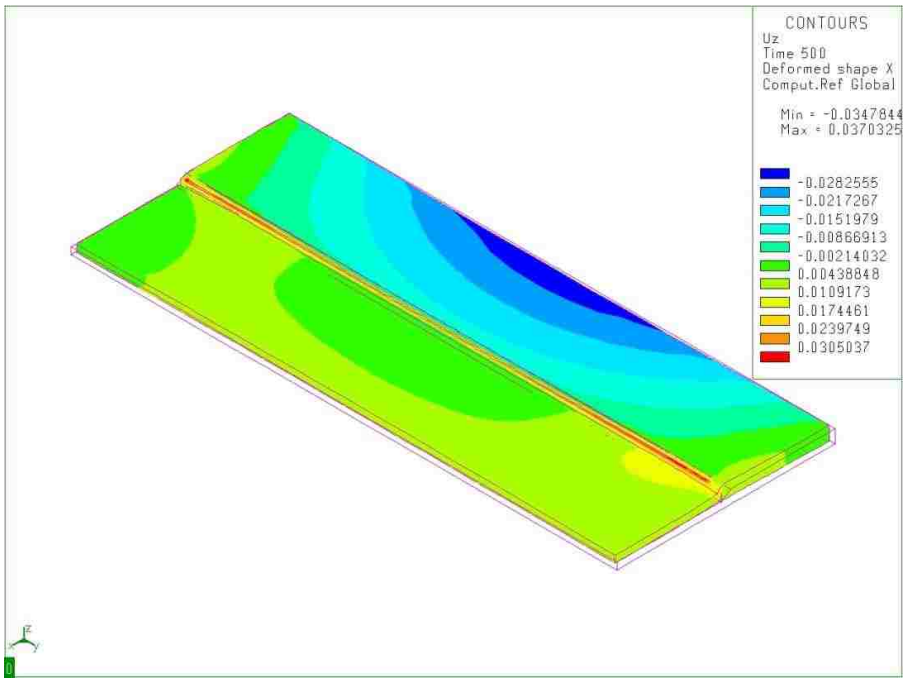

Figure 5.40 Distortion for laser power of 3,000 W

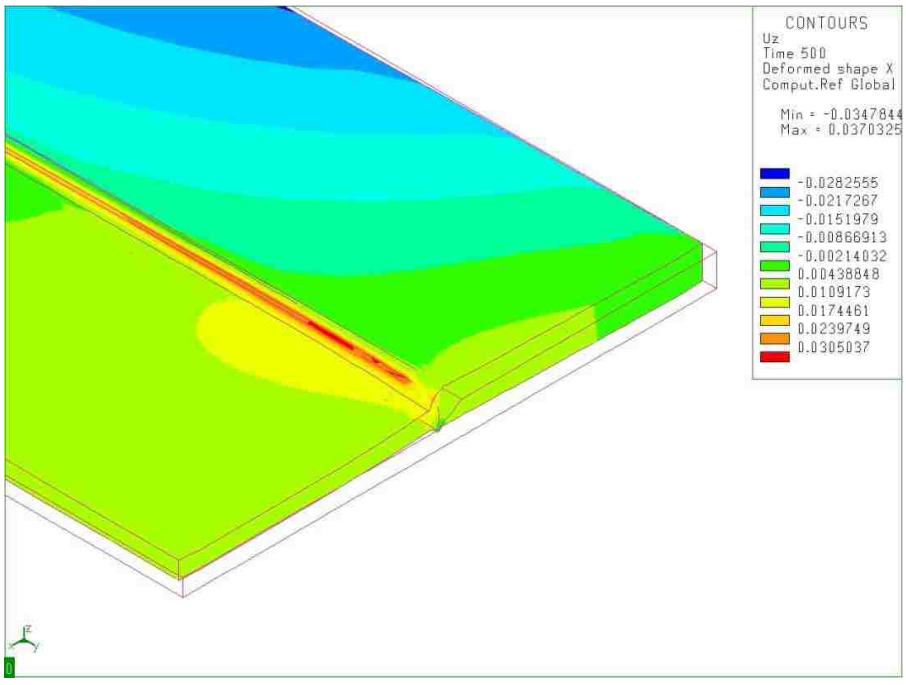

Figure 5.41 Higher magnification for deformation of thin sheet for laser power of 3,000 W.

Some of the distortion results for the cross section near the end point are shown in Fig.5.42. This figure displays the whole distortion of the butt joint. Greater distortions occur in the thinner sheets. The deflection of the thinner sheet is greater than the thicker sheet, due to the lower bending stiffness of the thin sheet metal. The distorted shape was compared between experiment and simulation at the middle point of the model as shown in Fig. 5.43. Comparison between the finite element predictions and the average measured distortions for the ASML1 case are shown in Fig. 5.44. Due to the different thicknesses of the specimens, the displacement values are given on both sides of the joint. It is observed that the maximum displacement occurs towards the center plane of the sheets. In addition, the displacement values of the thin metal sheet are higher than that of the thick metal sheet. It is clear that the model can accurately predict the distortions of the welded parts. Even though the distortions evaluated using the model are very close to the experimental measurements. Another factor, the shipping of the samples from the company that performed the welding to Lehigh University might have altered the real distortion. Fig. 5.45 shows the effect of the welding speed on several of angular distortions. Higher welding speeds cause a reduction in the angular distortion. Fig. 5.46 shows the effect of the laser power on several angular distortions. Higher laser power causes an increase in the angular distortion, as a result of a larger amount of heat energy input delivered into the sheet during the welding process.

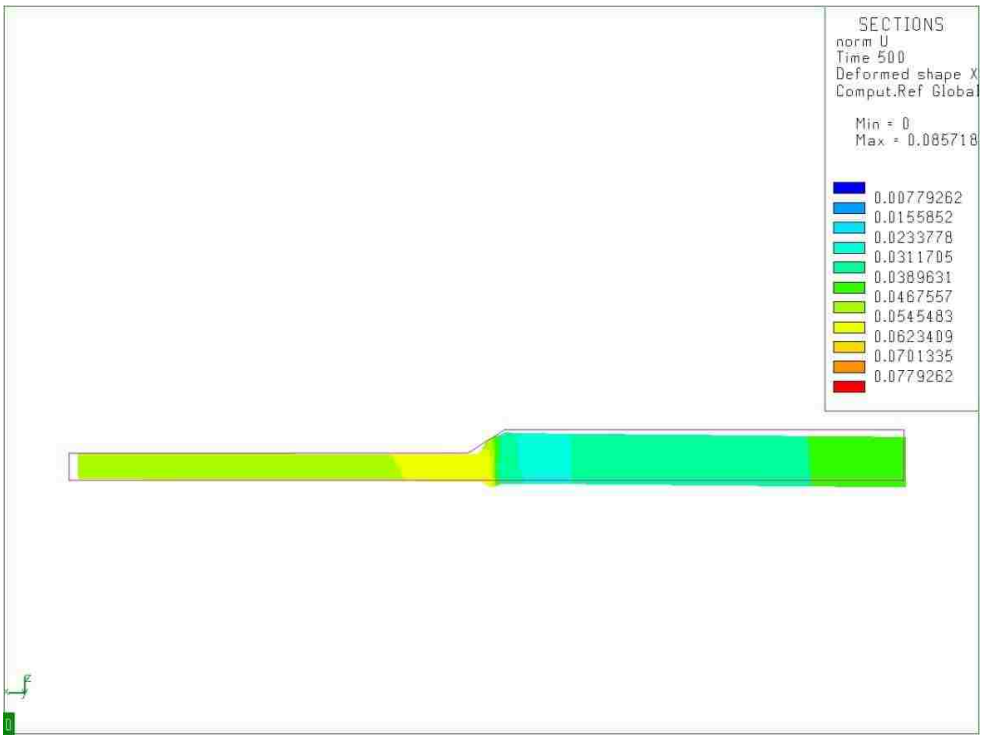

Figure 5.42 The cross section distortion at the middle point for ASML1 simulation

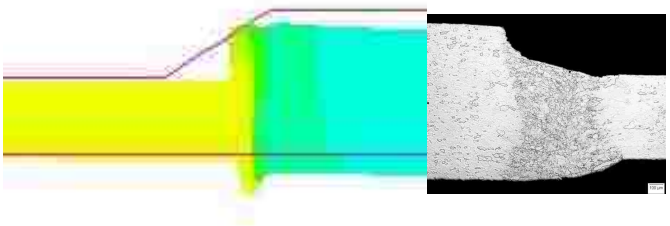

Figure 5.43 Comparison of distortion shape between experiment and simulation

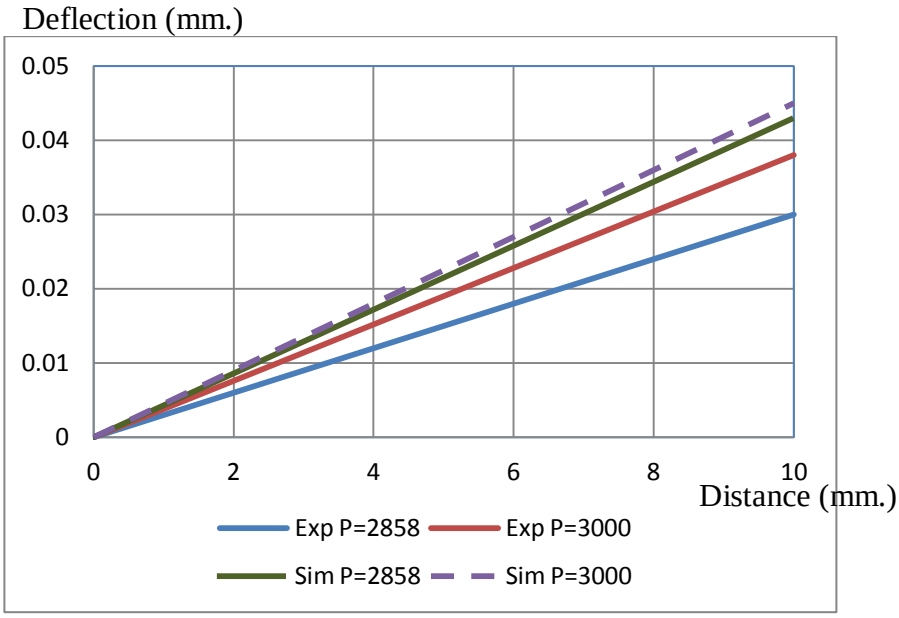

Figure 5.44 Comparison of distortion between simulation and experiment results for ASML1

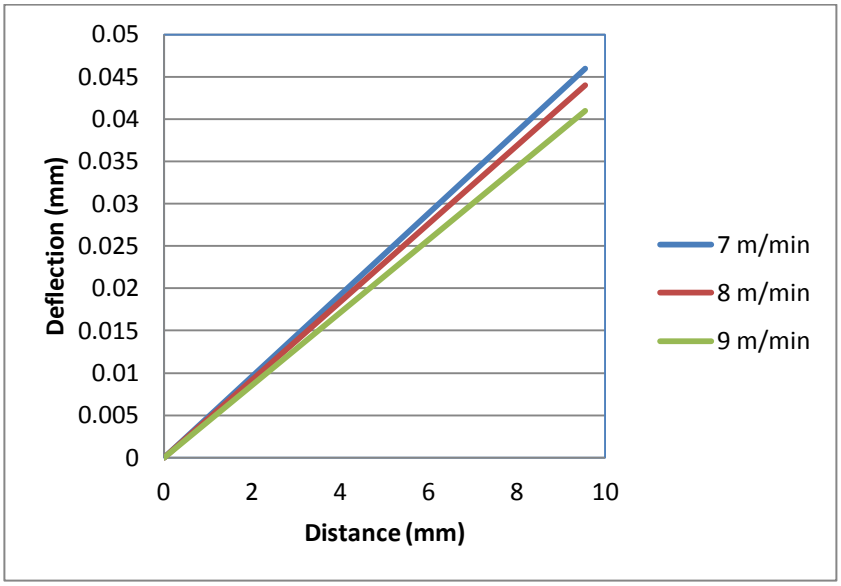

Figure 5.45 Angular distortion under various welding speed

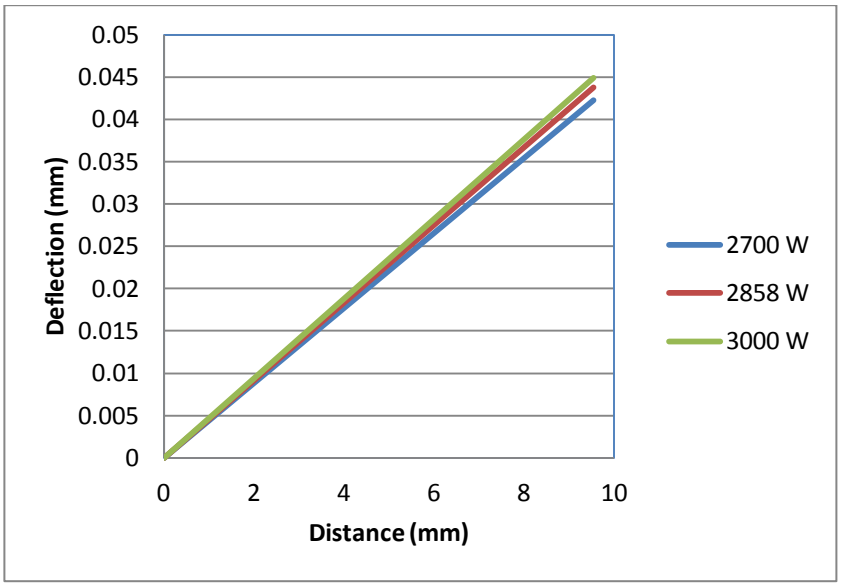

Figure 5.46 Angular distortion under various laser power

5.2.2.2 Stress Analysis

As welding involves localized heating of the sheet, it induces highly non-homogeneous stresses during its application. The stresses created in the weld during the welding process are due to the expansion of material that occurs during the heating of the welded metal sheet. This is followed by non-uniform contraction during cooling. Furthermore, the mechanical constraint of the metal sheet by the clamp fixture will cause additional stress. Having obtained good agreement between experimental and simulated temperatures and displacement results, residual stresses can now be predicted. The distribution of transverse (sigma11) and longitudinal (sigma22) residual stresses on the surface after cooling and unclamping for different welding speeds and laser power are shown in Fig. 5.47. The distribution of the von Mises stress in several cross sections after cooling at 500s is shown in Fig. 5.48. The stresses are given in MPa in this figure.

Predicted residual stresses at the mid-length of the weld for different condition are shown in Fig. 5.49 - 5.53. Since there are unequal sheet thicknesses, the expansion of the thinner sheet is higher than the thicker sheet due to greater accumulated heat. When the thinner sheet expands, the thicker sheet tries to maintain its original shape. Therefore, the tension stress occurs at the thinner sheet while the compressive stress occurs at the thicker sheet. For the expansion of both thicknesses along the y-axis, the metal sheet can expand in both the positive y-axis (ending edge) and negative (starting edge). The tensile stress distributes along the middle welding section along the y-axis, but reduces to compressive stress at the free surfaces of the starting and ending edges of the weld line. The material in the weld experiences significant longitudinal tensile stresses because when the weld contracts during cooling, the clamping of the base sheet to the weld to maintain the original length causes the weld to be plastically deformed. The longitudinal stress of 456 MPa in the weld is much higher than the transverse stress of 140 MPa for welding speed of 8 m/min.

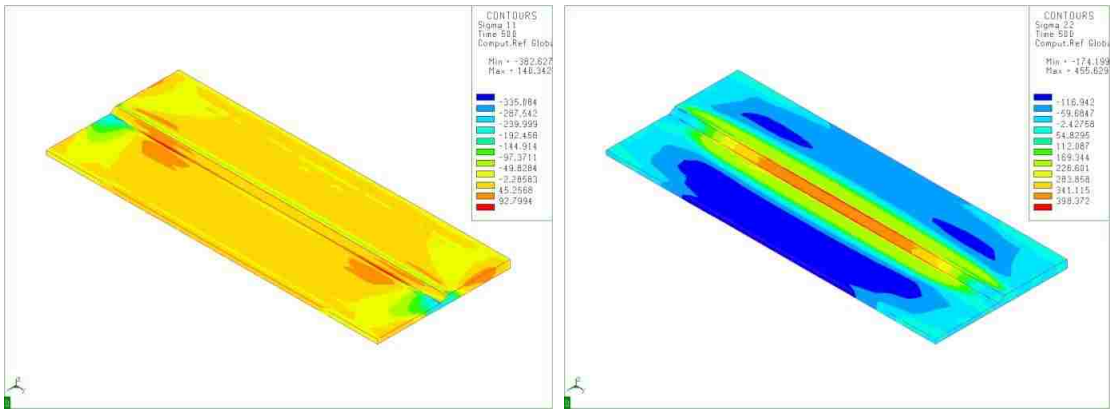

a) Transverse stress b) Longitudinal stress

Figure 5.47 The distribution of transverse and longitudinal residual stresses on the surface

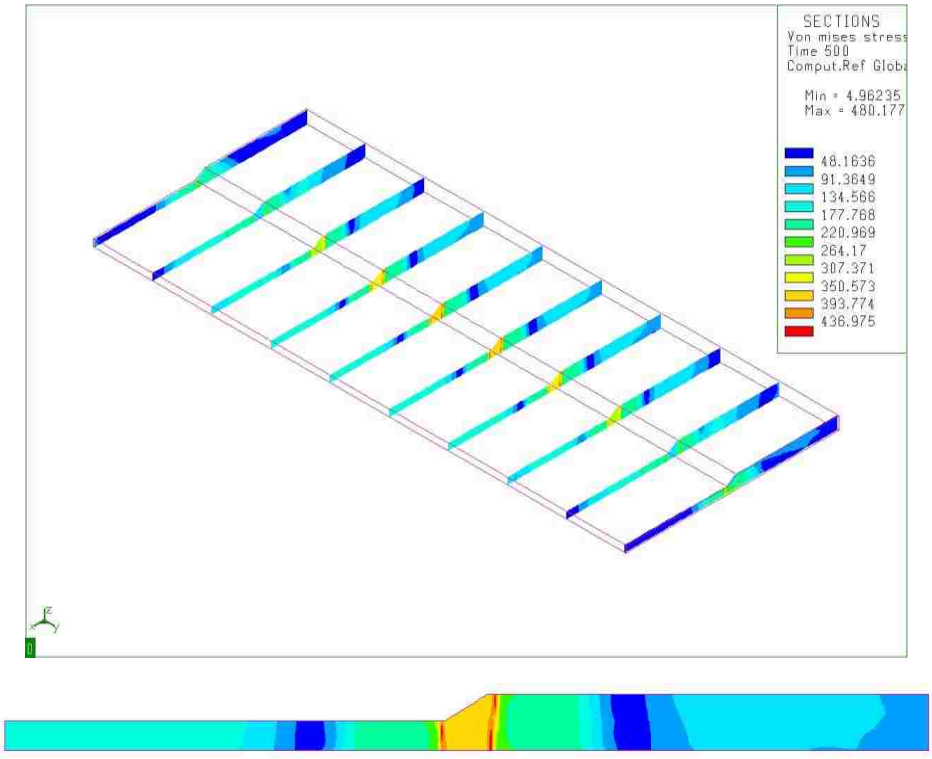

Figure 5.48 Distribution of the von Mises stress in several cross sections

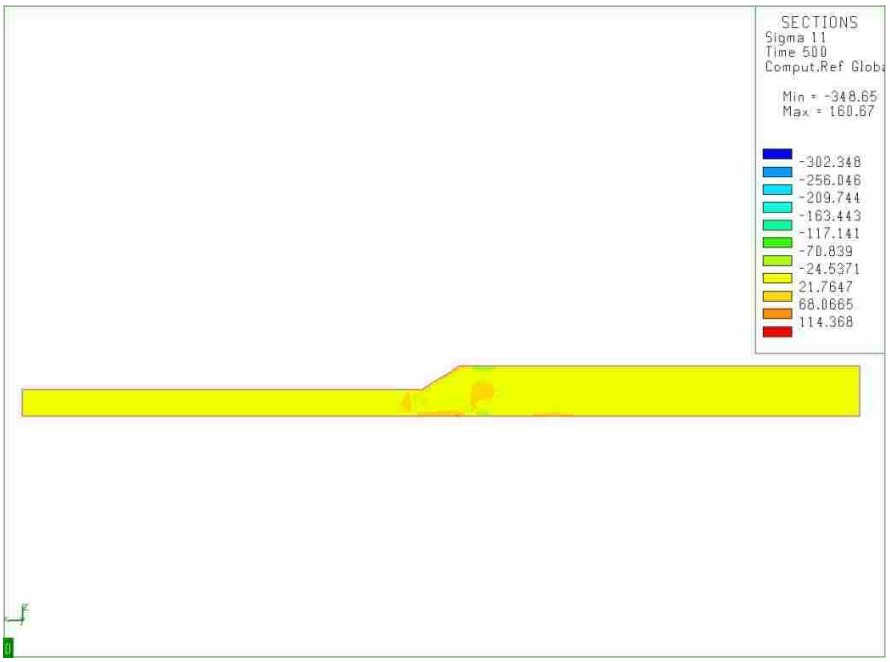

(a) Transverse residual stress

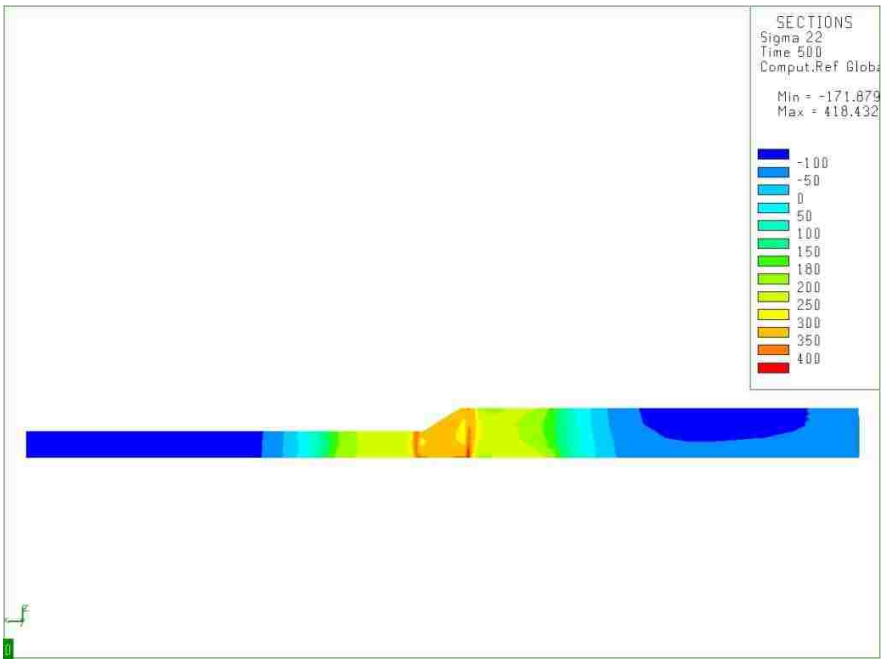

(b) Longitudinal residual stress

Figure 5.49 Predicted stress at mid-length of weld for welding speed of 7 m/min

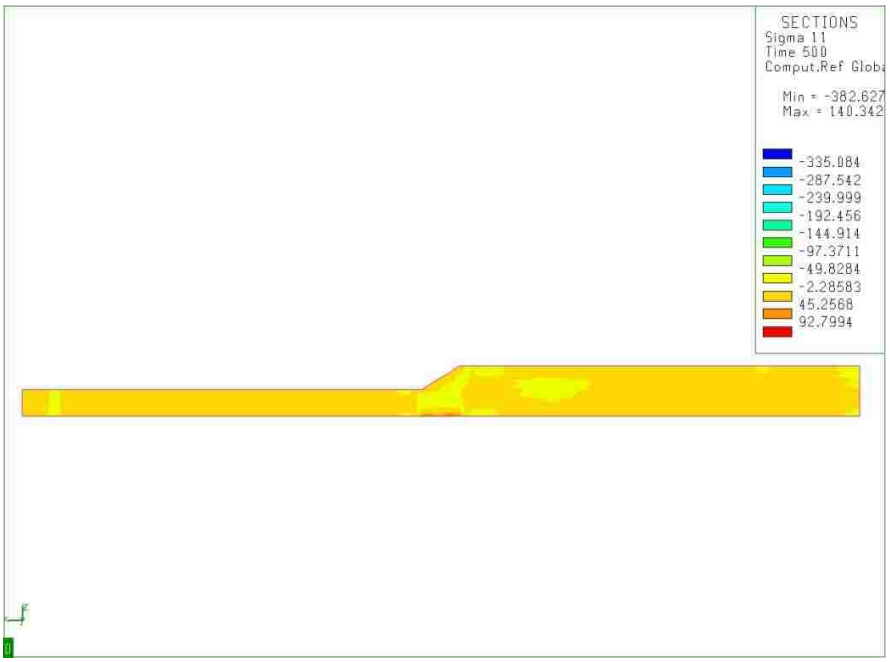

(a) Transverse residual stress

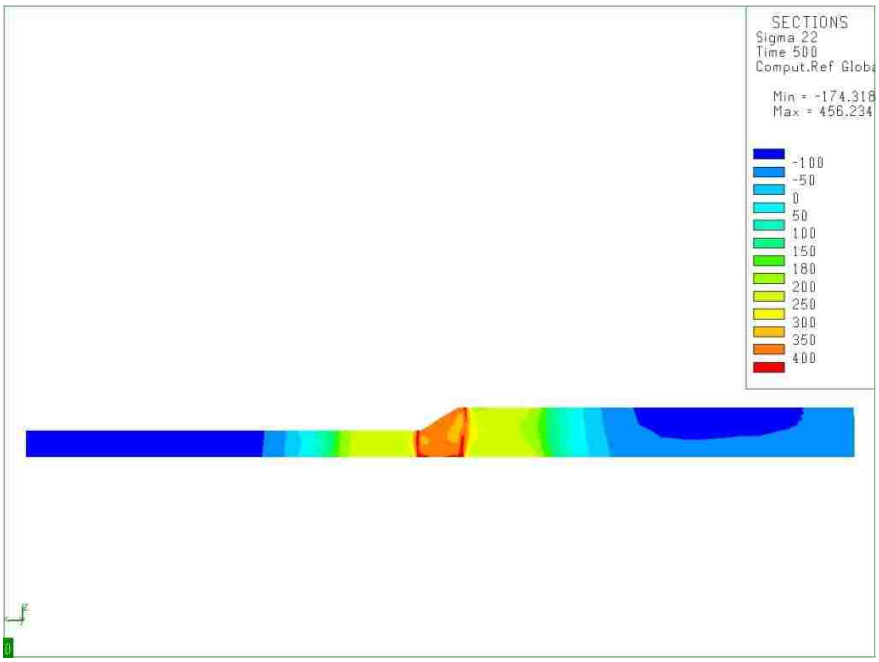

(b) Longitudinal residual stress

Figure 5.50 Predicted stress at mid-length of weld for welding speed of 8 m/min.

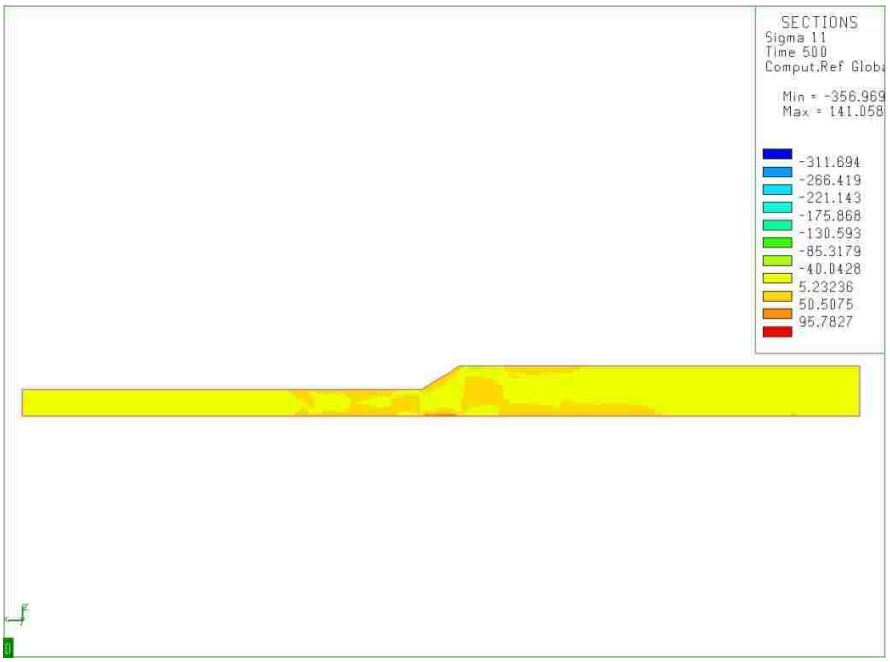

(a) Transverse residual stress

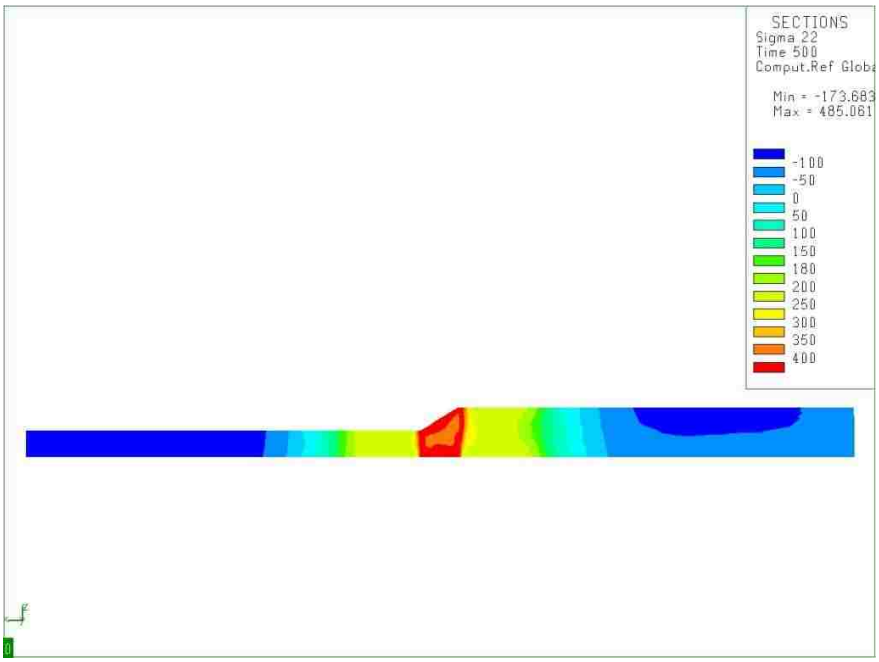

(b) Longitudinal residual stress

Figure 5.51 Predicted stress at mid-length of weld for welding speed of 9 m/min.

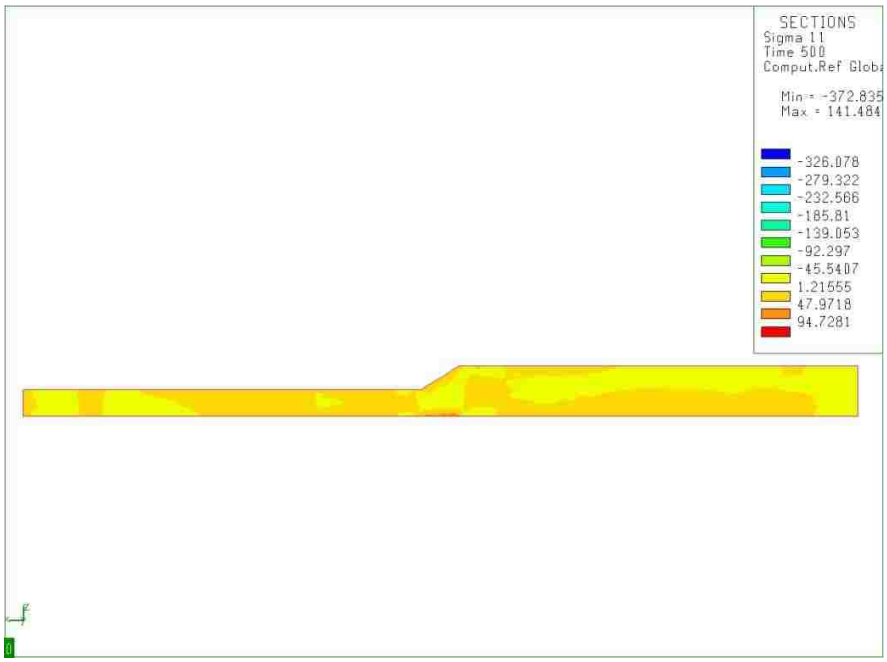

(a) Transverse residual stress

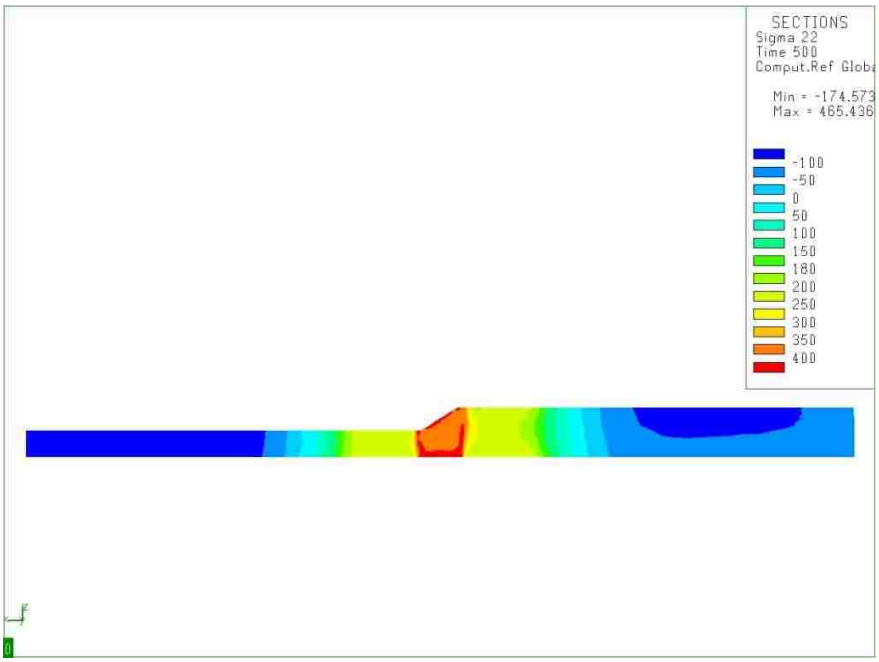

(b) Longitudinal residual stress

Figure 5.52 Predicted stress at mid-length of weld for Laser power of 2,700 W.

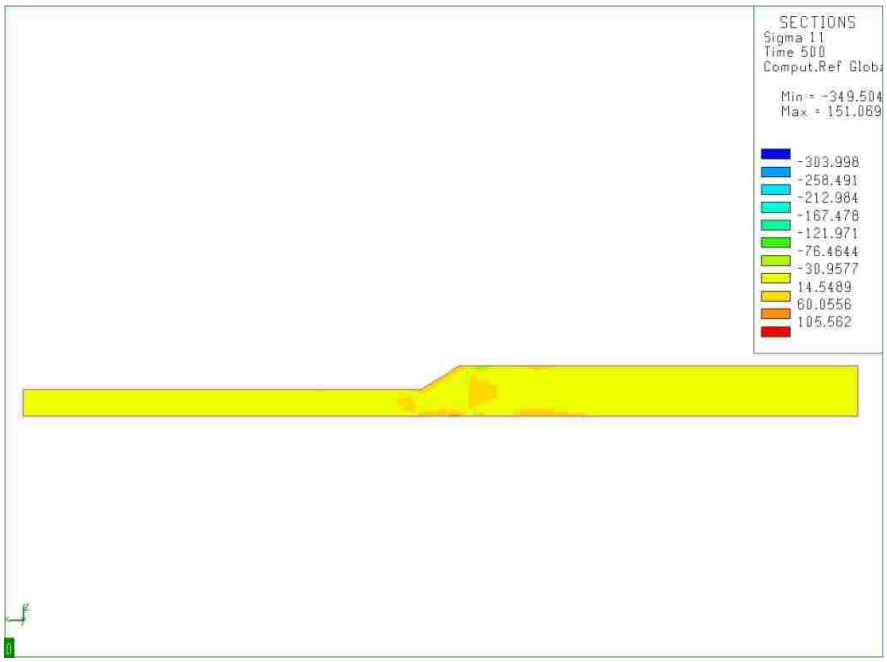

(a) Transverse residual stress

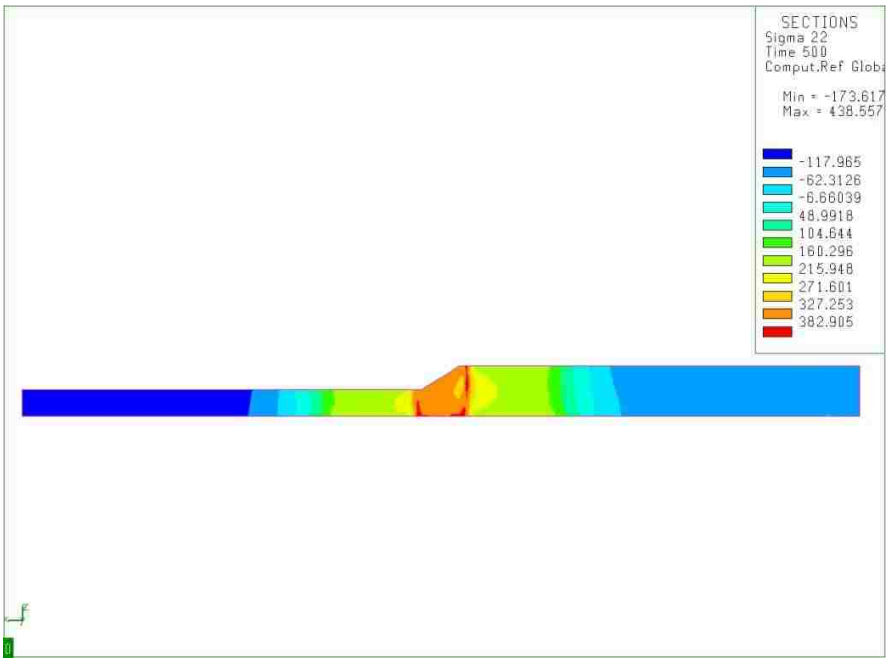

(b) Longitudinal residual stress

Figure 5.53 Predicted stress at mid-length of weld for Laser power of 3,000 W.

Fig. 5.54 - 5.55 shows the distribution of transverse and longitudinal residual stress on the top surface for three different welding speeds at the middle section of the plate length (y = 25 mm), respectively. This graph is given the residual stresses distribution along the x-axis. The tensile stresses are presented near the welding bead in both transverse and longitudinal stresses. For the transverse residual stress in the welded area, the tensile stresses increase as the laser welding speed increases. For longitudinal residual stress, increasing the welding speed results in increased peak stresses forming at the weld center. The former may be due to the reduction in heat input that accompanies an increase in welding speed. This would result in a reduction in the width of the high temperature zone. The latter could be a result of the increased thermal gradients during the higher speed welding.

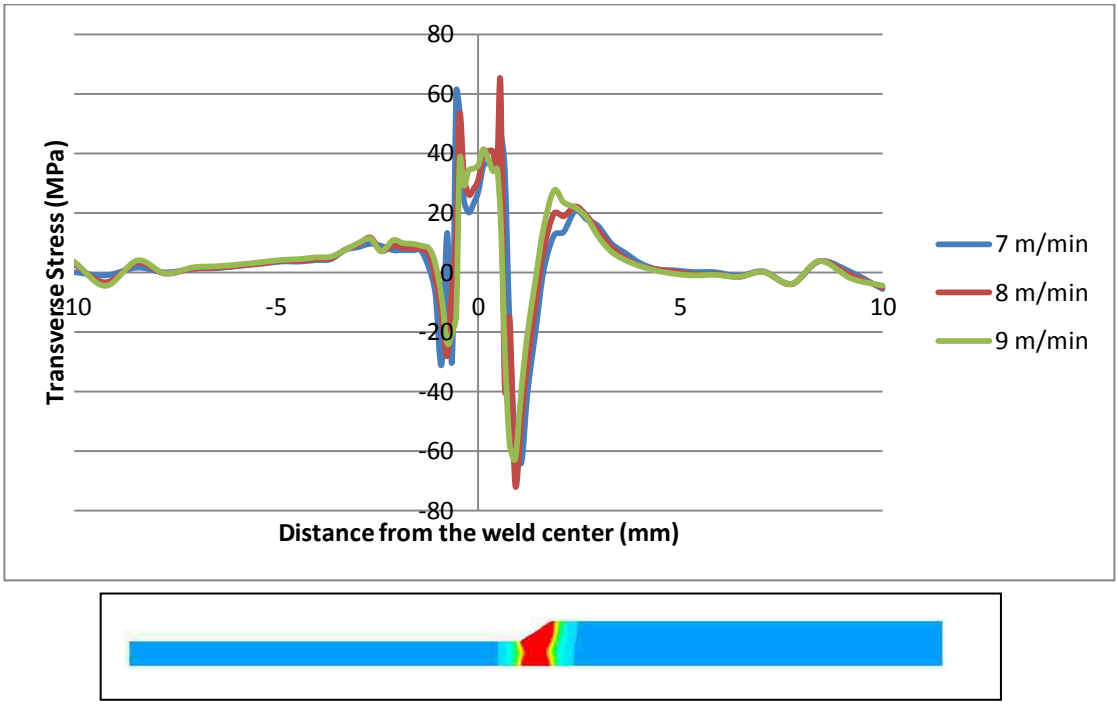

Figure 5.54 The effect of welding speed on transverse residual stresses

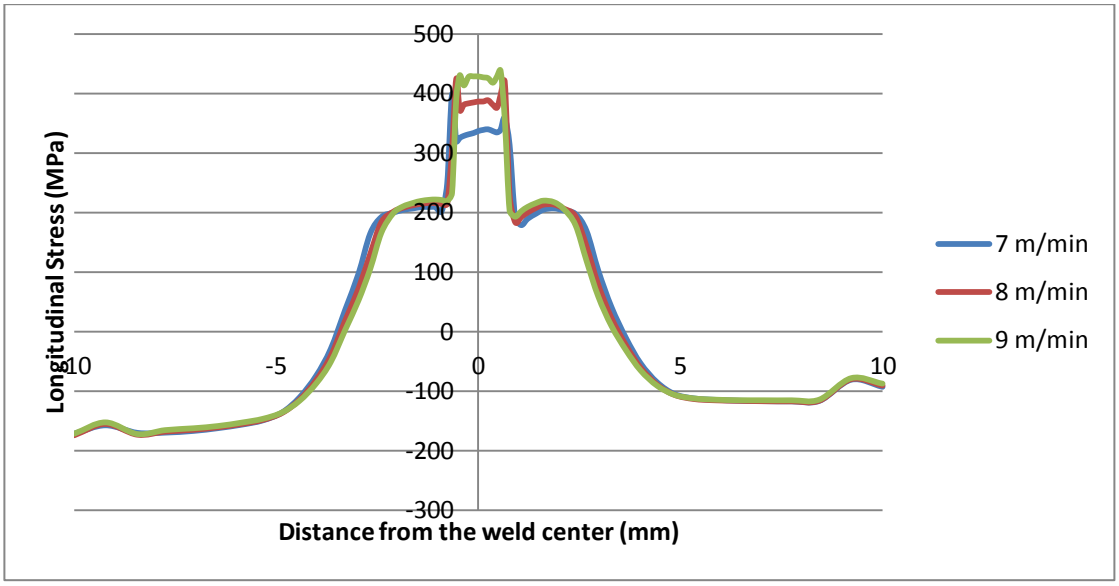

Figure 5.55 The effect of welding speed on longitudinal residual stresses

Figs. 5.54 - 5.55 show the distribution of the transverse (sigma 11) and longitudinal (sigma 22) residual stresses at the top surface, for three different laser powers. The plots are for the middle section of the plate length (y = 25 mm). This graph is given the residual stresses distribution along the x-axis. In the welded area, the tensile stresses decrease as the laser power increases. The possible reason is that higher laser power leads to plastic deformation and it contributes to relaxation of the thermo-mechanical stresses.

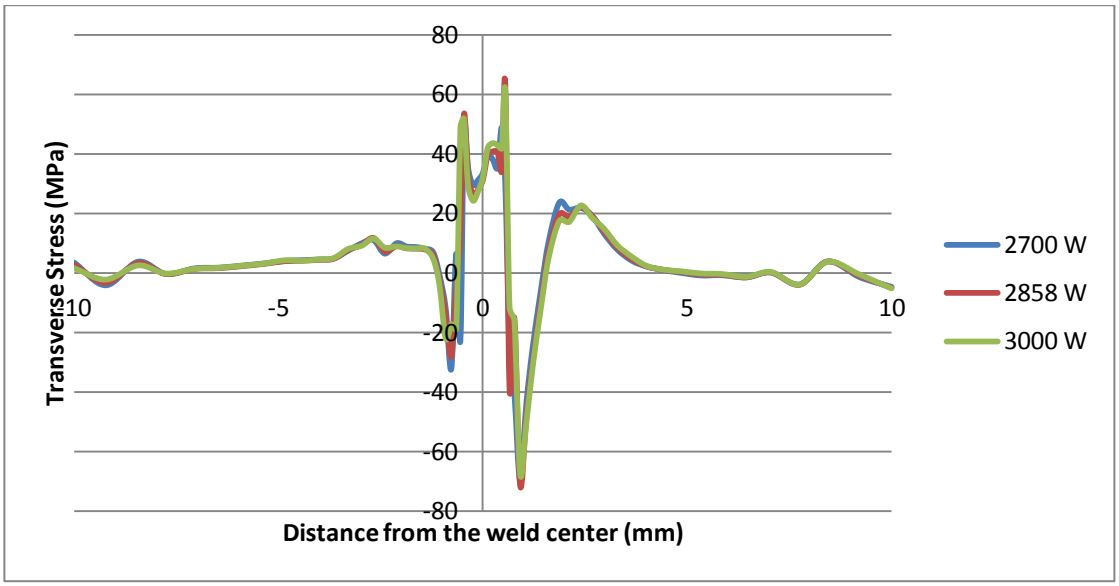

Figure 5.56 The effect of laser power on transverse residual stresses

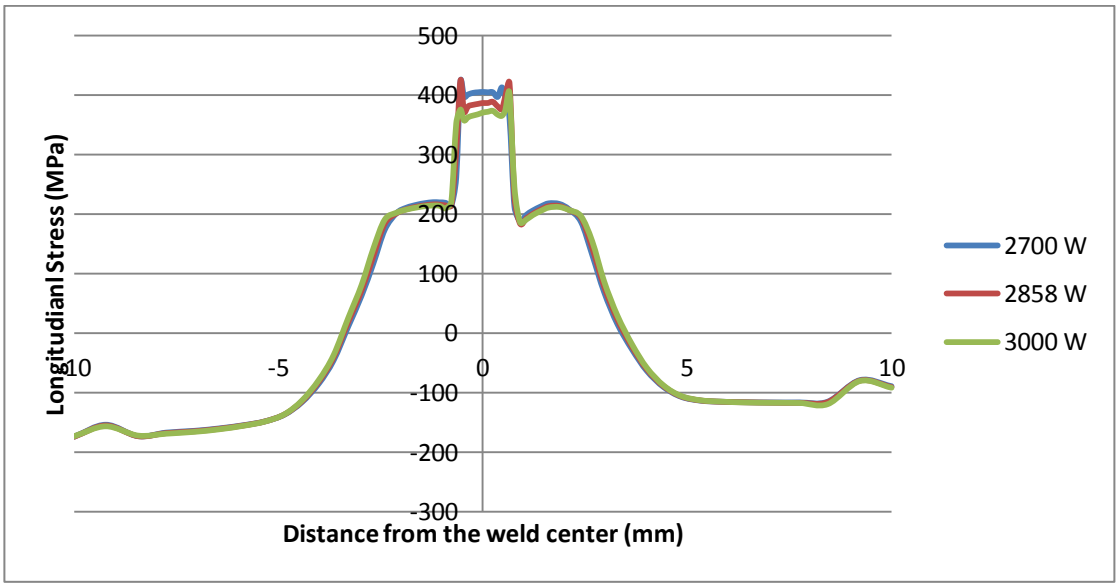

Figure 5.57 The effect of laser power on longitudinal residual stresses

5.2.3 Effect of boundary conditions on the laser welding results of thin metal sheets

5.2.3.1 Effect of heat loss

The simulated results of the temperature distribution for the different thermal boundary conditions are shown in Fig. 5.56. The maximum temperatures in all cases occur when the heat source has moved to the middle of sheet and the displacement values after cooling were summarized in the Table 5.3. The results show that the maximum temperature and displacement values are closely related due to analysis in the small area. In addition, the area of the heat source is very small, therefore the heat loss is not too different. In the case of conduction heat loss through the bottom surface, the heat loss is lower than the convection loss as a result the maximum temperature appears that case.

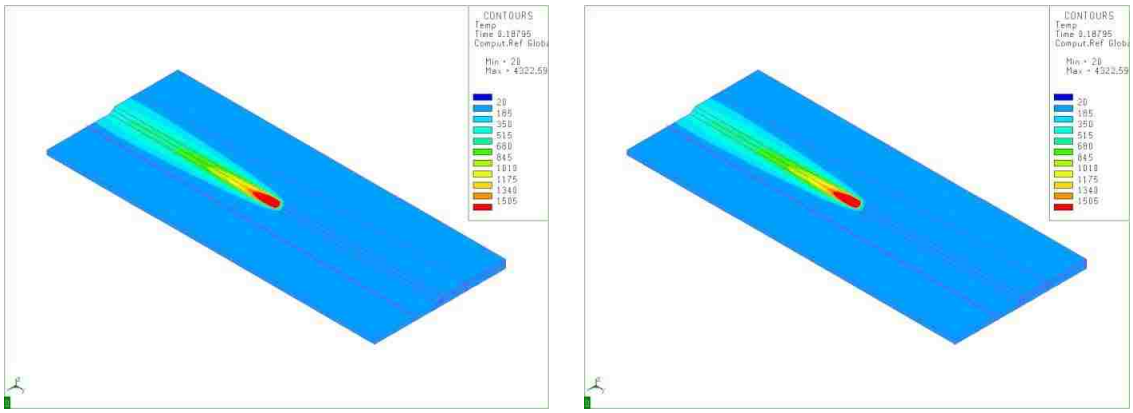

a) Type A (conv-rad bc at all surface) b) Type B(conv-rad bc at top and air-gap surface)

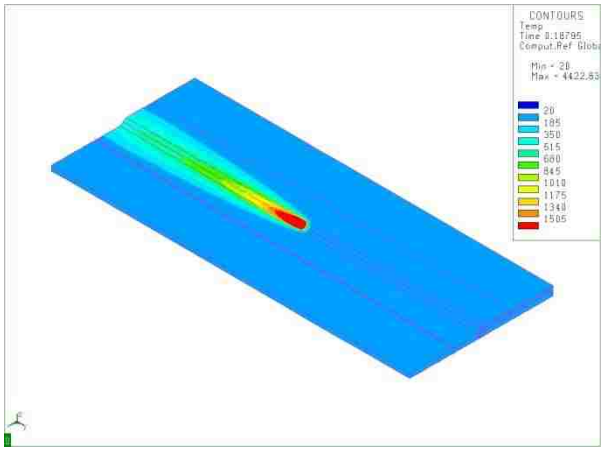

c) Type C (conv-rad bc. at top surface and cond bc at bottom surface)

Figure 5.58 Temperature distribution for difference thermal boundary conditions

Table 5.3 Temperature and displacement for difference thermal boundary condition.

Type of boundary condition	*Temperature* (^{o}C)	*displacement* (mm)
Type A	4,322.59	0.0798
Type B	4,422.67	0.0824
Type C	4,422.83	0.0828

5.2.3.2 Effect of clamping constraints

The influence of the external structural restraints, i.e., the fixtures, influences the residual stress and distortion. Three separate cases were studied. Case 1: As in the actual experiment the magnetic clamping was maintained the part completely cooled. Case 2: as the clamping was released after welding and cooling. Case 3: there was no clamping system during welding which was called unclamped condition. The simulated results of the deflection distribution for the different mechanical boundary conditions are shown in Fig. 5.59. It can be observed that substantial longitudinal bending and transverse bending are produced after welding in both cases. The final distortions are different, depending on the mechanical boundary conditions. In the first case, with rigid constraint at all clamping zone, the maximum bending is at the center area of the weld line and there is no longitudinal and transverse shrinkage due to the tight clamping and large sample size. The unclamping after welding (case 2) is shown in Fig. 5.59b. The deformation is highest at the end of the weld-line. Also there are longitudinal and transverse shrinkage and higher bending along the Y-direction in the thin metal sheet when compared to the thick metal sheet. In the case of unclamping (case 3), the deflection is highest at the corner of the specimen (Fig. 5.59c). Distortions in the Z-direction are shown in Fig. 5.60. In the case with rigid constraint, the distortion shape was a convex-like shape due to the restricted shrinkage. Longitudinal bending displacement (Z-Y plane view) is produced in cases with releasing clamping and unclamping, which was a concave-like shape. Predicted residual stresses for the

different mechanical boundary conditions were compared. The maximum residual stresses were produced in the rigid constraint case.

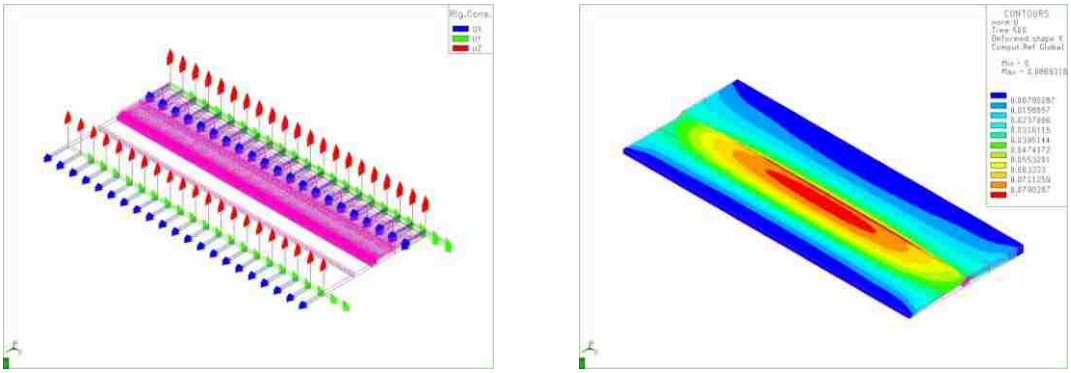

a) Case 1: Rigid constraint all edges

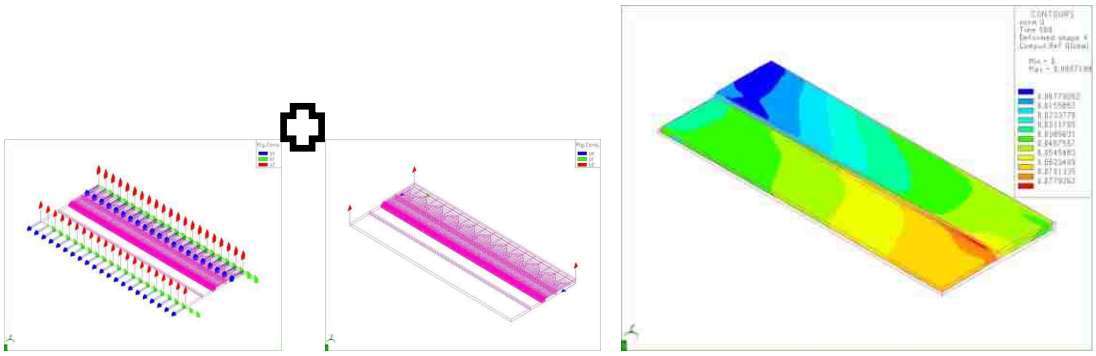

b) Case 2: Unclamping after welding

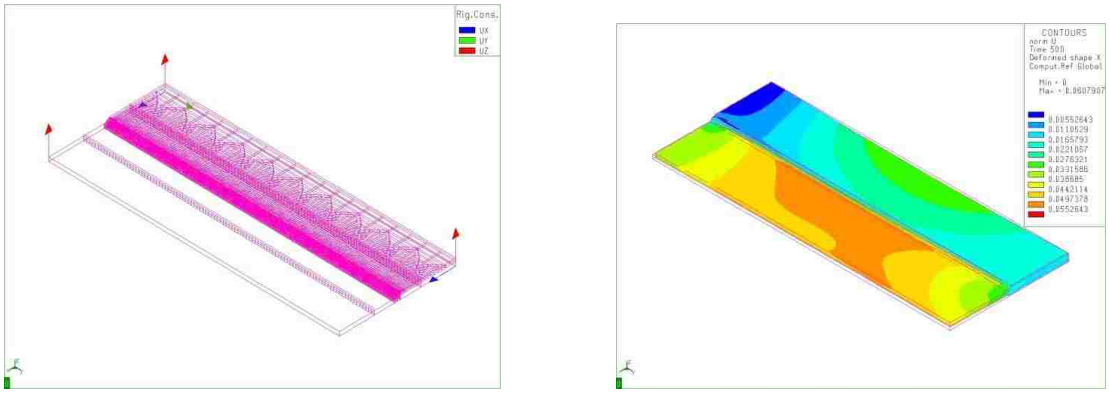

c) Case 3: Unclamping

Figure 5.59 Deflection distribution for difference mechanical boundary conditions

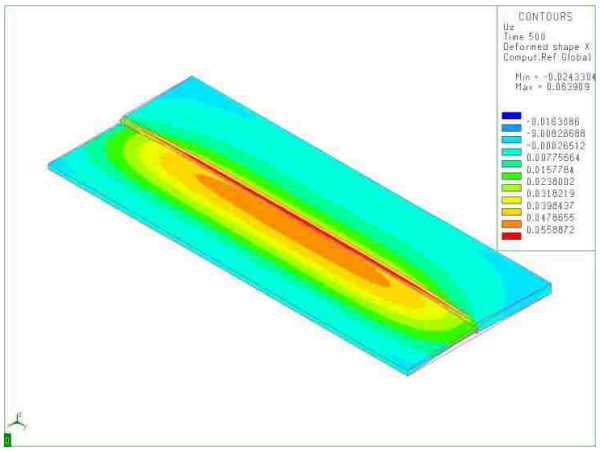

a) Case 1: Rigid constraint

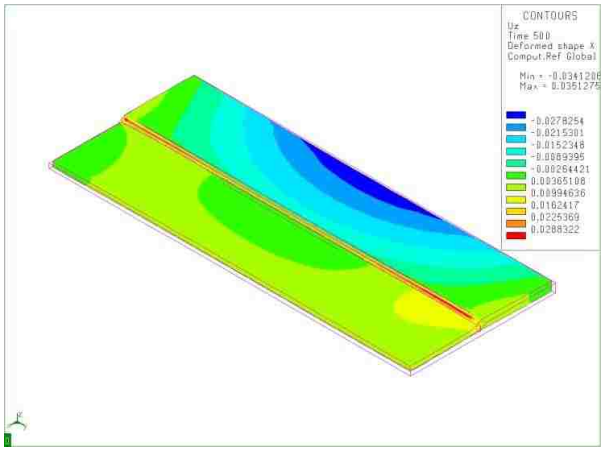

b) Case 2: Unclamping after welding

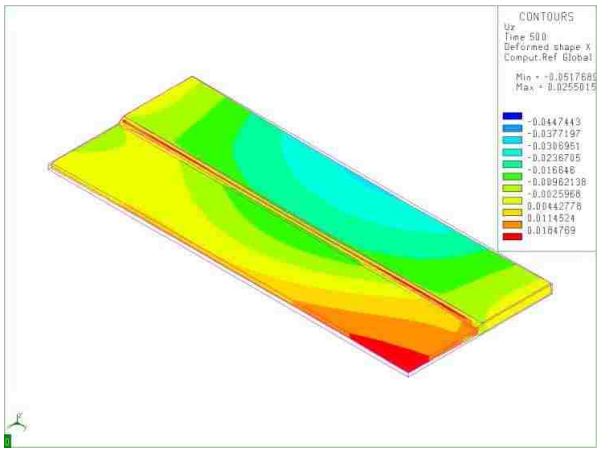

c) Case 3: Unclamping

Figure 5.60 Defection distribution in z-direction

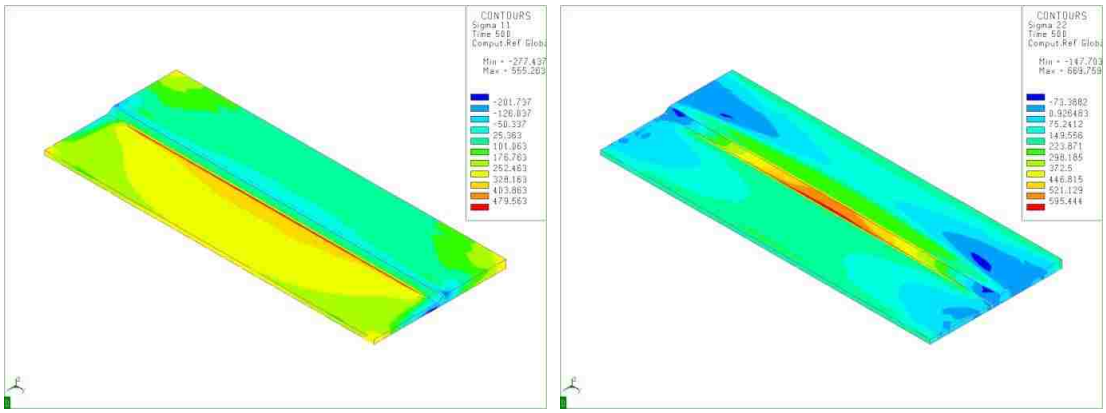

a) Case 1: Rigid constraint

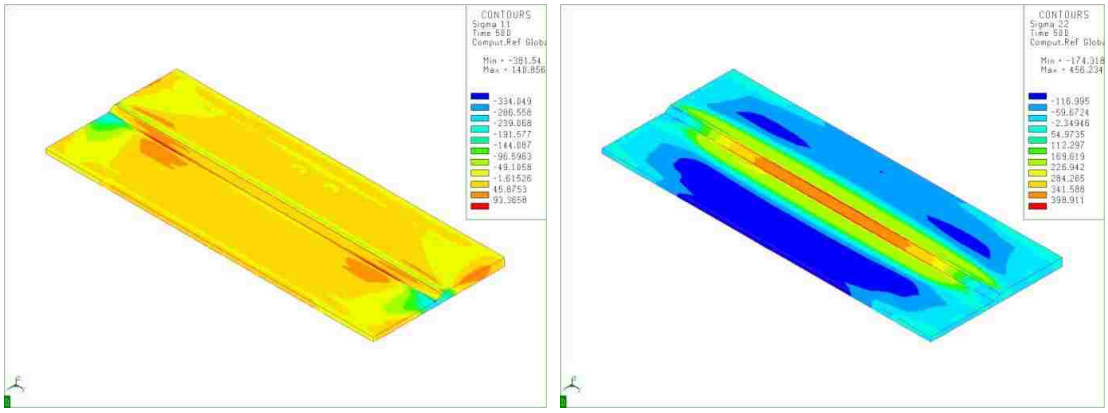

b) Case 2: Unclamping after welding

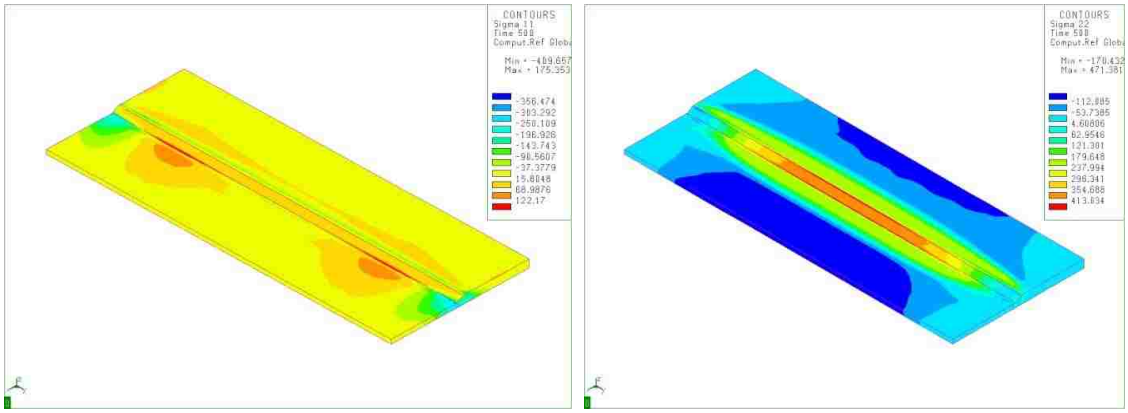

c) Case 3: Unclamping

Figure 5.61 Predicted residual contour for difference mechanical boundary conditions

5.4 Summary

For butt joint laser welding of thin metal sheets with different thicknesses, the experimental samples contained a sound weld without spatter and full penetration was achieved. The performance tests of the laser-welded sheet specimens were comparable to the base metal sheet. From the metallurgical analysis the full penetration weld pool shape presented an hourglass-like shape due to surface tension effects on the top and bottom of the thin sheet. Weld zone microstructure indicated ferrite mix with bainite for the low carbon steel, while martensite microstructure was observed at the carbon steel, contained with higher carbon element, due to rapid cooling rate.

The heat source development with a double conical heat source, i.e. an hourglass heat source, was applied within the SYSWELD code. Comparisons of the weld pool shape from the finite element simulation with the experimental results are in good agreement. The width of the weld pool decreased with increasing welding speed, because the laser power density applied to the metal sheet is reduced with increasing welding speed. The weld pool dimension is larger with increasing laser power, due to an increase in the laser power density. The effect of thermal boundary conditions, the heat loss, the surface convection, radiation and conduction, have little effect on the fusion zone boundary and distortion.

Zinc vaporizes at a temperature of 1180 K, whereas steel starts to melt at 1505 K. Because of this huge difference, problems occur during the laser welding of galvanized steels, especially when welding lap joints refer to Fig. 2.3. This problem is

less important in butt joint welds so the effect of zinc evaporation was neglected in this study.

Referring to the results of distribution of transverse and longitudinal residual stresses, it can be seen that the material in the weld is plastically deformed at elevated temperatures and significant tensile stress arise along the length of the sheet. The transverse shrinkage is mainly a result of the thermal strains during expansion and contraction during the welding process.

Due to the different thickness sheets, the distribution of temperature, deformation and residual stress are asymmetric. The good agreement between the experimental results and simulation results suggests that the model can be used as a tool for parametric examination of the laser welding process, which will lead to optimized values of the welding parameters.

CHAPTER 6

Gas Tungsten Arc Welding Results

In this chapter, GTAW experimental and simulation results, are described as well as comparison with laser welding results.

6.1 GTAW Experimental Results

The visual investigation, tensile tests, and hardness tests were carried out to evaluate performance and mechanical properties of the weld.

6.1.1 Visual investigation

Fig. 6.1 - 6.2 shows the top and bottom views of the TIG-welded butt joints obtained in experiments. There was no splatter and porosity from welding with the GTAW welding process. A sound weld with complete penetration was achieved and continuous without the presence of spatter or porosity.

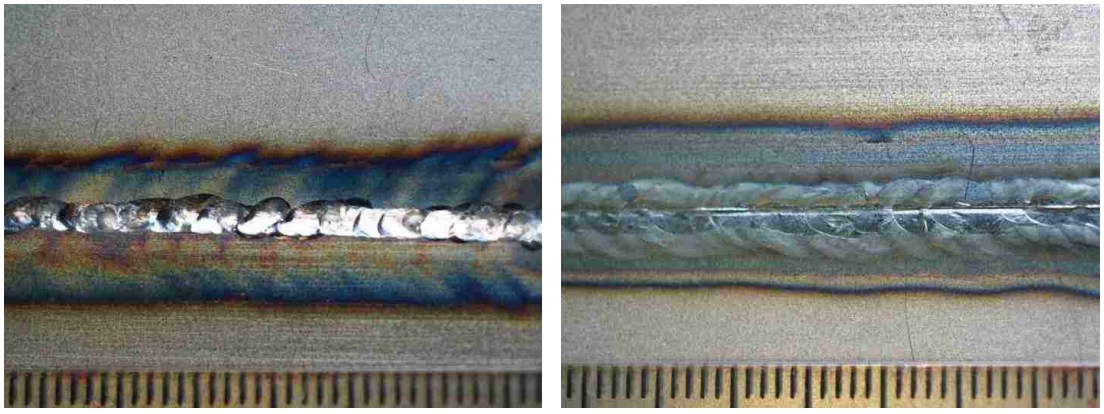

a) Top surface b) Bottom surface

Figure 6.1 The TIG butt joint for ASMT1

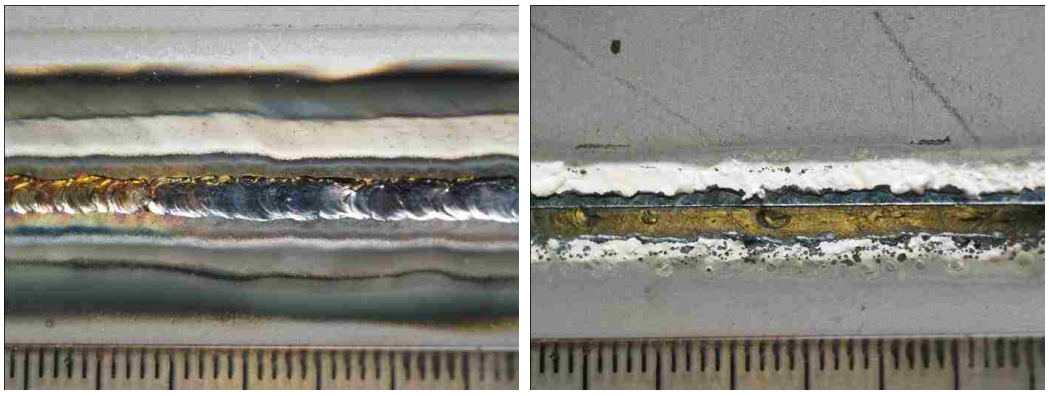

a) Top surface b) Bottom surface

Figure 6.2 The TIG butt joint for ASMT

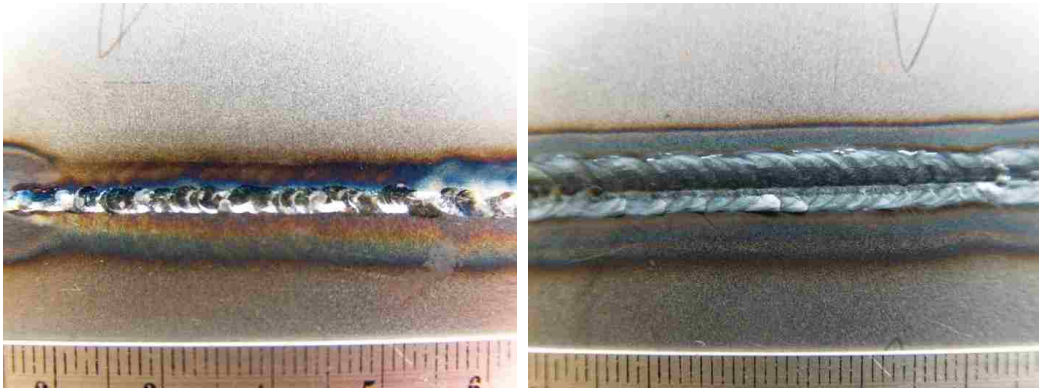

a) Top surface b) Bottom surface

Figure 6.3 The TIG butt joint for BSMT1

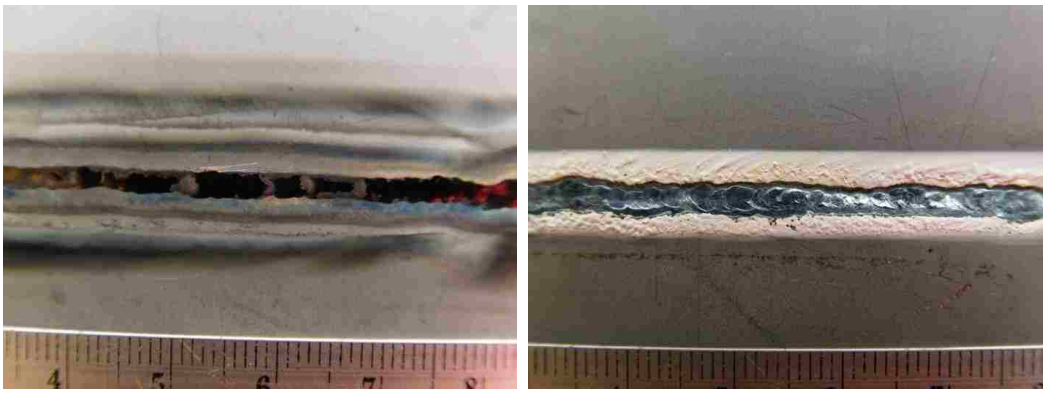

a) Top surface b) Bottom surface

Figure 6.4The TIG butt joint for BSML

6.1.2 Tensile Stress Test

Uniaxial tensile tests were conducted on the TIG-welded metal sheet until fracture occurred. The tensile specimens before testing compared to after testing are shown in Fig. 6.5. Some specimens fractured at the welded area, whereas other specimens fractured in the thinner sheet metal. Table 6.1 shows the mechanical properties obtained from the tensile tests of the TIG-welded metal sheet, which is plotted in Fig. 6.6.

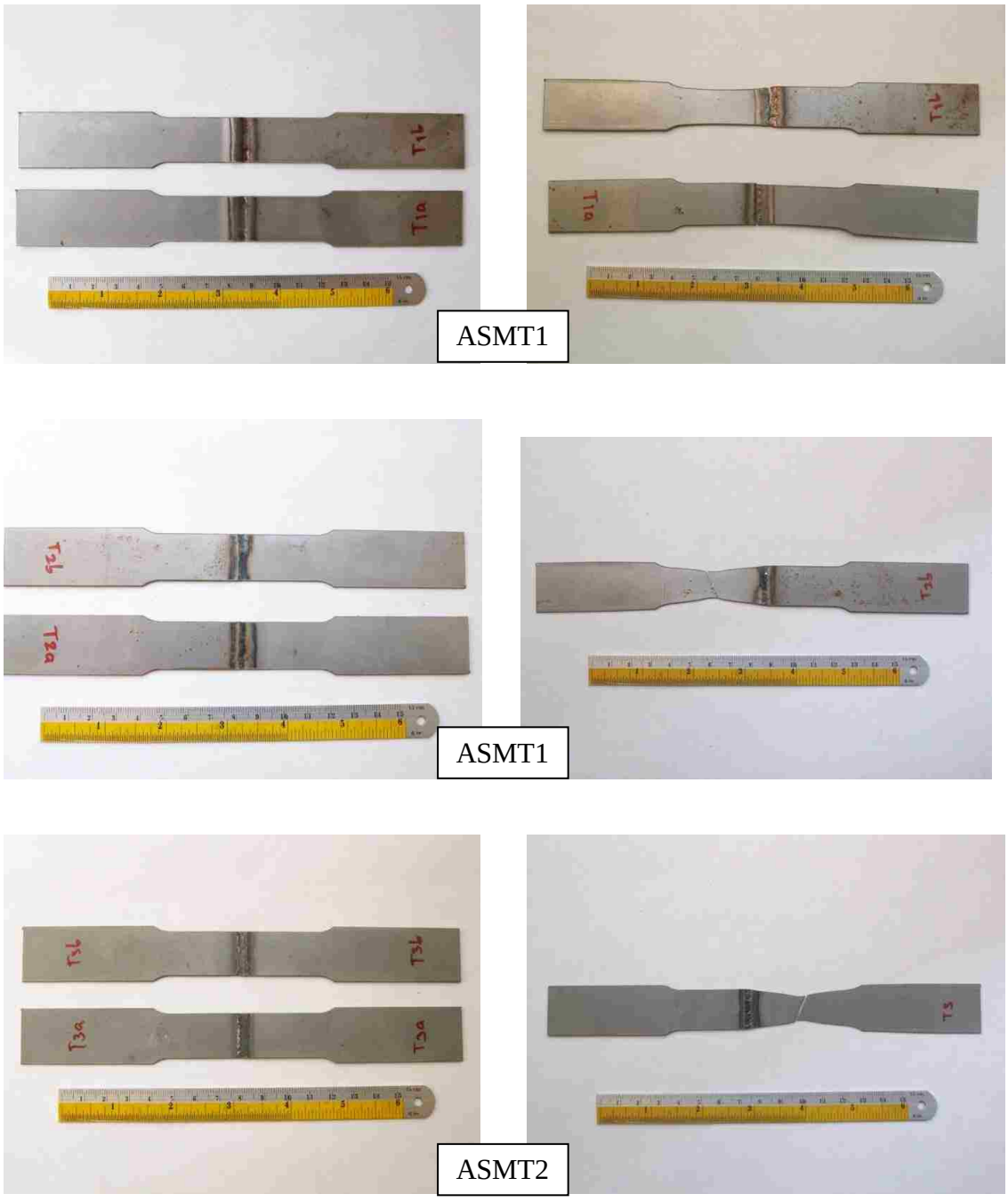

a. Before testing b. After testing

Figure 6.5 Comparison of the tensile specimens before and after testing

Table 6.1 Tensile test of the sheet specimens

Specimen No.	Cross-section area (mm^2)	Ultimate Tensile (N)	Tensile Strength (N/mm^2)
1-ASMT1	12.79	4226.12	330.33
2-ASMT2	12.79	3881.16	303.37
3-BSMT1	13.24	4213.48	318.38
4-BSMT1	13.25	4219.18	318.48
5-BSMT2	13.27	3971.80	299.23
6-BSMT3	13.22	3957.68	299.32

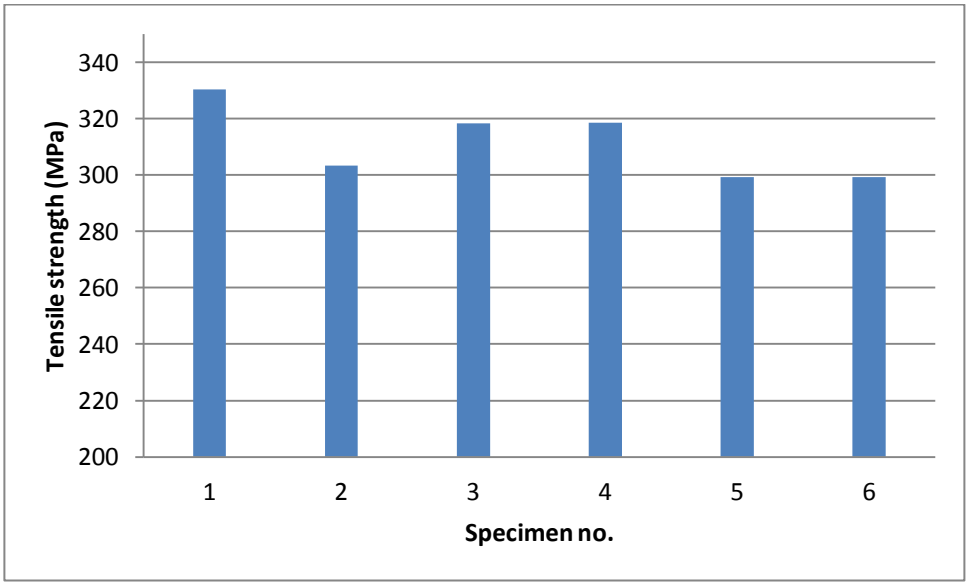

Figure 6.6 Tensile strength of the TIG-welded metal

6.1.3 Metallurgical Analysis

Some locations from the TIG-welded samples were selected to analyze microstructure and weld pool shape. Fig. 6.7 shows the microstructure and weld pool shape after welding using the manual TIG welding process. As shown in these figure, defects, misalignment and undercuts, were observed. The same sample is shown at a higher magnification in the Fig.6.8. In these figures, coarse grains were observed in the fusion zone. Fig. 6.9 - 6.10 shows the microstructure and weld pool shape of BSMT1 and BSMT2 specimens, respectively. In these figures, full penetration without defects was observed. Welding on the bottom side of the group A specimens to eliminate the undercut defect was performed as shown in Fig. 6.11. Heating on the bottom side results in a distorted welded area. For the FZ, the fine grain microstructures of bainite appeared in the thin sheet due to the higher cooling rate, whereas the coarse gain ferrite is observed at the thick sheet as shown in Fig. 6.12.

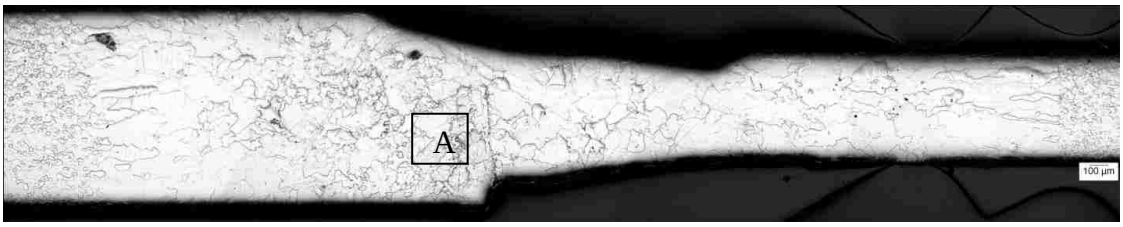

a) ASMT1

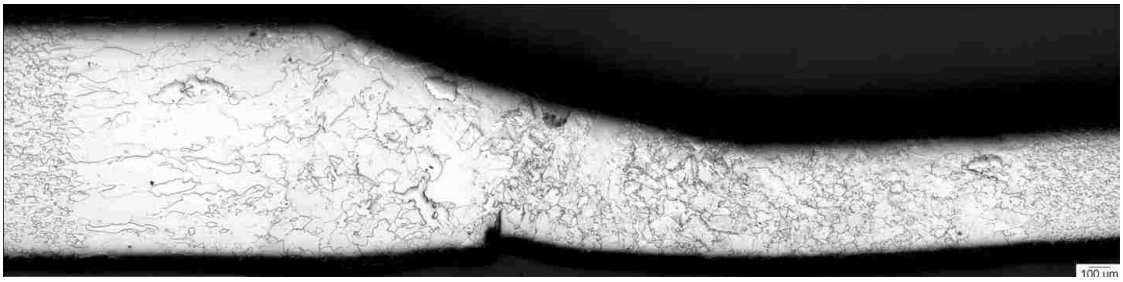

b) ASMT2

Figure 6.7 The weld pool geometry from TIG welding process

Figure 6.8 Higher magnification 10x of ASMT1 at A area in Fig. 6.7a

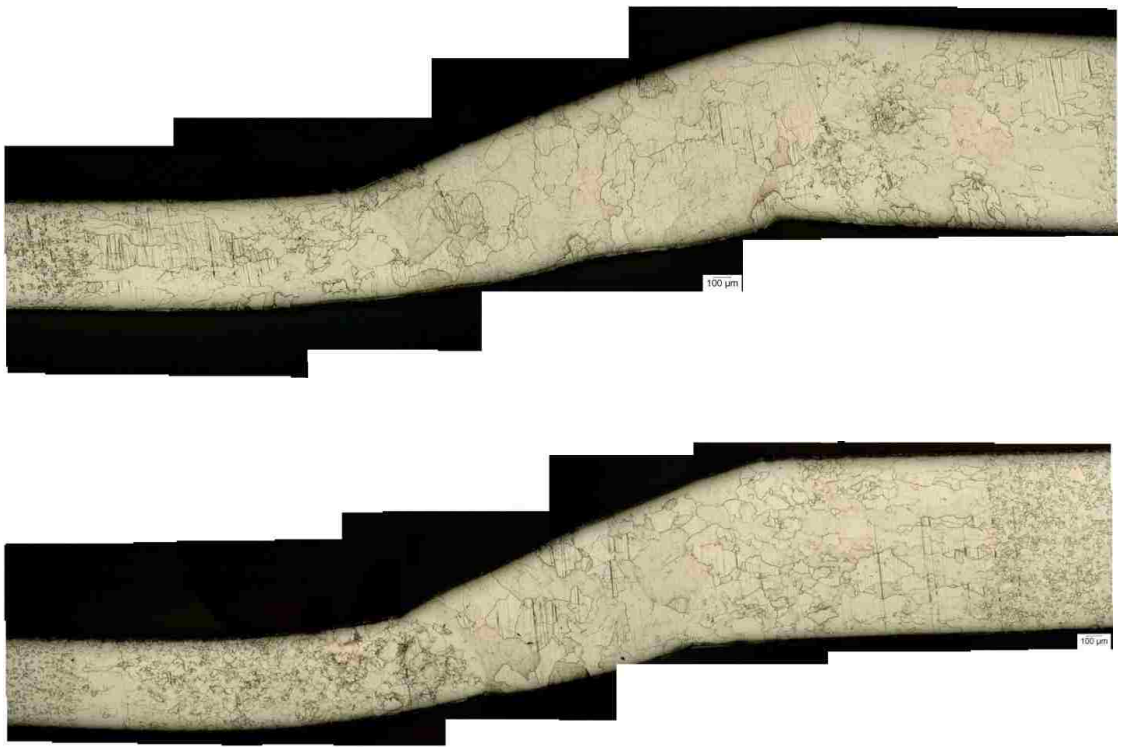

Figure 6.9 The weld pool geometry of BSMT1 in different locations.

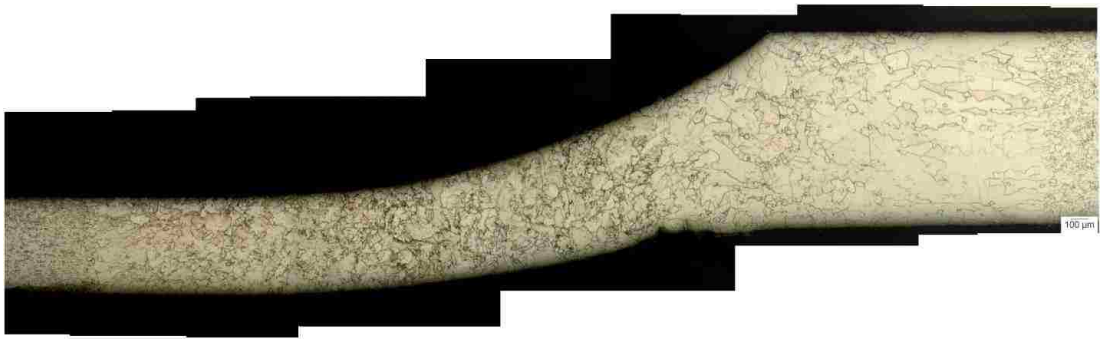

Figure 6.10 The weld pool geometry of BSMT2

Figure 6.11 ASMT2 with welding two sides

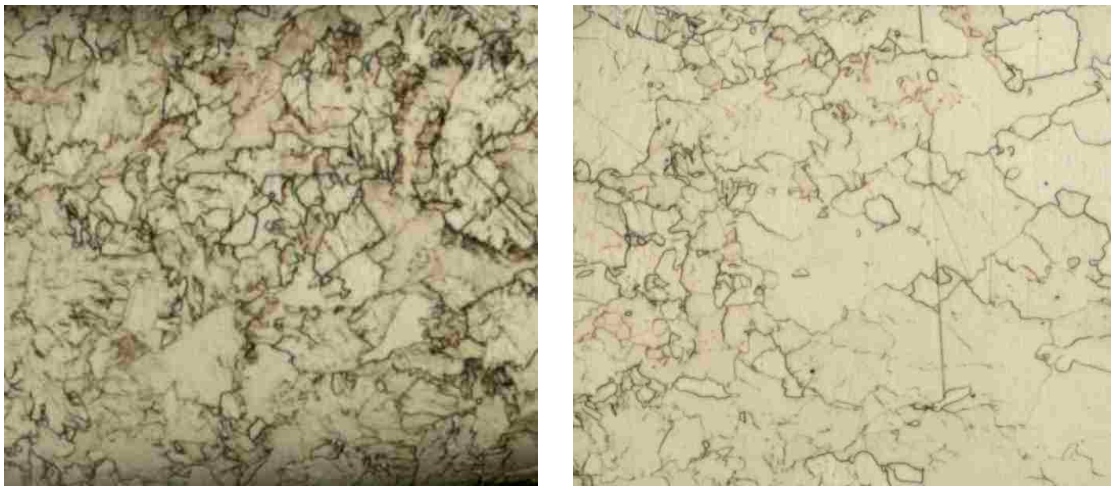

a) Thin sheet b) Thick sheet

Figure 6.12 Microstructure of welding area in; a) thin sheet b) thick sheet

6.1.4 Hardness Test

Hardness testing was carried out using a Leco Model M-400 microhardness unit with a 100g-200g load, the same as the laser-welded specimens. Hardness was measured over the fusion zone, the heat-affected zone (HAZ) and the base metal (Fig. 6.13). Fig. 6.14 - 6.15 shows the measured line and the hardness profiles across the weld zone and the heat-affected zone (HAZ) as well as the base metal. The microhardness values are a function of the distance from the weld centerline. The hardness of the base metal is less than 120 Hv, whereas the maximum hardness of the fusion zone is 121-165 Hv. The hardness values of each weld region are affected by its chemical composition and microstructure. In the fusion zone, the weld in the thin sheet has a higher hardness value than that of the thick sheet due to the fast cooling.

Figure 6.13 The location of the hardness scans of unequal thickness TIG-welded specimen using a 200g load.

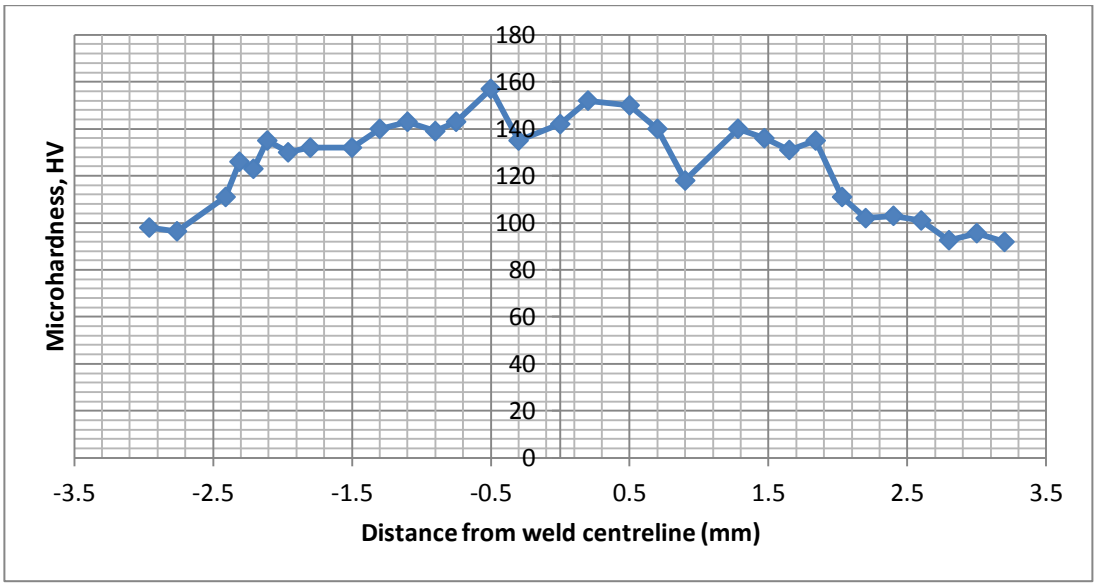

Figure 6.14 Microhardness profile of a welded joint between unequal thickness carbon steel sheet.

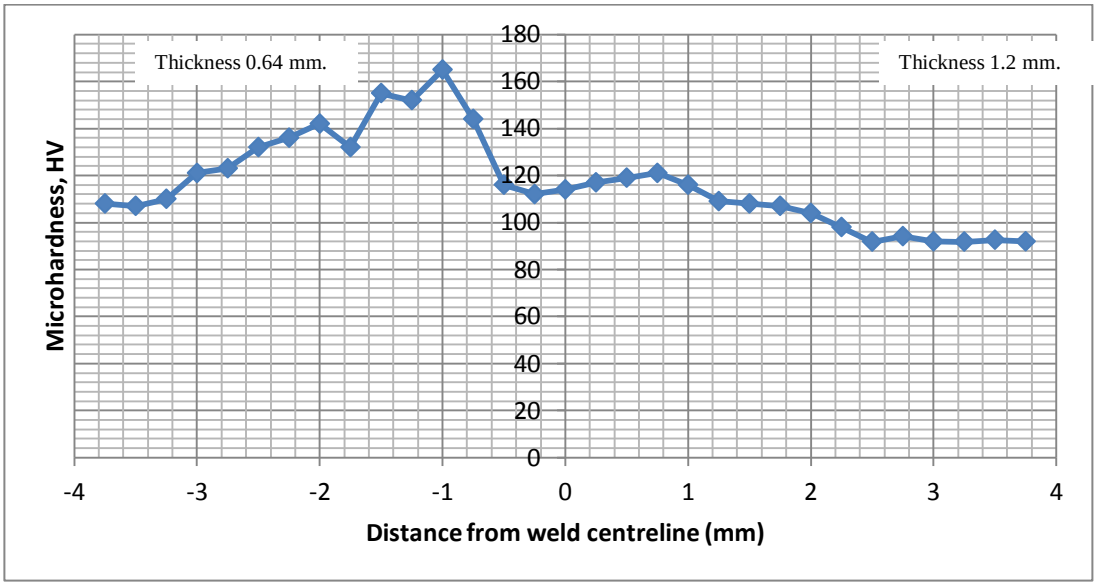

Figure 6.15 Microhardness profile of a welded joint.

6.2 TIG Welding Simulation Results

Using the geometry, the mesh and the heat flux models described in previous chapters and the geometrical parameters of the weld pool that were measured from the metallographic investigation, the TIG welding process on butt-joint welds with different thickness sheets was simulated.

6.2.1 Thermal Results

In this particular study, the thermal results are used to compare the weld pool shape between the simulation results and the experimental results. The size and shape of the weld pool from the metallurgical results was used to compare with the thermal results.

Fig. 6.15 shows the temperature distribution when the welding torch passes the center position at the coordinate of y = 25 mm in the welding direction.

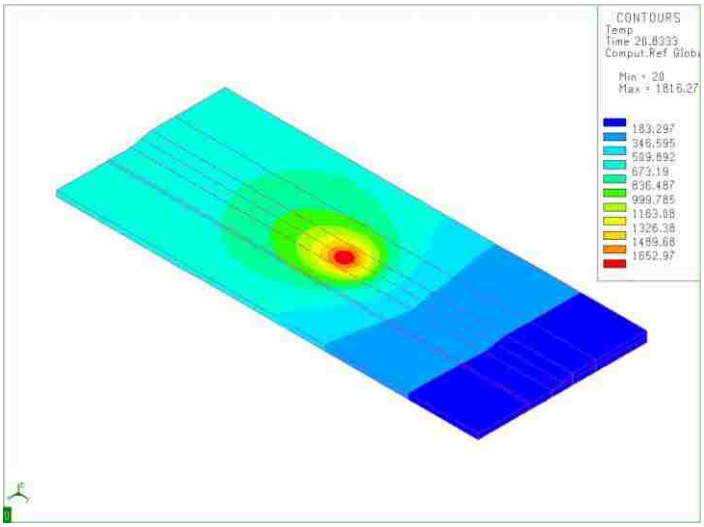

Figure 6-15 Distribution of the surface temperature of the low carbon steel sheet at t = 20.8s.

In Fig. 6.16, the temperature evolution on the top surface along weld line at the starting node, middle node and last node, during the laser welding process are illustrated. It can be observed that heating is very steep, leading to local heating, while the cooling process is relatively fast due to the convection and radiation heat transfer.

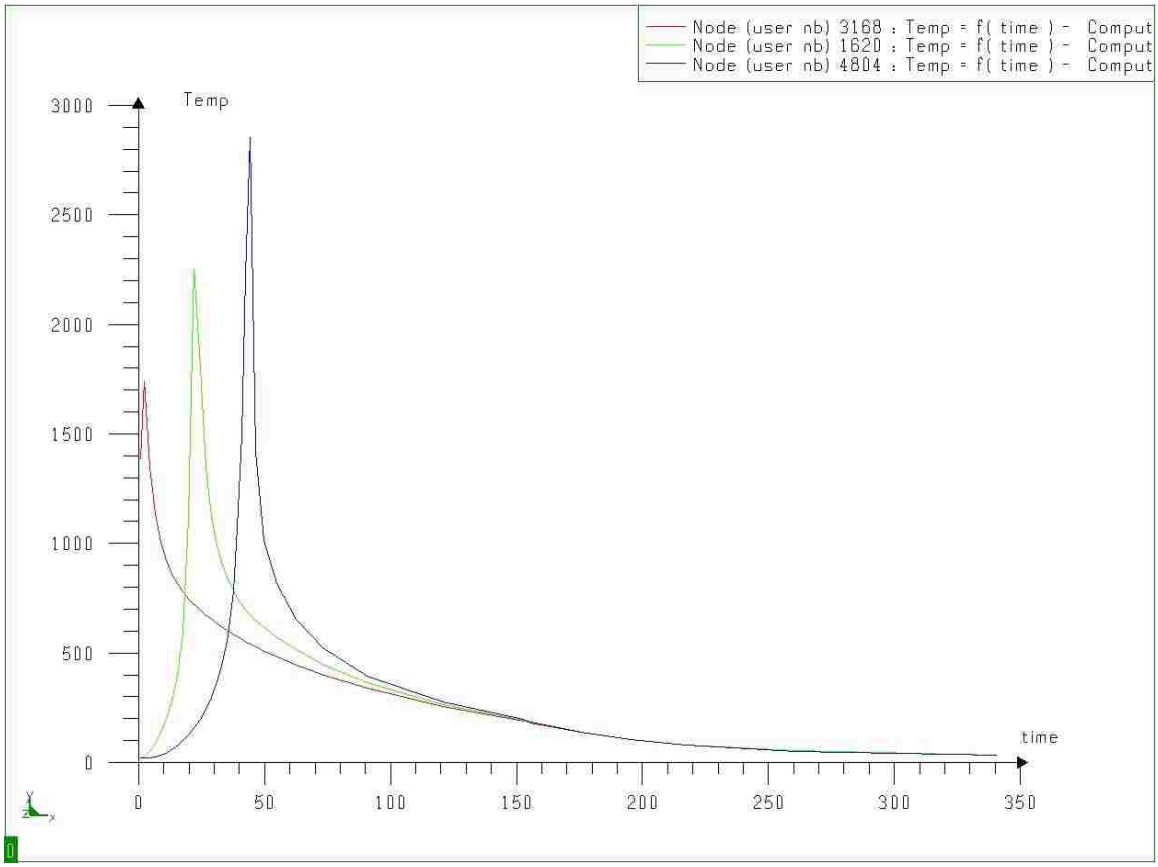

Figure 6.16 Temperature evolution on the top surface at start node, middle node and last node.

The temperature distribution in the cross-section perpendicular to the welding direction is presented to compare with TIG weld experiment. Fig. 6.17 compares the TIG weld pool shape between experiment and simulation result for BSMT1.

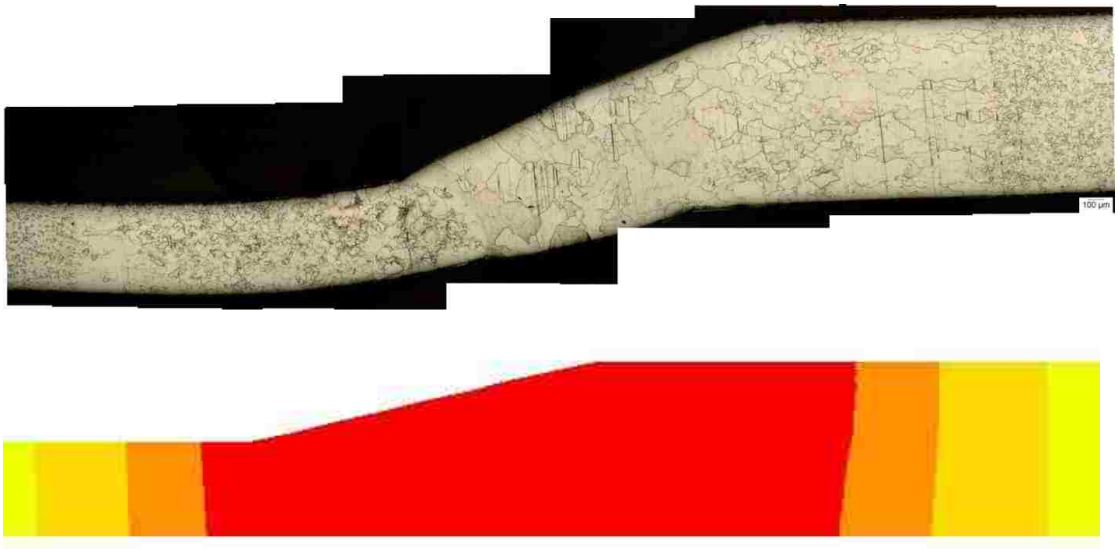

Figure 6.17 Comparison of TIG weld pool distance between experiment and simulation.

6.2.2 Mechanical results

Distortion and residual stresses in the TIG welding samples was also determined. C-shaped clamps were used and released after welding. Since the parameters for TIG welding; including power, welding speed and clamping conditions were different from laser welding, the mechanical results, as expected, were different.

6.2.2.1 Distortion analysis

The results of displacement after cooling and unclamping for different cases in TIG welding are shown in Fig. 6.18. The contours of the results represent the normal displacement, the magnitude of the displacement vector (Fig. 6.18a). The finite element predictions were compared with the average measured distortions for BSMT1 case as shown in Fig. 6.19.

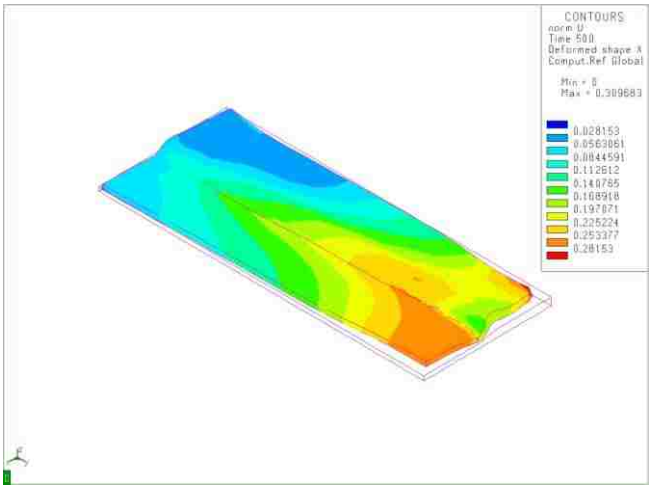

a. Normal displacement

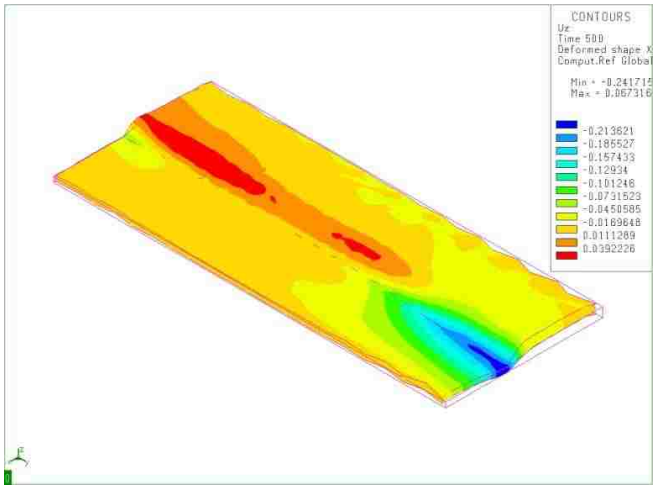

b. z-axis displacement

Figure 6.18 Normal displacement and z-axis displacement of TIG welding at 500 seconds

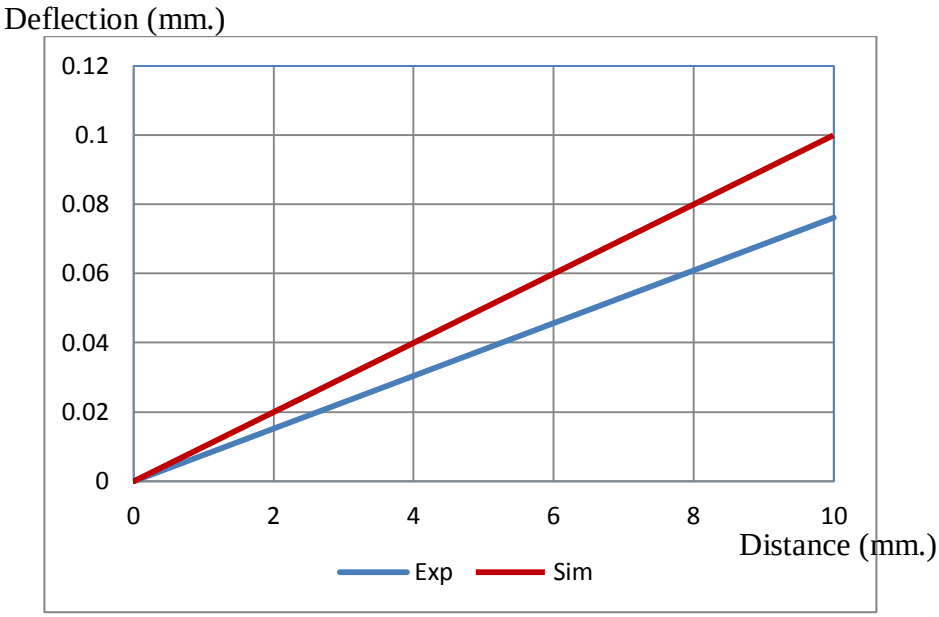

Figure 6.19 Comparison of distortion between simulation and experiment results for BSMT1

6.2.2.2 Stress analysis

The distribution of transverse (sigma11) and longitudinal (sigma22) residual stresses on the surface after cooling and with unclamping, is shown in Fig. 6.20. Stress concentrations occurred at the locations that were fixed due to wide range of heat transfer distribution.

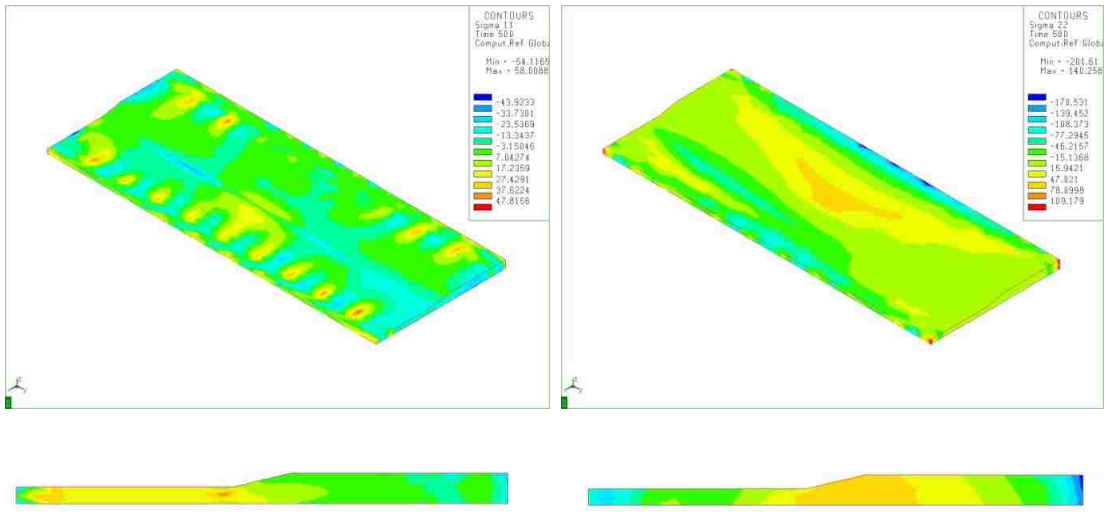

a) Transverse stress b) Longitudinal stress

Figure 6.20 The distribution of transverse and longitudinal residual stresses on the surface

6.3 Comparative evaluation of TIG welding and laser welding

The fundamentally different welding methods in TIG welding and laser welding were used for butt joint welding of different thickness metal sheets. The laser process allows much higher power density and welding speed than the TIG process. In the present study, the laser welding speed was around 8 m/min, whereas the TIG welding speed was approximately 100 times lower, at around 0.1 m/min. The characteristics of both methods are discussed, focusing on the influence of each welding parameter.

6.3.1 Weld bead formation and its mechanical properties

Fig. 6.21 shows the top surfaces for both laser welding and TIG welding. For the laser welding, the weldseam surface is smoother and narrower. Cross-sections of laser and TIG welds are shown in Fig. 6.22. It can clearly be seen that the weld bead width produced with TIG welding is wider than laser welding. The microstructure for laser welding is finer than TIG welding, due to the higher cooling rate in laser welding. Since laser welding has a much higher energy density compared with TIG welding, it melts the metal in a shorter period of time and the melted metal can rapidly then solidify. In addition, the HAZ in laser welding is much smaller than that in the TIG welding sample. Because of the rapid solidification rate in laser welding, the grains do not have sufficient time to merge and coarsen. In the HAZ near the base metal, equiaxed grains were formed. The granular grains grew along the radial direction because the thermal gradient along this direction. Table 6.2 compares aspect ratio (weld penetration/width) between laser welding and TIG welding. Laser welding compared with TIG welding

produced higher aspect ratio (deep penetration/width of weld bead) due to the high energy density of the laser welding processing.

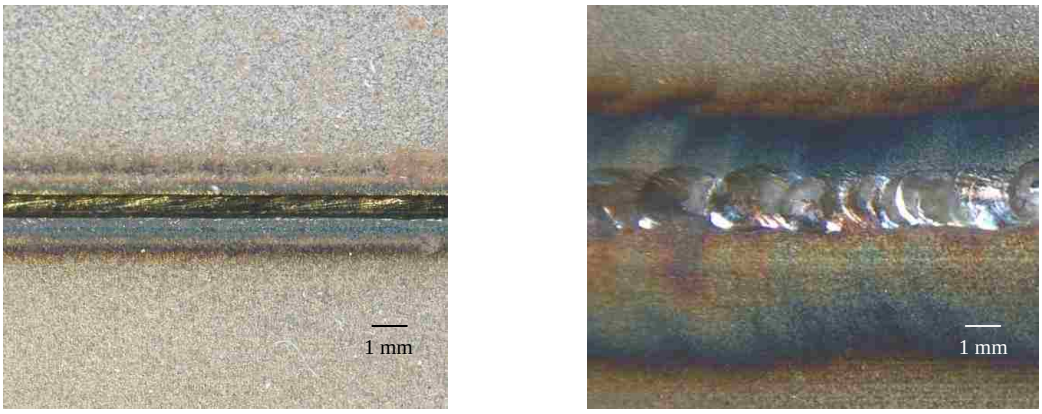

Figure 6.21 Weld top surface obtained using laser and TIG welding

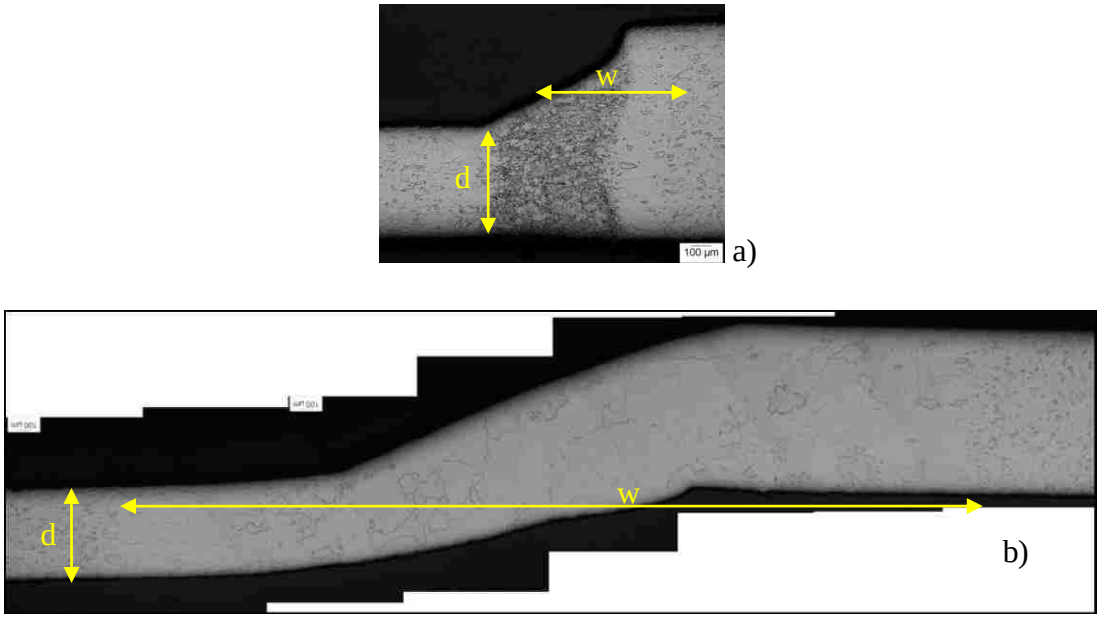

Figure 6.22 Weld cross-section a) both laser and b) TIG welding

Table 6.2 Weld bead aspect ratio

Welding process	Aspect ratio (d/w)
Laser	0.68
TIG	0.1

The transverse distribution of hardness across the weld produced with laser welding is higher than TIG welding due to the higher cooling rate in the laser welding (Fig.6.23). For tensile tests, some of the TIG-welded specimens failed at the weld due to weld defects such as lack of fusion and mismatch. With the failure occurring at the thinner sheet for both welding processes, there was no significant difference in mechanical strength.

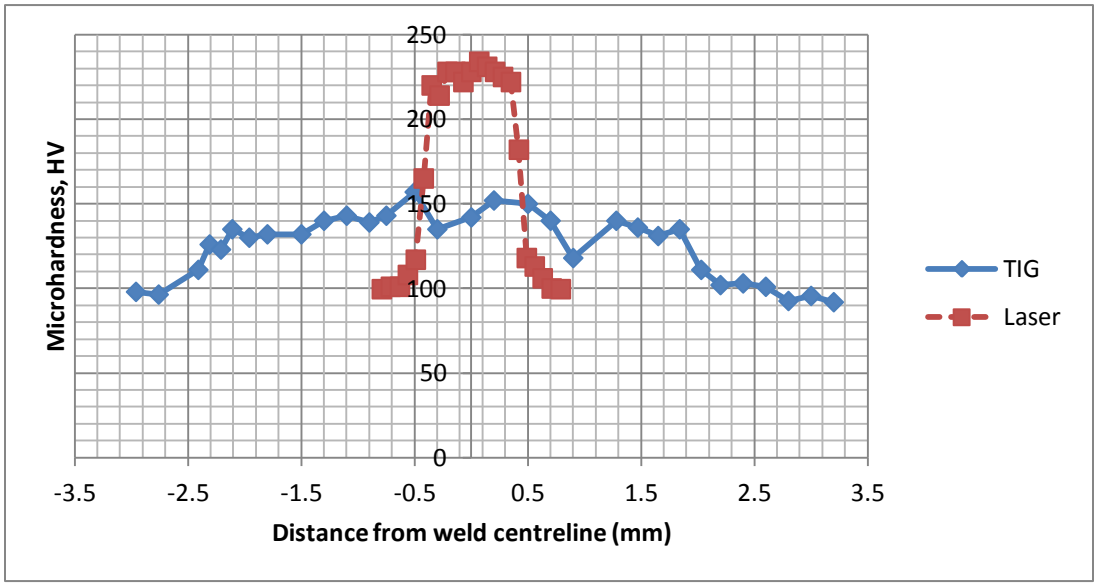

Figure 6.23 Comparison of hardness between the laser welding and the TIG welding

6.3.2 Cooling rate

The amount of heat input per unit length of the laser welding of 21.5 J/mm is lower than the TIG welding of 141.6 J/mm. The cooling rate of the laser welding is higher than the TIG welding due to lower amount of heat input per unit length of the laser welding. Fig. 6.24 shows the cooling rate comparison between the laser welding and the TIG welding.

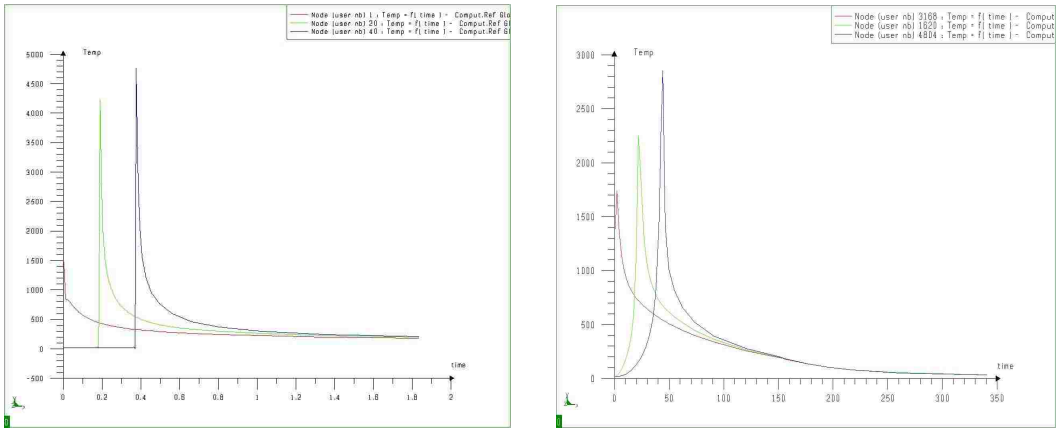

a) The laser welding b) The TIG welding

Figure 6.24 Cooling rate comparison

6.3.2 Amount of distortion of welded joint

A comparison of the distortion for the two welding methods is shown in Fig. 6.25. The amount of distortion in laser welding is one third of that in TIG welding. A comparison of the amount of distortion for the two welding methods at 20 mm from weld line is in shown in Fig. 6.26. Welding locally heats the steel sheets and the

adjacent cold metal restrains the heated material. This generates stresses greater than the yield stress, causing permanent distortion of the component. The TIG welding provides the higher heat input when compared with the laser welding. Consequently, the width of the tensile stress region is greater than from the laser welding, which explains the greater distortion with the TIG welding.


a)

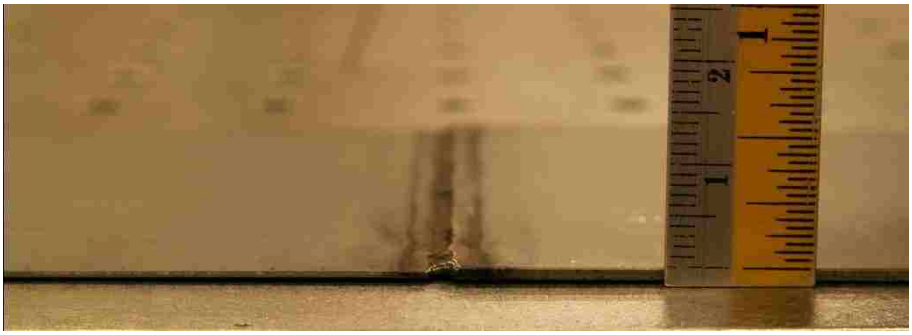
b)

Figure 6.25 Distortion in a) laser and b) TIG welding

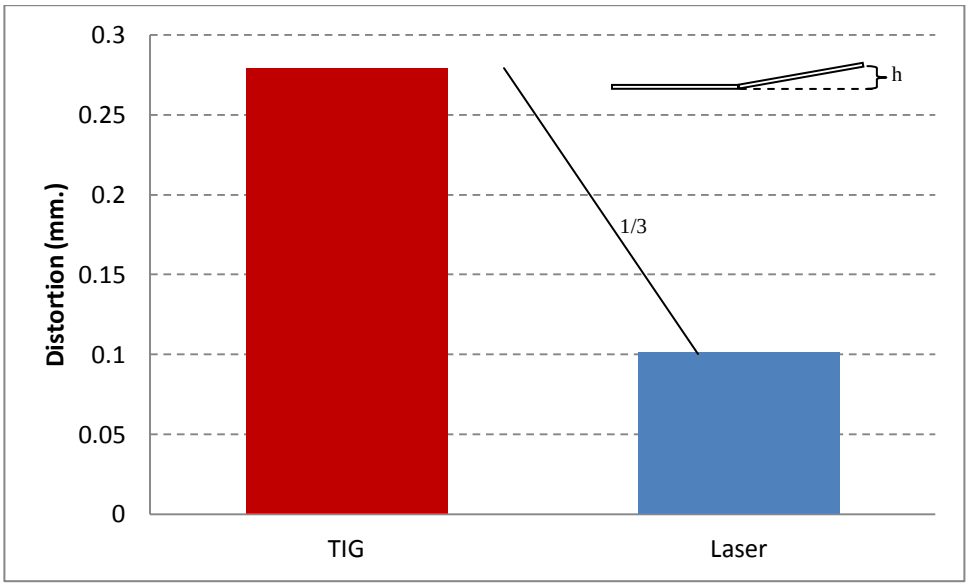

Figure 6.26 Amount of distortion at 20 mm from weld line

6.3.3 Amount of residual stress

A comparison of the predicted residual stresses for the two welding methods is shown in Fig. 6.27. The thermal contraction of the weld metal and the adjacent base metal are restrained by the areas farther away from the weld metal. Consequently, after cooling, residual tensile stresses exist in the weld metal and the adjacent base metal, while residual compressive stresses exist in the areas farther away from the weld metal. The amount of residual stress in the welding zone is largely produced from laser welding process when compared with TIG welding process due to higher intensity power. On the other hand the amount of residual stress at the edge from TIG welding is higher than in laser welding due to larger fusion zone (wider weld pool).

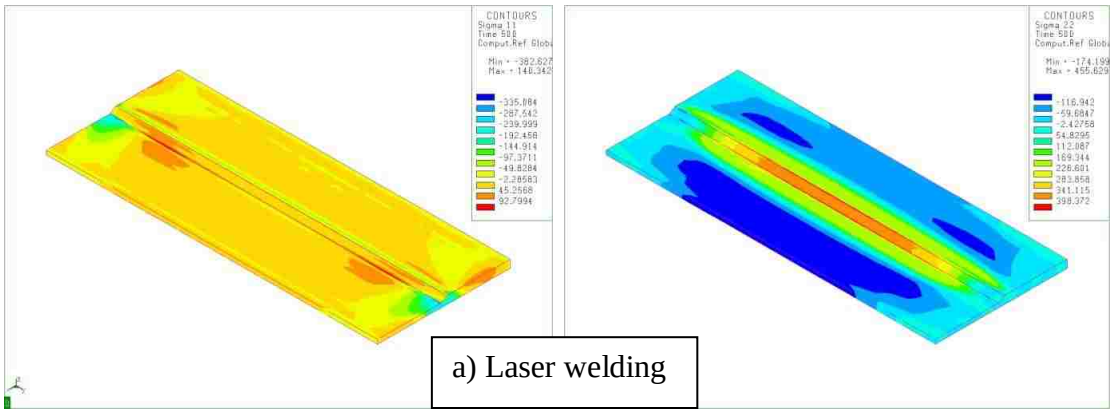

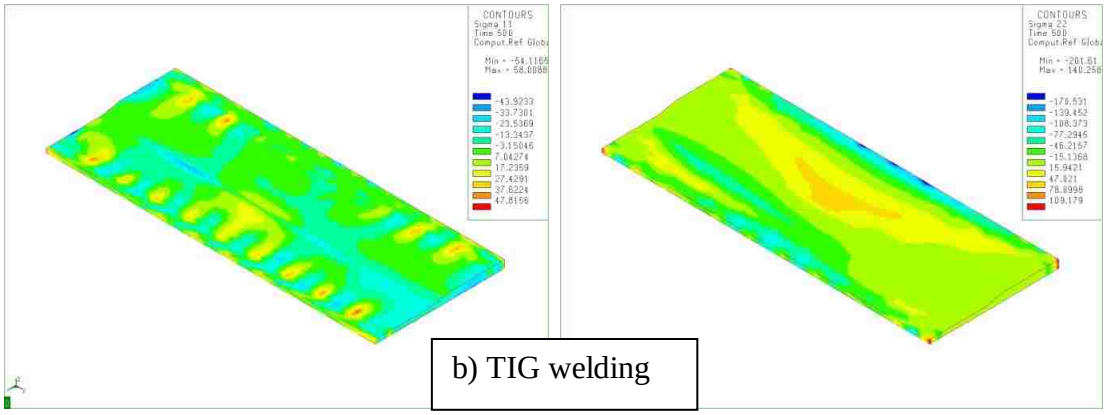

Figure 6.27 Amount of residual stress at middle of weld line

6.4 Summary

Due to the different thicknesses of the welded metal sheets, the distribution of temperature and residual stress are asymmetric.

Referring to the results showing the distribution of transverse and longitudinal residual stresses in Fig. 6.20., it can be seen that the material in the weld is plastically deformed at elevated temperatures and significant tensile stresses develop along the length of the sheet. In other areas of the welded sheet, the residual stresses are much

lower than the material yield strength. This indicates that the transverse shrinkage is mainly a result of the thermal strains during expansion and contraction during the welding process.

Laser welding compared with TIG welding produced higher aspect ratio and finer grains due to the high energy density of these processing. Laser welds were shown to be equal to, or better in quality than TIG joints on tensile strength test.

CHAPTER 7

Conclusions

The present work compares both experiment and simulation of welding for tailor welded blanks using laser welding and gas tungsten arc welding. A three-dimensional finite element model was developed to simulate these welding processes and predict the final distortions and residual stresses for a butt joint welded specimen. The finite element calculations were performed using the SYSWELD FEM code, which takes into account thermal and mechanical behavior. A number of welding experiments were conducted to verify the modeling results.

The developed welding model has the advantage as it is independent of any parameter. Simulation results can also help researchers in enhancing their ability to choose proper welding process parameters. This research deals with the subject of temperature distributions, residual stresses, and residual deformations during and after welding. This research also is useful for design, analysis, test and production engineers.

7.1 Laser and TIG welding process

This research effort was successful in applying two very different heat source models for the different welding processes of interest.

The finite element models for laser welding included a new heat source model, the hourglass heat source that can be used to predict the weld pool shape that results from tension effects on the top and bottom surfaces of butt welded joints in thin sheets.

For the TIG welding, the finite element method utilized a double ellipsoid heat source, that can be used to predict the weld pool shape, distortion and residual stress for butt welded joints in thin sheets.

This research achieved a suitable picture of welding behavior for both laser and TIG welding, to generate a high performance of welded thin metal sheet with a full penetration of weld pool.

The objective of this research is to study a computational and experimental effort to qualitatively understand the weld pool shape, distortion and residual stress for continuous laser welding and manual pulsed gas metal arc welding of TWBs.

7.2 Comparison of Laser and TIG welding

Sound welds without major defects and full penetration can be produced via laser welding. High performance of welding products can find in the laser weld metal sheet as a result of tensile testing. Laser welding can produce weld beads having high aspect ratio (penetration/width) due to the high energy density. The Nd:YAG laser produces the finer weld microstructure, whereas TIG with Ar gas shielding produces the coarser microstructure. This is due to the different energy density and hence different cooling rates. The fine weld microstructure led to increased microhardness values.

7.3 Recommendations for Future Work

This work is the first in the available literature to consider the hourglass weld pool shape that takes into account the surface tension developed by the laser heat source

on the top and bottom surfaces of the thin metal sheets. Based on the experience gained in this research, the following recommendations for future work are suggested.

More experimental data is needed to validate the developed model. The various power and welding speed should be investigated the effect of the surface tension to study hourglass weld pool shape behavior. Likewise, the measurements of the residual stress should be carried out to compare with the simulation results.

Different of material such as aluminum and stainless steel and dimensions such as thickness should also be studied. Here the simple butt joint was considered. More complicated geometry such as lap joint, T-joint and structure should be investigated and simulated.

In this study, the simulations used only heat transfer equations with the hourglass heat source to fit the weld pool shape. However, during the welding process, the flow of molten metal is unstable and complex. The effects of fluid flow should be studied. Details concerning fluid flow in the melt pool, the fluid equations should be incorporated.

The greatest limitation in modeling a large structure is computation time and storage requirement. In order to get more accurate results, the use of plate and shell elements might be considered, which would reduce solution times and storage requirements without a painful loss of accuracy.

Continuous cooling transformation (CCT) behavior affects the transient state of material properties employed in a numerical simulation, having a direct influence on the developing stress states. The CCT diagrams are constructed from transformation data contained in the SYSWELD database.

References

1. Tusek J, Kampus K, Suban M, (2001). "Welding of tailored blanks of different materials." *J Mater Process Technology*. 119: 180–184.
2. C.A. Huntington and T.W. Eagar, (1982). "Laser welding of Aluminum and Aluminum Alloys." *Welding Journal*. 62 (4): 105s.
3. J. Rapp, C. Glumann, F. Dausinger, H. Hugel, "Laser welding of aluminum lightweight materials: problems, solutions, readiness for application." *Optical and Quantum Electronics*. 27: 1203-1211.
4. K. H. Leong, K. R. Sabo BA, T. L. Wilkinson, C.E. Albright, (1999). "Laser Beam Welding of 5182 Aluminum Alloy Sheet." *Journal of Laser Applications*. 11 (3): 109-118.
5. H. Zhao, D.R. White, T. DebRoy, (1999). "Current issues and problems in laser welding of automotive aluminium alloys." *International Materials Reviews*. 44 (6): 238-266.
6. J. Canas, R. Picon, F. Paris, A. Blazquez and J. C. Marin, (1996). "A Simplified Numerical Analysis of Residual Stresses in Aluminum Welded Plates." *Computers & Structures.* 58 (1): 59-69.
7. K. Abdullah, P.M. Wild, J.J. Jeswiet, A. Ghasempoor, (2001). "Tensile testing for weld properties in tailor welded blanks using the rule of mixtures." *J Mater Process Technology* 112: 91–97.
8. Tsai, M. C. and Kou, S. (1989), "Marangoni convection in weld pools with a free surface. International Journal for Numerical Methods in Fluids." 9: 1503–1516
9. Zacharia, T., S. A. David, J. M. Vitek, and T. DebRoy, (1989a), Weld Pool Development during GTA and Laser Beam Welding of Type 304 Stainless Steel, Part I-II, Weld. J. Res. Suppl. 68, 499s
10. J. Goldak, A. Chakravarti, and M. Bibby, A New Finite Element Model for Welding Heat Source. Metallurgical Transactions B, 1984, 15B: p. 299-305.
11. P. Ferro, A. Zambon and F. Bonollo, Investigation of Electron-Beam Welding in Wrought Inconel 706 Materials Science Engineering A, **392** (2005), p. 94–105.
12. P. Ferro, H. Porzner, A. Tiziani and F. Bonollo, The influence of phase transformations on residual stresses induced by the welding process 3D and 2D numerical models, Modeling and Simulation in Materials Science and Engineering, 14 (2006), p. 117-136.
13. K. Masubuchi (1980) "Analysis of welded structures-Residual stressed, distortion, and their consequences" Pergamon Press
14. S.A. Tsirkas, P. Papanikos, and Th. Kermanidis (2003) Numerical simulation of the laser welding process in butt-joint specimens. Journal of Materials Processing Technology 134: 59-69
15. D. Deng, and H. Murakawa (2008) Prediction of welding distortion and residual stress in a thin plate butt-welded joint. Computational Materials Science 43: 353-365

16. G. A. Moraitis, and G. N. Labeas (2008) Residual stress and distortion calculation of laser beam welding for aluminum lap joints. Journal of Materials Technology 198: 260-269
17. M. Zain-ul-Abdein, D. Nelias, J. Jullien, and D. Deloison (2009) Prediction of laser beam welding-induced distortions and residual stresses by numerical simulation for aeronautic application. Journal of Materials Processing Technology 209: 2907-2917
18. ESI-Group. SYSWELD reference manual, 2010
19. SCHUÖCKER, D. (Ed.): Handbook of the EuroLaser Academy Vol.2. London: Chapman&Hall, 1998.
20. Kou, S., 1987, Welding Metallurgy (John Wiley and Sons, New York)
21. L. Juffus, Welding Principles and Applications, (fourth ed.), Delmar Publishers, New York (1999).
22. Pitscheneder. W., DebRoy, T., Mundra, K., and Ebner. R., (1996) Welding Journal 75: 71s-80s.
23. R. Rai, S.M. Kelly, R.P. Martukanitz, and T. DebRoy., (2008) "A Convective Heat-Transfer Model for Partial and Full penetration Keyhole Mode Laser Welding of a Structural Steel." 39(A); 98-112
24. Aalderink B J, de Lange D F, Arts R and Meijer J 2007 Keyhole shapes during laser welding of thin metal sheets J. Phys. D: Appl. Phys. 40 5388–93
25. G. A. Moraitis, and G. N. Labeas (2008) Residual stress and distortion calculation of laser beam welding for aluminum lap joints. Journal of Materials Technology 198: 260-269
26. A. Lunback, (2003). "Finite Element Modelling and Simulation of Welding of Aerospace Components.", Department of Applied Physics and Mechanical Engineering, Lulea University of Technology.
27. D. Rosenthal, The Theory of Moving Sources of Heat and its Application to Metal Treatments. Transactions of ASME, 1946. 68: p.849-865.
28. J. Goldak, A. Chakravarti, and M. Bibby, A New Finite Element Model for Welding Heat Source. Metallurgical Transactions B, 1984, 15B: p. 299-305.
29. Mazumder J., Steen W.M. “Heat Transfer Model for CW Laser Material Processing,” Journal of Applied Physics, 1980, 51(2): p. 941-947
30. J. A. Goldak, M. Akhlaghi, “Computational Welding Mechanics,” Springer, pp. 30-35, 2005.
31. S.A. Tsirkas, P. Papanikos, Th. Kermanidis, "Numerical simulation of the laser welding process in butt-joint specimens", J. Mater. Process. Technol., 134:1, pp. 59–69, 2003
32. SYSWELD 2009, “How to Model Restrains,” SYSWELD 2009 Engineering Guide, ESI Group, 2009.
33. R. W. Messler, “Principles of Welding,” John Wiley & Sons, pp. 23-25, 1999.
34. Y.C. Kim, K.H. Chang and K. Horikawa, "Characteristics of Out-of-Plane Deformation and Residual Stress Generated by Fillet Welding," Trans. JWRI, Vol.27, No.1, 1998

35. H. Du, L. Hu, J. Liu, and X. Hu, 2004, "A study on the metal flow in full penetration laser beam welding for titanium alloy," Computational Materials Science, 29: p. 419-427

36. K.B. Min, K.S. Kim, and S.S. Kang, 2000, "A study on resistance welding in steel sheets using a tailor-welded blank (1st report) evaluation of upset weldability and formability," J. Mater. Process. Technol., 101: pp. 186–192

37. Standard Methods for Mechanical Testing of Welds (7th Edition): (AWS B4.0:2007)

38. Maple 14 reference manual 2010.

39. Wu C.S., Wang H.G., and Zhang Y.M., "A New Heat Source Model for Keyhole Plasma Arc Welding in FEM Analysis of the Temperature Profile," Weld Journal 200:85(12), p. 284s-291s

APPENDIX A

Heat Intensity Equation

Derivation for Heat Intensity Distribution Equations

The heat intensity distribution is

$$Q_V(r,z) = Q_0 \exp\left(-\frac{r^2}{r_0^2}\right) \tag{1}$$

The thermal energy conservation is

$$\eta P = \int_0^H \int_0^{2\pi} \int_0^{r_0} Q_V r dr d\theta dh$$

$$= \int_0^H \int_0^{2\pi} \int_0^{r_0} Q_0 \exp\left(-\frac{r^2}{r_0^2}\right) r dr d\theta dh$$

$$= 2\pi \int_0^H \int_0^{2\pi} Q_0 \exp\left(-\frac{r^2}{r_0^2}\right) r dr dh \tag{2}$$

rearranging

$$\eta P = -\pi Q_0 \int_0^H r_0^2 \int_0^{r_0} \exp\left(-\frac{r^2}{r_0^2}\right) d\left(-\frac{r^2}{r_0^2}\right) dh$$

$$\eta P = -\pi Q_0 (e^{-1} - 1) \int_0^H r_0^2 \, dh \tag{3}$$

Three-Dimensional Conical Heat Source (TDC)

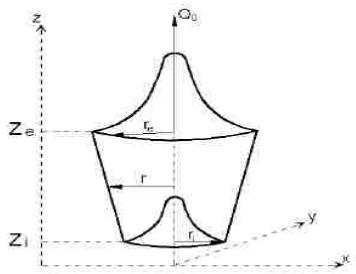

The distribution parameter can be expressed as

$$r_0(z) = r_e - (r_e - r_i)\frac{z_e - z}{z_e - z_i} \tag{4}$$

or

$$r_0^2 = \left\{r_i + (r_e - r_i)\frac{h}{H}\right\}^2 \quad , \; h = z - z_i$$

Since

$$\int_0^H r_0^2\, dh = \int_0^H \left\{r_i + (r_e - r_i)\frac{h}{H}\right\}^2 dh$$

$$= \tfrac{H}{3}(r_e^2 + r_e r_i + r_i^2) \tag{5}$$

Substituting (5) into (3)

$$\eta P = -\pi Q_0 (e^{-1} - 1)\tfrac{H}{3}(r_e^2 + r_e r_i + r_i^2)$$

Rearrange

$$Q_0 = \frac{3\eta P}{\pi(e^1 - 1)} \frac{1}{H(r_e^2 + r_e r_i + r_i^2)} \tag{6}$$

where $H = z_e - z_i$

Finally, substituting (6) into (1)

$$Q_V(r, z) = \frac{3\eta P}{\pi(e^1 - 1)(z_e - z_i)(r_e^2 + r_e r_i + r_i^2)} . \exp\left(-\frac{r^2}{r_0^2}\right)$$

APPENDIX B

Laser Welding Butt Joint Source Code

Listed here is the main input file with hour glass model for butt weld joint using laser welding process.

1. HT.DAT

```
NAME LASERWELDING_MESH_

SEARCH DATA 1000 ASCII

DEFINITION

 3D Metal Sheet Laser Welding Butt Joint with Velocity 8 m/min

OPTION THERMAL METALLURGY SPATIAL

RESTART GEOMETRY

MATERIAL PROPERTIES

  ELEMENTS GROUPS $PART$ / MATE 1

MEDIUM

  WELDLINE / GROUPS $L244$ REFERENCE $L245$ ELEMENTS $FE$ START $FN$ ARRIVAL--

 $LN$ VELOCITY 133 TINF 0 MODEL 1

$GROUP CREATE NAME GROUPNODEONLYTRAJ$ RETURN

CONSTRAINTS

  ELEMENTS GROUPS $CONV&RAD$ / KT 1 VARIABLE 1

  ELEMENTS GROUPS $COND$ / KT 1 VARIABLE 2

LOAD 1

 ELEMENTS GROUPS $CONV&RAD$ / TT 20.

 ELEMENTS GROUPS $COND$ / TT 20.

 ELEMENTS GROUPS $PART$ / QR 1 VARIABLE -10000 TRAJECTORY 1
```

TABLE

1 / FORTRAN

```
      function f(t)
C  radiative losses : f = sig * e * (t + to)(t**2 + to**2)
      e = 0.8
      sig = 5.67*-8
      to = 20.
      to = 20. + 273.15
      t1  = t + 273.15
      a = t1 * t1
      b = to * to
      c = a + b
      d = t1 + to
      d = d * c
      d = d * e
      d = d * sig
C  convective losses = 25 W/m2
      f = d + 25.
C  change to W/mm2
      d = 1*-6
      f = f * d
C
      return
      END
```

2 / FORTRAN

```
      function f(t)
```

```
C  conduction losses : f = k * (t - to) / L
      k = 58
      L = 0.1
      to = 20. + 273.15
      t1  = t + 273.15
      a = t1 - to
      a = a * k
      a = d / L
C  change to W/mm2
      d = 1*-6
      f = a * d
C
      return
      END
 10000 /  FORTRAN
      FUNCTION F(X)
C   F   = Q0 * exp( - R^2 / R0^2 ) with
C   R^2 = ( XX-X0 )^2 + ( YY-Y0-VY*T )^2
C   R0  = RE - ( RE-RI )*( ZE-ZZ+Z0 )/( ZE-ZI )
C   IF R0 < RI , R0 = 0. and return
C   IF R0 > RE , R0 = 0. and return
C
      DIMENSION X(4)
C Input
      XX = X(1)   ; X Coordinate
      YY = X(2)   ; Y Coordinate
```

```
      ZZ = X(3)   ; Z Coordinate
      TT = X(4)   ; Time
C Variables
      Q0 = 10230   ; Maximal source intensity 40%
      RE = 0.4    ; Gaussian parameter
      RI = 0.1    ; Gaussian parameter
      ZE = 0.0    ; Upper plan
      ZI = -0.5   ; Lower plan
      M1 = -1
C R^2 computation
      DE    = ZZ - ZE
      DI    = ZZ - ZI
      A1    = XX * XX
      A2    = YY * YY
      R2    = A1 + A2
      A3 = DI * DI
      IF( ZZ .LT. ZI ) R2 = R2
C R0^2 computation
      A1    = RE - RI
      A2    = ZE - ZI
      A3    = ZE - ZZ
      R0    = A3 / A2
      R0    = R0 * A1
      R0    = RE - R0
      RII   = RI + RI
      IF( ZZ .LT. ZI ) R0 = RII - R0
```

```
      R02   = R0 * R0
C F computation
      IF( R2 .GT. R02 ) RETURN
      A1    = R2 / R02
      A2    = M1 * A1
      A2    = EXP( A2 )
      F     = Q0 * A2
C
       RETURN
       END
RETURN
NAME V8_
SAVE DATA 1000
MEDIUM
EXTRACT MEDIUM
```

2. MECH.DAT

NAME LASERWELDING_MESH_

SEARCH DATA 1000 ASCII

DEFINITION

3D Metal Sheet Laser Welding Butt Joint with Velocity 8 m/min

OPTION THREEDIMENSIONAL THERMOELASTICITY

RESTART GEOMETRY

MATERIAL PROPERTIES

ELEMENTS GROUPS $PART$ / E -10000 NU -10001 YIELD -10002 LX -10003 LY -10003 -

LZ -10003 SLOPE -10004 MODEL 3 PHAS 6 AUST 6 TF 1300 KY 0

MEDIUM

WELDLINE / GROUPS $L244$ REFERENCE $L245$ ELEMENTS FE START FN ARRIVAL--

LN VELOCITY 133 TINF 0 MODEL 1

$GROUP CREATE NAME GROUPNODEONLYTRAJ$ RETURN

CONSTRAINTS

NODES GROUPS FIX / UX UY UZ

LOAD

1 NOTHING

TABLE

10000 / -10005 -10006 -10005 -10005 -10005 -10005

10001 / 1 20 0.33 1500 0.33

10002 / -10007 -10008 -10009 -10010 -10011 -10012

10003 / -10013 -10014 -10013 -10013 -10013 -10015

10004 / -10016 -10017

10005 / 1 20 210000 200 200000 400 175000 600 135000 800 78000 1000 15000 1100 7000 1200 3000 1300 1000 1500 1000

10006 / 1 20 1000 1505 1000

10007 / 1 20 234 100 180 200 139 300 110 400 89 500 70 600 57 700 40 800 25 900 14 1000 10 1100 5 1200 5 1300 5 1450 5

10008 / 1 20 141 100 108 200 83 300 66 400 53 500 42 600 34 700 24 800 16 900 14 1000 10 1100 5 1200 5 1300 5 1450 5

10009 / 1 20 600 100 575 200 544 300 505 400 466 500 402 600 305 700 188 800 100 900 14 1000 10 1100 5 1200 5 1300 5 1450 5

10010 / 1 20 380 100 339 200 297 300 256 400 214 500 173 600 132 700 90 800 63 900 14 1000 10 1100 5 1200 5 1300 5 1450 5

10011 / 1 20 380 100 339 200 297 300 256 400 214 500 173 600 132 700 90 800 63 900 14 1000 10 1100 5 1200 5 1300 5 1450 5

10012 / 1 20 141 100 108 200 83 300 66 400 53 500 42 600 34 700 24 800 16 900 14 1000 10 1100 5 1200 5 1300 5 1450 5

10013 / 1 25 0 200 0.002363 400 0.005329 600 0.008573 1000 0.0152 1200 0.0188

10014 / 1 25 0 1200 0

10015 / 1 25 -0.00937 1200 0.0180

10016 / -10018 -10018 -10019 -10020 -10018

10017 / 7 20 10021 100 10022 200 10023 300 10024 400 10025 500 10026 600 10027 700 10028 800 10029 1000 10030 1200 10031

10018 / 7 20 10032 100 10033 200 10034 300 10035 400 10036 500 10037 600 10038 700 10039 800 10040 1000 10041 1300 10042

10019 / 7 20 10043 100 10044 200 10045 300 10046 400 10047 500 10048 600 10049 700 10050 800 10051 900 10052 1000 10053 1100 10054 1200 10055 1300 10056

RETURN

NAME V8_

SAVE DATA 2000

MEDIUM

EXTRACT MEDIUM

3. METALURGICAL.DAT

MATERIAL 1 PHASE 6

KX(1) = KX(2) = KX(3) = KX(4) = KX(5) = TABLE 103

KX(6) = TABLE 104

C(1) = C(2) = C(3) = C(4) = C(5) = TABLE 105

C(6) = TABLE 106

RHO(1) = RHO(2) = RHO(3) = RHO(4) = RHO(5) = TABLE 107

RHO(6) = TABLE 108

REACTION

1 6 HEATING PEQ table 10 TAU table 11 F table 12

2 6 HEATING PEQ table 13 TAU table 14 F TABLE 15

6 1 COOLING PEQ table 20 TAU table 21 F table 22

6 4 COOLING PEQ table 30 TAU table 31 F table 32

6 3 COOLING MS 475 KM 0.01428

TABLES

10 / 1 730 0 870 1

11 / 1 700 1*6 710 1*3 730 5 870 1 1200 1 1250 5 1300 10 1400 1 1500 0.01 1550 0.001

12 / 1 1 1 100 5 1000 30 2400 60 5000 100 10000 150 20000 250 50000 550 100000 1000

13 / 1 995 0 1000 1

14 / 1 950 1*6 980 1*3 1000 1 1100 0.1 1300 0.05 1400 0.01 1500 0.01 1600 0.001

15 / 1 1 1 100 5 1000 30 2400 60 5000 100 10000 150 20000 250 50000 550 100000 1000

20 / 1 589 0 590 1 620 1 860 0

21 / 1 589 1*6 590 1 620 1 700 1 780 10 860 100

22 / 1 -200 0.01 -100 0.14 -80 0.19 -40 0.26 -20 0.24 -12.5 0.21 -7 0.3 -5 0.7 -3.2 1 -0.1 1

30 / 1 479 0   480 1 595 0

31 / 1 479 1*6 480 1 625 1

32 / 1 -280 0.01 -250 0.2 -200 0.5 -100 2 -80 3 -40 5 -20 2.5 -12.5 2 -7 3 -5 10

103 / 1 20 0.068 200 0.059 400 0.047 600 0.036 800 0.029 900 0.027 1450 0.033

104 / 1 20 0.018 800 0.025 900 0.027 1450 0.033 1475 0.033 1500 0.033 1550 0.033 1650 0.033 2500 0.033

105 / 1 0 430 100 500 200 550 300 580 400 610 500 650 600 710 700 790 800 865 900 565 1440 630 2500 707

106 / 1 0 450 100 473 200 495 300 512 400 523 500 533 600 541 700 548 800 556 900 565 1440 630 2500 707

107 / 1 0 7850*-9 200 7800*-9 400 7730*-9 600 7653*-9 700 7613*-9 1600 7190*-9

108 / 1 0 8104*-9 800 7656*-9 900 7600*-9 1000 7548*-9 1200 7443*-9 1400 7320*-9 1600 7190*-9 2500 6940*-9

END

Vita

Pornsak Thasanaraphan was born in Surin province, Northeast Thailand, on March 31st, 1972. He is a first son of Somsak and Vanussanan Thasanaraphan. He studied Mechanical Engineering and received a Bachelor degree from King Mongkut's Institute of Technology North Bangkok, KMITNB and Master degree from King Mongkut's University of Technology Thonburi, KMUTT.

After graduation at KMUTT, he worked for The Thailand Institute of Scientific and Technological Research as a research officer. In 2006, he was granted and received an honored scholarship from the Thai Royal Government to pursue his PhD at Lehigh University, USA.